

SELECTED EXAMPLES OF NMR SPECTROSCOPY TOWARDS THE  
CHARACTERIZATION OF NEXT GENERATION LITHIUM ION BATTERY  
MATERIALS

Ph.D. Thesis – A.D. Pauric; McMaster University - Chemistry

SELECTED EXAMPLES OF NMR SPECTROSCOPY TOWARDS THE  
CHARACTERIZATION OF NEXT GENERATION LITHIUM ION BATTERY  
MATERIALS

BY

ALLEN D. PAURIC, B.SC., B.ED., M.SC.

A Thesis Submitted to the School of Graduate Studies in Partial Fulfillment of the  
Requirements for the Degree Doctor of Philosophy

McMaster University

© Copyright by Allen D. Pauric, October, 2016

McMaster University DOCTOR OF PHILOSOPHY (2016) Hamilton, Ontario  
(Chemistry)

TITLE: Selected Examples of NMR Spectroscopy towards the Characterization of Next  
Generation Lithium Ion Battery Materials

AUTHOR: Allen D. Pauric,

B.Sc. (University of Ontario Institute of Technology), B.Ed. (University of Ontario  
Institute of Technology), M.Sc. (McMaster University)

SUPERVISOR: Professor Gillian R. Goward

NUMBER OF PAGES: xvii, 193

## Abstract

The research described here encompasses several different aspects of lithium ion battery operation including deep eutectic electrolytes, manganese trapping evaluation, silicon monoxide anodes, and in-situ NMR development under both static and spinning conditions. Individually, the results of these investigations as contained within the corresponding chapters contribute valuable insight. Collectively, they represent a snapshot into the numerous different ways in which nuclear magnetic resonance spectroscopy is applicable to lithium ion battery characterization.

For instance, the deep eutectic electrolytes thus studied were amenable to diffusion coefficient characterization via the  $^1\text{H}$ ,  $^7\text{Li}$  and  $^{19}\text{F}$  nuclei. This provided dynamical information on the anion, cation and neutral component and lent itself well towards parameterization of molecular dynamics simulations. The results thus obtained were useful in describing this relatively understudied class of electrolytes.

Another example is that of the evaluation of manganese trapping. In this context  $^7\text{Li}$  NMR measurements were used to investigate the competitive inhibition of manganese trapping in crown ethers by lithium. Candidate crown ethers were thus evaluated for their ability to trap  $\text{Mn}^{2+}$  and  $\text{Mn}^{3+}$  in a lithium rich environment. Given the detrimental effects that manganese dissolution from cathode materials has on cycle life performance, the NMR enabled assessment of the appropriate chelating agents had identifiable importance.

Additionally described was the progress made with silicon monoxide anodes supported on cellulosic substrates. The high active material loadings achieved, while also intriguing from a performance perspective, enabled  $^{29}\text{Si}$  MAS-NMR and  $^7\text{Li}$  static in-situ NMR measurements. For the in-situ measurements in particular, a novel cell design was constructed to utilize the advantages of a cellulosic substrate in this context. This has also enabled preliminary work on a spinning in-situ design.

## Acknowledgements

The expectation for this portion of a doctoral thesis is to acknowledge the contributions of the great many people who went into making this document possible. And indeed I do not wish to break from tradition on this point. These include people such as my supervisor, Dr. Gillian Goward, who supported my pursuit of some of the crazier projects, yet tempered them with thoughtful mentorship, useful ideas, and realistic expectations. I also include my wife, Dr. Nicole De Almeida, as her love, support, and companionship has been instrumental in maintaining the motivation to complete this degree. Besides these two main characters there is a wide supporting cast such as industrial collaborators (e.g. Dr. Ion Halalay), lab group members (you know who you are) and committee members (Dr. Adam Hitchcock and Dr. Darren Brouwer). I could go on, friends, family and all manner of other people, but I feel that might take a bit too much time. So, as outgoing lunch captain I think it would be prudent if I left off with quotes of some kind. The late author Douglas Adams gives me some inspiration in this regard as he has a knack for pointing out the absurdity and the beauty of life.

“I may not have gone where I intended to go, but I think I have ended up where I intended to be.”

“He was a dreamer, a thinker, a speculative philosopher... or as his wife would have it, and idiot.”

“I’m spending a year dead for tax reasons.”

## Table of Contents

Abstract .....	iii
Table of Contents .....	v
List of Tables .....	viii
List of Figures .....	ix
List of Abbreviations and Symbols.....	xv
Chapter 1: Introduction to Lithium Ion Batteries.....	1
1.1 - Motivation.....	1
1.2 - General Operation of Lithium Ion Batteries .....	3
1.2.1 - Cathodes .....	6
1.2.2 - Anodes.....	10
1.2.3 - Electrolytes.....	14
1.2.4 - Separators .....	17
1.2.5 - Current Collectors .....	18
1.3 - Thesis Overview .....	19
1.4 - References.....	20
Chapter 2: Introduction to Nuclear Magnetic Resonance.....	30
2.1 – Fundamentals of Nuclear Magnetic Resonance Spectroscopy.....	30
2.1.1 - Solution State NMR .....	36
2.1.2 - Diffusion NMR.....	37
2.1.3 - Molecular Dynamics .....	40
2.1.4 - MAS-NMR.....	44
2.1.5 - In-Situ NMR of Lithium Ion Battery Electrodes.....	50
2.2 - References.....	54
Chapter 3 - Combined NMR and Molecular Dynamics Modeling Study of Transport Properties in Sulfonamide Based Deep Eutectic Lithium Electrolytes in LiTFSI Based Binary Systems .....	62
3.1 - Introduction.....	62

3.2 - Experimental .....	67
3.3 - Molecular Dynamics Simulations .....	70
3.4 - Results and Discussion.....	71
3.4.1 - PFG-NMR Results .....	71
3.4.2 - Molecular Dynamics Simulation Results.....	79
3.5 - Conclusions.....	87
3.6 - References.....	88
Chapter 4: NMR Determination of the Relative Binding Affinity of Crown Ethers for Manganese Cations in Aprotic Non-Aqueous Lithium Electrolyte Solutions .....	94
4.1 - Introduction.....	95
4.2 - Experimental .....	99
4.3 - Modeling of Cation Binding .....	101
4.4 - Results and Discussion.....	105
4.5 - Conclusions and Outlook .....	113
4.6 - References.....	115
Chapter 5 - Cellulose Substrates and their Application to Solid State NMR of Lithium Ion Batteries: A Case Study in Silicon Monoxide Anodes .....	123
5.1 - Introduction.....	124
5.2 - Experimental .....	128
5.3 - Results and Discussion.....	131
5.4 - Conclusion .....	145
5.5 - References.....	146
Chapter 6: Rotobattery .....	153
6.1 - Introduction.....	153
6.2 - Objectives.....	156
6.3 - Structural Considerations .....	157
6.4 - Cell Assembly .....	160
6.4.1 - Initial Electrochemical Performance .....	163
6.4.2 - Initial NMR Performance .....	164
6.5 - Future Considerations .....	170

6.6 – Summary.....	173
Chapter 7 – Summary, Conclusion, and Appendices.....	177
7.1 - Summary .....	177
7.2 - Conclusion .....	182
7.3 - Appendices.....	183
7.3.1 - Chapter 3 .....	183
7.3.2 - Chapter 4 .....	187
7.3.3 - Chapter 5 .....	191
7.3.4 - Chapter 6 .....	193

## List of Tables

Table 2.1. Relative magnitudes of different interactions that influence the NMR spectra of solids .....	47
Table 2.2. Nuclear properties for relevant nuclei investigated in this thesis .....	50

## List of Figures

<b>Figure 1.1.</b> Lithium Ion Battery Schematic (Osiak, M.; Geaney, H.; Armstrong, E.; O’Dwyer, C. Structuring Materials for Lithium-Ion Batteries: Advancements in Nanomaterial Structure, Composition, and Defined Assembly on Cell Performance. <i>J. Mater. Chem. A</i> 2014, 2 (25), 9433–9460.) (Reproduced with permission from the Royal Society of Chemistry) .....	4
<b>Figure 1.2.</b> Representative crystal structures of cathode materials for lithium-ion batteries: (a) layered $\alpha$ -LiCoO <sub>2</sub> ; (b) cubic LiMn <sub>2</sub> O <sub>4</sub> spinel; (c) olivine-structured LiFePO <sub>4</sub> ; (d) $\beta_{II}$ -Li <sub>2</sub> FeSiO <sub>4</sub> ; and (e) tavorite-type LiFeSO <sub>4</sub> F. Li ions are shown as light green spheres, CoO <sub>6</sub> octahedra in blue; MnO <sub>6</sub> octahedra in mauve, Fe–O polyhedra in brown, PO <sub>4</sub> tetrahedra in purple, SiO <sub>4</sub> tetrahedra in yellow, SO <sub>4</sub> tetrahedra in grey, and in (e) fluoride ions in dark blue. Black lines demarcate one unit cell in each structure. (Islam, M. S.; Fisher, C. A. J. Lithium and Sodium Battery Cathode Materials: Computational Insights into Voltage, Diffusion and Nanostructural Properties. <i>Chem. Soc. Rev.</i> 2013, 43 (1), 185–204.) (Reproduced with permission from the Royal Society of Chemistry under Creative Commons Attribution 3.0 License) .....	7
<b>Figure 1.3.</b> Representative lithium dendrite formation (Orsini, F.; Du Pasquier, A.; Beaudoin, B.; Tarascon, J. M.; Trentin, M.; Langenhuisen, N.; De Beer, E.; Notten, P. In Situ Scanning Electron Microscopy (SEM) Observation of Interfaces within Plastic Lithium Batteries. <i>J. Power Sources</i> 1998, 76 (1), 19–29.) (Reproduced with permission from The Journal of Power Sources) .....	11
<b>Figure 2.1.</b> The Morse potential (blue) and harmonic oscillator potential (green). The potential at infinite internuclear distance is the dissociation energy for pure vibrational spectra. For vibronic spectra there are two potential curves and the dissociation limit is the <i>upper</i> state energy at infinite distance. (Used with permission from Mark Somoza via Wikipedia under the CC BY-SA 3.0 License) .....	31
<b>Figure 2.2.</b> Zeeman splitting diagram for a spin ½ nucleus placed in a magnetic field. Used with permission from UC-Davis University of California under the CC NC-SA 3.0 License. Contributors include Derrick Kaseman and Revathi Srinivasan Ganesh Lyer. Figure is available through the following URL: <a href="http://chem.libretexts.org/Core/Physical_Chemistry/Spectroscopy/Magnetic_Resonance_Spectroscopies/Nuclear_Magnetic_Resonance/Nuclear_Magnetic_Resonance_II">http://chem.libretexts.org/Core/Physical_Chemistry/Spectroscopy/Magnetic_Resonance_Spectroscopies/Nuclear_Magnetic_Resonance/Nuclear_Magnetic_Resonance_II</a> .....	33
<b>Figure 2.3.</b> Longitudinal eddy current delay gradient pulse (LEDGP2S), pulse sequence .....	38

<b>Figure 2.4.</b> Example of curve fitting for the diffusion coefficient using data for $^7\text{Li}$ in a 50/50 wt% ethylene carbonate/dimethyl carbonate solution of 1M $\text{LiPF}_6$ .....	40
<b>Figure 2.5.</b> Schematic of a HR-MAS stator depicted with the additional inclusion of gradient coils orientated along the magic angle. (Todd M. Alam and Janelle E. Jenkins (2012). HR-MAS NMR Spectroscopy in Material Science, Advanced Aspects of Spectroscopy, Dr. Muhammad Akhyar Farrukh (Ed.), InTech, DOI: 10.5772/48340. Available from: <a href="http://www.intechopen.com/books/advanced-aspects-of-spectroscopy/hr-mas-nmr-spectroscopy-in-material-science">http://www.intechopen.com/books/advanced-aspects-of-spectroscopy/hr-mas-nmr-spectroscopy-in-material-science</a> ).....	45
<b>Figure 2.6.</b> Example of resolution enhancement as demonstrated by using high resolution magic angle spinning (HR–MAS) NMR for A) methanol swollen anion exchange membrane, and B) $\text{CDCl}_3$ swollen pBAN (polyButadiene-AcryloNitrile) polymer. (Todd M. Alam and Janelle E. Jenkins (2012). HR-MAS NMR Spectroscopy in Material Science, Advanced Aspects of Spectroscopy, Dr. Muhammad Akhyar Farrukh (Ed.), InTech, DOI: 10.5772/48340. Available from: <a href="http://www.intechopen.com/books/advanced-aspects-of-spectroscopy/hr-mas-nmr-spectroscopy-in-material-science">http://www.intechopen.com/books/advanced-aspects-of-spectroscopy/hr-mas-nmr-spectroscopy-in-material-science</a> ) .....	48
<b>Figure 3.1.</b> Structural formulae of the organic components considered in this work, methanesulfonamide (MSA) and dimethylmethanesulfonamide (DMMSA).....	68
<b>Figure 3.2.</b> Temperature dependence of the $^1\text{H}$ , $^7\text{Li}$ , and $^{19}\text{F}$ diffusion coefficients in DMMSA:LiTFSI mixtures at (a) 1:1, (b) 3:1, and (c) 6:1 molar ratios, determined by PFG-NMR.....	72
<b>Figure 3.3.</b> Temperature dependence of the $^1\text{H}$ , $^7\text{Li}$ , and $^{19}\text{F}$ diffusion coefficients at 1:1 (a), 3:1 (b) and 6:1 (c) MSA:LiTFSI molar ratios, determined through PFG-NMR. ....	72
<b>Figure 3.4.</b> Variation of the lithium transport numbers with temperature derived from $^1\text{H}$ , $^7\text{Li}$ , and $^{19}\text{F}$ diffusion coefficient measurements for 1:1, 3:1 and 6:1 mole ratios of MSA:LiTFSI (a) and DMMSA:LiTFSI (b).....	77
<b>Figure 3.5.</b> Lithium-nitrogen radial distribution functions for $\text{Li}^+$ contact with TFSI (a) and MSA (b) at 298K in MSA:LiTFSI mixtures.....	80
<b>Figure 3.6.</b> Lithium-nitrogen radial distribution functions for intermolecular between contact between $\text{Li}^+$ and TFSI (a) or DMMSA (b) at 298 K in DMMSA:LiTFSI mixtures.....	81
<b>Figure 3.7.</b> Lithium – oxygen radial distribution functions for intermolecular contact between $\text{Li}^+$ and TFSI (a) or MSA (b) at 298 K for MSA:LiTFSI mixtures. ....	82
<b>Figure 3.8.</b> Lithium – oxygen radial distribution functions for intermolecular contact between $\text{Li}^+$ cations and TFSI (a) or DMMSA (b) in DMMSA:LiTFSI at 298 K.....	83

<b>Figure 3.9:</b> Oxygen – hydrogen radial distribution functions for intermolecular contact between MSA and TFSI (a) or MSA (b) in MSA:LiTFSI mixtures at 298 K. ....	85
<b>Figure 3.10.</b> Oxygen – hydrogen radial distribution functions for intermolecular contact between MSA and TFSI (a) or MSA (b) in MSA:LiTFSI mixtures at 358 K. ....	85
<b>Figure 3.11.</b> Oxygen – hydrogen radial distribution functions for intermolecular contact between DMMSA and TFSI (a) or DMMSA (b) in DMMSA:LiTFSI mixtures at 298 K. ....	86
<b>Figure 3.12.</b> Oxygen – hydrogen radial distribution functions for intermolecular contacts between DMMSA and TFSI (a) or DMMSA (b) in DMMSA:LiTFSI mixtures at 358 K. ....	86
<b>Figure 4.1.</b> Chemical structures of the ion trapping agents investigated in the present work, (a) 15-crown-5 and (b) 1-aza-15-crown-5. ....	100
<b>Figure 4.2.</b> Theoretical binding curves for $\text{Li}^+$ binding to crown ether with a total $[\text{Li}^+]$ of 0.005 mol/L for $K_{\text{Li}^+}$ values ranging from 1 to 10,000 L/mol. ....	103
<b>Figure 4.3.</b> Theoretical binding curves for $\text{Li}^+$ binding to crown ether in the presence of manganese cations. Total metal concentration is at $5 \times 10^{-3}$ mol/L consisting of $2.5 \times 10^{-3}$ mol/L of lithium and $2.5 \times 10^{-3}$ mol/L of manganese over a range of equilibrium constant ratios. The equilibrium constant for lithium was kept constant at 1000 L/mol. ....	104
<b>Figure 4.4</b> Experimental binding curves for $\text{Li}^+$ binding to 1-aza-15-crown-5 (A15C5) and 15-crown-5 (15C5) in propylene carbonate solvent at a constant $\text{Li}^+$ concentration of ~3 mM. ....	106
<b>Figure 4.5.</b> Experimental $^7\text{Li}$ chemical shifts for $\text{Li}^+$ binding with increasing amounts of 15-crown-5 (15C5) from the bottom (0 mM) to the top (~3 mM) of the figure. Each spectrum represents an approximate increase in 15-crown-5 molarity of 0.2 mM. These were all collected in the presence of a constant amount of both $\text{MnCl}_2$ and LiTFSI in the in the propylene carbonate solvent, each at ~1 mM concentration. ....	108
<b>Figure 4.6.</b> Experimental $^7\text{Li}$ chemical shifts for $\text{Li}^+$ binding to increasing amounts of 1-aza-15-crown-5 (A15C5) and 15-crown-5 (15C5) in the presence approximately equimolar amounts of $\text{MnCl}_2$ and propylene carbonate solvent. ....	110
<b>Figure 4.7.</b> Experimental $^7\text{Li}$ chemical shifts for $\text{Li}^+$ binding to increasing amounts of 1-aza-15-crown-5 and 15-crown-5 in the presence approximately equimolar amounts of $\text{Mn}(\text{OAc})_3$ in propylene carbonate solvent. ....	111
<b>Figure 4.8.</b> Experimental $^7\text{Li}$ chemical shifts with $\text{Li}^+$ binding to increasing amounts of 10 wt% divinylbenzene – 90 wt% vinylbenzyl-aza-15-crown-5 in both a manganese free environment and one containing $\text{Mn}(\text{CH}_3\text{COO})_3$ and propylene carbonate solvent. ....	112

- Figure 4.9.** SEM micrograph of the 10 wt% divinylbenzene – 90 wt% vinylbenzyl-aza-15-crown-5 polymer from the present study. The polymeric particles have a spherical morphology with diameters ranging from 20 to 50 nm. .... 113
- Figure 5.1.** Silicon monoxide capacity (a) and coulombic efficiency (b) data over multiple cycles showing an associated variation in performance. An additional replicate was included to further verify the observed trend..... 132
- Figure 5.2.**  $^{29}\text{Si}$  MAS-NMR spectra of pristine silicon monoxide (a), silicon monoxide discharged to 77 mAh/g (b), and discharged to 330 mAh/g (c)..... 134
- Figure 5.3.**  $^{29}\text{Si}$  MAS-NMR spectra of further discharged silicon monoxide electrodes including 781 mAh/g (red), 1239 mAh/g (blue), 1755 mAh/g (green), and 2059 mAh/g (purple). The sample cycling curve serves as a legend to correlate the appropriate coloured spectra with their position on the cycling curve. The dashed line is presented in reference to work by Eckert et al.<sup>32</sup> where the isotropic  $^{29}\text{Si}$  chemical shift of a pure phase of  $\text{Li}_7\text{Si}_3$  is shown for reference ..... 135
- Figure 5.4.**  $^{29}\text{Si}$  MAS-NMR spectra of charged silicon monoxide anodes from 2230 mAh/g to near the end of charge at approximately 1000 mAh/g showing the reversible capacity associated with the broad resonance and the peak at -20 ppm. .... 137
- Figure 5.5.** The central figure shows a deconvolution of  $^{29}\text{Si}$  MAS-NMR spectrum for the species lithiated to 1239 mAh/g capacity. The spectrum depicts a narrow  $\text{Li}_4\text{SiO}_4$  peak (-70 ppm) as well as lithium silicide products (narrow peak at -20 ppm, broad peak at -70 ppm) associated with the other two resonances. The left figure shows how the chemical shift of the broad lithium silicide resonance changes as a function of lithiation. On the right figure the integral area of the lithium silicide peaks is shown as a function of the lithiation capacity, normalized to the intensity of the  $\text{Li}_4\text{SiO}_4$  resonance..... 139
- Figure 5.6.** Schematic of in-situ cell configuration showing an overview (a) and a closeup (b) of the cell design. Elements include the anode and cathode wires (magenta and cyan spirals respectively), plastic core (red cylinder) and the lithium metal, separator, and cellulosic substrate anode (represented by the purple, white and gray cylinders respectively). These are all enclosed in a plastic tube with a silicon rubber septum serving to isolate the battery chemistry from the environment while allowing electrical connections..... 140
- Figure 5.7.** Comparison of  $^7\text{Li}$  in-situ spectra detailing change in lithium chemical shift across a full discharge/charge cycle for cellulose based silicon metal anodes (a) and silicon monoxide (b) ..... 142

<b>Figure 5.8.</b> Comparison of $^7\text{Li}$ in-situ snapshots detailing change in lithium chemical shift at the beginning (blue) middle (red) and end (green) of charge for cellulose based silicon metal anodes (a) and silicon monoxide (b) .....	144
<b>Figure 6.1.</b> Schematic depiction of rotobattery support structure .....	158
<b>Figure 6.2.</b> Longitudinal cross sectional schematic of rotobattery construction.....	162
<b>Figure 6.3.</b> Initial cycling data for rotobattery prototype using an LCO cathode and graphite anode on cellulosic substrates with 1M $\text{LiPF}_6$ in EC/DMC electrolyte cycled at 7.5 $\mu\text{A}$ constant current between 2 and 4.3 V.....	164
<b>Figure 6.4.</b> Single charge cycle for LCO/Graphite full cycled in 4 mm rotor with 1M $\text{LiPF}_6$ in EC/DMC. Discontinuities constitute periodic stoppages and were often associated with an increase in current rate to expedite the experiment. ....	165
<b>Figure 6.5.</b> Stacked MAS-NMR under various conditions including static (a), 4 kHz (b), 8 kHz (c), and 10 kHz (d) of the fully charged rotobattery. The # symbols correspond to resonances while the * symbols are their associated spinning sidebands.....	166
<b>Figure 6.6.</b> $^7\text{Li}$ MATPASS spectra @ 10 kHz spinning speed for a LCO/Graphite charged rotobattery soon after ending charge (a), and 24 hours later (b). ....	168
<b>Figure 6.7.</b> $^7\text{Li}$ MAS-NMR single pulse experiments collected soon after charge (a), and after a further 24 hours (b). The # symbols correspond to resonances while the * symbols are their associated spinning sidebands. ....	169
<b>Figure 6.8.</b> Schematic of rotobattery operation with left side showing support template with battery components connected to the top of the cell via a LED. The whole assembly is depicted assembled into a 4 mm rotor with the inclusion of a central hole cut in the rotor cap to allow laser light illumination. Shown right are the expected operational modes for the LED both with and without illumination. ....	172
<b>Figure 7.3.1.1.</b> Lithium-nitrogen volume integrals for $\text{Li}^+$ contact with TFSI (a) and DMMSA (b) in DMMSA:LiTFSI mixtures at 298K.....	184
<b>Figure 7.3.1.2.</b> Lithium-nitrogen volume integrals for $\text{Li}^+$ contact with TFSI (a) and MSA (b) in MSA:LiTFSI mixtures at 298K.....	185
<b>Figure 7.3.1.3.</b> Lithium-oxygen volume integrals for intermolecular contact between $\text{Li}^+$ and TFSI (a) and DMMSA (b) in DMMSA:LiTFSI mixtures at 298K.....	185
<b>Figure 7.3.1.4.</b> Lithium-oxygen volume integrals for intermolecular contact between $\text{Li}^+$ and TFSI (a) and MSA (b) in MSA:LiTFSI mixtures at 298K.....	186
<b>Figure 7.3.1.5.</b> Ionicity derived through the ratio of molar conductivities, as determined by impedance spectroscopy and NMR.....	186

**Figure 7.3.2.1.** Example theoretical lithium binding curve generated in Maple 16 from equation (8) with [crown ether] in mM being plotted as the dependent variable and normalized chemical shift as the independent variable ..... 190

**Figure 7.3.3.1.** Top view of in-situ sample mounting configuration on probe head including anode and cathode electrical connections, strain relieving metallic posts, and connections to probe base. .... 191

**Figure 7.3.3.2.** Side view of in-situ sample mounting configuration on probe head including anode and cathode electrical connections, strain relieving metallic posts, and connections to probe base. .... 192

**Figure 7.3.4.1** – OpenSCAD code used to construct rotobattery support..... 193

### List of Abbreviations and Symbols

B	External Magnetic Field
C	Charge rate
CSA	Chemical Shielding Anisotropy
D	Diffusion coefficient
DEC	Diethyl carbonate
DMC	Dimethyl Carbonate
DMMSA	Dimethylmethanesulfonamide
e	Elementary charge
EC	Ethylene Carbonate
FID	Free Induction Decay
G	Gradient strength
G.M.	General Motors
$h$	Planck's Constant
I	Spin
$I_0$	Initial signal intensity
$I_f$	Observed signal intensity
IF	Infrared
IL	Ionic liquid
$K_{Li}$	Equilibrium constant for lithium trapping in crown ether
$K_{Mn}$	Equilibrium constant for manganese trapping in crown ether
LIB	Lithium Ion Battery
LiFSI	Lithium fluorosulfonyl (Imide)
LiTFSI	Lithium bis(trifluoromethanesulfonyl)imide
LMO	$Li_xMn_2O_4$ spinel

MD	Molecular Dynamics
MSA	Methanesulfonamide
NMC	Nickel Manganese Cobalt Oxide
NMR	Nuclear Magnetic Resonance
NPT	Isobaric-Isothermal ensemble
NVT	Canonical ensemble
OPLS-AA	Optimized Potential for Liquid Simulations, All Atom variant
PFG	Pulsed Field Gradient
R&D	Research and Development
RF	Radio Frequency
SEI	Solid Electrolyte Interphase
S/N	Signal to Noise
SEM	Scanning electron microscopy
TMO	Transition Metal Oxide
$[\otimes]$	Molar concentration of free crown ether
$[\otimes_0]$	Initial molar concentration of free crown ether
$[Mn]$	Molar concentration of free manganese
$[Mn_0]$	Initial molar concentration of free manganese
$[Mn \cup \otimes]$	Molar concentration of manganese-crown complex
$[Li]$	Molar concentration of free lithium
$[Li_0]$	Initial molar concentration of free lithium
$[Li \cup \otimes]$	Molar concentration of lithium-crown complex
$\partial_{obs}$	Observed chemical shift

$\delta_{Li}$	Free lithium chemical shift
$x_{Li}$	Lithium mole fraction
$\delta_{Li\cup\otimes}$	Bound lithium chemical shift
$x_{Li\cup\otimes}$	Bound lithium mole fraction
$\delta_{obs,n}$	Normalized, observed chemical shift
$\omega$	Larmor frequency
$\gamma$	Gyromagnetic ratio
$\nu$	Frequency
$\Delta$	Diffusion delay
$\partial$	Gradient pulse length
$\varepsilon$	Potential energy well depth
$V_{LJ}$	Lennard-Jones Potential
$\sigma_{iso}$	Isotropic chemical shift
$\eta_{\sigma}$	Asymmetry parameter
$V_{zz}$	Electric field gradient tensor
$\hbar$	Reduced Planck constant
$\Theta$	Spin orientation with respect to magnetic field axis
$\Phi$	Spin orientation with respect to x-y plane

## **Chapter 1: Introduction to Lithium Ion Batteries**

### **1.1 - Motivation**

The industrial revolution has brought about an unprecedented increase in the standard of living for a significant fraction of humanity. An energy bonanza in the form of fossil fuels has enabled this transformation. But, the accompanying increase in CO<sub>2</sub> emissions is associated with some particularly worrisome consequences.<sup>1</sup> As the 21<sup>st</sup> century progresses warning signs of impending climate catastrophe have become clearly evident. These include rising global temperatures<sup>2</sup>, mass coral reef bleaching<sup>3</sup>, sea level rise<sup>4</sup>, and many others. Unfortunately these are merely a preview of the changes predicted in the coming decades where current models suggest a global temperature increase on the order of 3-6 °C over the next century. This would ultimately shift the climate into a realm not experienced for millions of years.<sup>5</sup>

Such warm temperatures have been present on Earth before. And while mass extinctions would certainly occur (as is argued to be occurring already) life would eventually adapt and recover. However, human civilization has evolved over the last 10,000 years in an era of relative climactic stability. Our population centers and agricultural heartlands have evolved in this timeframe to take advantage of the local characteristics of a given region. The predicted changes to this climate regime would alter these places, in some cases to the point of being inhospitable to human life.<sup>6</sup> Overall climate disruption coupled with the rapidity of the change would incur an astounding cost both in lives and material. Scarce resources have historically often led to conflict, and the

potential nuclear consequences of a large scale conflict could be the most disastrous of all.

The simplest way to escape this grim scenario is to drastically reduce greenhouse gas emissions. Although this will be difficult as the majority of our energy is still derived from fossil fuels.<sup>7</sup> Fortunately there exist a vast array of significantly less polluting sources including wind, solar, hydroelectric, tidal, nuclear, and others. The energy sources mentioned are however associated with their own mixture of positive and negative consequences. Of particular note is that adoption of the listed technologies for portable applications requires a ready means of electrical energy storage. While there exist several options to address this issue, lithium ion batteries (LIBs) have emerged as a popular solution.<sup>8</sup>

Lithium ion batteries have been commercially available for over 25 years and matured to take a central role in portable applications.<sup>9</sup> Long cycle life and high energy density have contributed to their ubiquity. A distinctly important application is their utilization in electric vehicles. Transportation accounts for a significant fraction of global CO<sub>2</sub> emissions. The electrification of transportation and prerequisite incorporation of energy storage technology would provide a significant boost to the CO<sub>2</sub> reduction effort. In recent years there has been substantial interest in the electrification of transportation with numerous companies investing heavily in electric vehicle offerings. This trend shows no sign of abating and continued advancement in LIB technology can only help to accelerate this progression.

It is no understatement to say that technologies which enable a low carbon future are

crucial in ensuring the continued viability of human civilization. Lithium ion batteries are a part of this future and thus serve to motivate the research presented here.

## **1.2 - General Operation of Lithium Ion Batteries**

A lithium ion battery represents a convenient and efficient method of storing electrical potential energy. It does this by facilitating the controlled and reversible redox reaction of two lithium containing electrodes. A description of this reaction can be described in stages using the initial states of the reactants as a starting point.

Key components of a LIB include the cathode, anode, separator, and electrolyte and current collectors. While there are other ancillary components these are the ones required to obtain a basic understanding of LIB operation (Figure 1.1). The cathode is usually comprised of a transition metal oxide (TMO) as the active material, with small amounts of carbon for electrical conduction and fluorinated binder for structural integrity. These materials typically have reduction potentials which range from between 3.5 to 4.5V versus lithium and are synthesized in a fully reduced state. Most anodes however start in a lithium free state, including graphite, the most commonly used anode material. As lithium is extracted from the cathode and reversibly intercalated between the graphite planes, the potential of the graphite anode rapidly drops and plateaus at its intercalation potential of 0.1V versus lithium.<sup>10</sup> This process will not occur spontaneously as it creates a larger potential energy difference between the cathode and anode. Energy is required from an outside source to facilitate the redox reaction in this direction. This can be done by connecting the anode and cathode to an external power supply and supplying a reverse

bias. However, for the reaction to proceed, lithium from the cathode must intercalate into the anode to satisfy charge balance requirements. If the electrodes are placed in direct contact with no electrically insulating barrier an electrical short circuit across the anode/cathode interface will result.

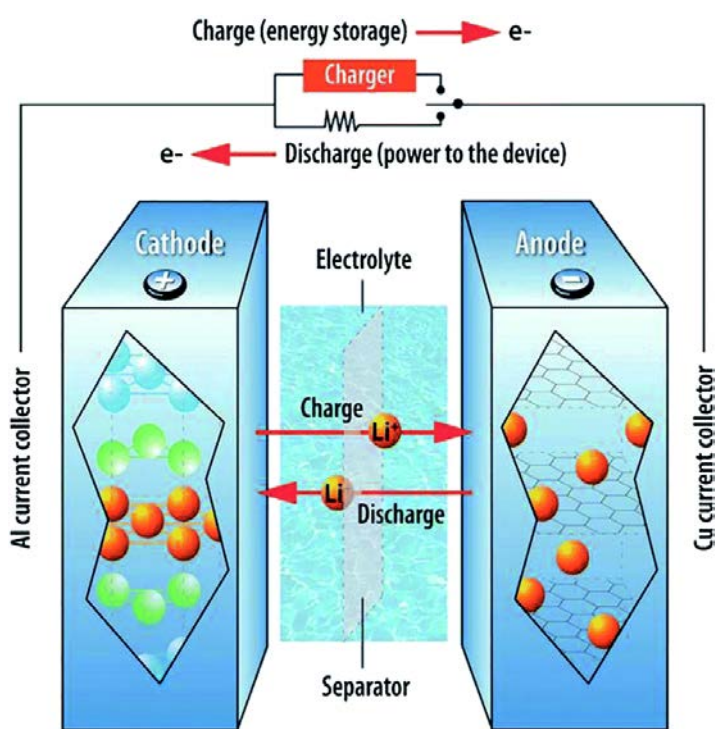


**Figure 1.1.** Lithium Ion Battery Schematic (Osiak, M.; Geaney, H.; Armstrong, E.; O'Dwyer, C. Structuring Materials for Lithium-Ion Batteries: Advancements in Nanomaterial Structure, Composition, and Defined Assembly on Cell Performance. *J. Mater. Chem. A* 2014, 2 (25), 9433–9460.) (Reproduced with permission from the Royal Society of Chemistry)

Proper use of an electrolyte/separator combination solves the problem of lithium transport and electrical insulation respectively. The electrolyte, typically a solution of 1M  $\text{LiPF}_6$  in ethylene carbonate/dimethyl carbonate (EC/DMC) and derivatives thereof, has the right combination of parameters to make it an ideal medium for lithium ion transport.<sup>11</sup> Additionally, the porous plastic separator, typically polypropylene and/or mixtures of other plastics, is permeable to lithium ions but prevents the electrical short circuit of the electrodes. An applied reverse bias under these circumstances will facilitate the cathode/anode redox reaction. Lithium cations emerging from the cathode and entering the solution are simultaneously coupled with lithium cations in the solution intercalating into the graphite. Once the cathode is delithiated to the desired state of charge, the circuit is connected to a load and controllably discharged to suit both the device and the cell chemistry.

This basic description of LIB operation glosses over a metaphorical mountain of complexity associated with lithium ion battery chemistry. From this, one of the most crucial issues which arise is that of performance degradation. LIBs are designed to endure hundreds and up to thousands of cycles with limited capacity loss.<sup>12</sup> This feat is made all the more surprising by the inherent thermodynamic instability of a lithium ion battery. Namely, the anode is operated at such a reducing potential that no known liquid electrolyte remains unreacted. For most electrolytes this represents an incompatibility as it will continually react, building up degradation products and quickly halting operation. However, specifically tailored electrolytes can decompose to produce a passivating solid electrolyte interphase (SEI) which significantly reduces the rate of electrolyte

degradation, but still allows for lithium conduction to the active material.<sup>13</sup>

Other problems in this vein abound when improving the cyclability of LIBs. Their inherent thermodynamic instability and the expectation of long cycle life means that even small problems which contribute little during the first cycle can accumulate to have a significant impact over hundreds of cycles. To understand some of the factors which underlie this behaviour, the following sections provide a generalized overview of the various LIB components. Particular emphasis is placed on features pertinent to subsequent chapters.

### **1.2.1 - Cathodes**

Transition metal oxides represent the most common type of cathode material. Their high oxidative potential coupled with excellent reversibility and minimal structural deformation has situated them as the de-facto standard for LIBs. Figure 1.2 exemplifies the solid state structure for a sampling of these materials. While  $\text{LiCoO}_2$  was the first to be successfully commercialized, better performing alternatives have superseded it. Of particular interest lately is the  $\text{LiNi}_{0.33}\text{Mn}_{0.33}\text{Co}_{0.33}\text{O}_2$  (NMC) cathode.<sup>14</sup> It has a power density comparable to  $\text{LiCoO}_2$  but significantly improves on its cyclability and safety parameters. Furthermore it retains other favourable features such as a sloped charge profile where the voltage of the material depends on its state of charge in a range from 3.7V up to 4.3V and higher. This allows for a simpler state of charge calculation which is particularly useful in automotive applications for range estimation.

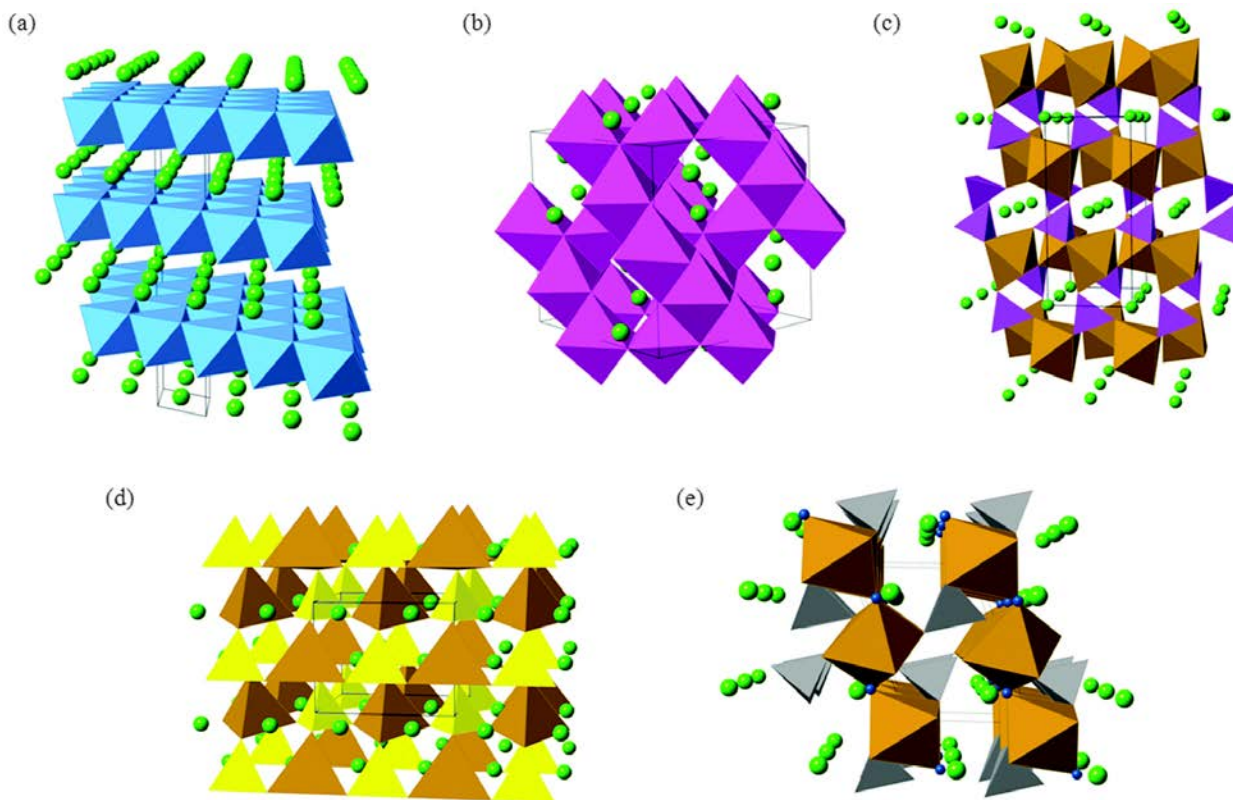


**Figure 1.2.** Representative crystal structures of cathode materials for lithium-ion batteries: (a) layered  $\alpha$ -LiCoO<sub>2</sub>; (b) cubic LiMn<sub>2</sub>O<sub>4</sub> spinel; (c) olivine-structured LiFePO<sub>4</sub>; (d)  $\beta_{II}$ -Li<sub>2</sub>FeSiO<sub>4</sub>; and (e) tavorite-type LiFeSO<sub>4</sub>F. Li ions are shown as light green spheres, CoO<sub>6</sub> octahedra in blue; MnO<sub>6</sub> octahedra in mauve, Fe–O polyhedra in brown, PO<sub>4</sub> tetrahedra in purple, SiO<sub>4</sub> tetrahedra in yellow, SO<sub>4</sub> tetrahedra in grey, and in (e) fluoride ions in dark blue. Black lines demarcate one unit cell in each structure. (Islam, M. S.; Fisher, C. A. J. Lithium and Sodium Battery Cathode Materials: Computational Insights into Voltage, Diffusion and Nanostructural Properties. *Chem. Soc. Rev.* 2013, 43 (1), 185–204.) (Reproduced with permission from the Royal Society of Chemistry under Creative Commons Attribution 3.0 License)

A common aspect of many high voltage cathodes is the use of manganese. Some, such as LiNi<sub>0.5</sub>Mn<sub>1.5</sub>O<sub>4</sub> have standard reduction potentials as high as 4.9V versus lithium.<sup>15</sup>

Others like  $\text{LiMn}_2\text{O}_4$  have a somewhat reduced power density versus NMC. However, the relative cost of manganese being an order of magnitude cheaper than either nickel or cobalt helps outweigh this disadvantage.

Unfortunately a major drawback of many manganese containing cathodes is that over the course of cycling small amounts of manganese cations leach out of the electrode structure and into the electrolyte. This is an especially prevalent issue for  $\text{LiMn}_2\text{O}_4$  where the problem has been noted for over two decades.<sup>16</sup> Dissolved manganese in the electrolyte migrates towards the anode and has been linked to detrimental side reactions.<sup>17</sup> Specifically the highly reducing environment of the anode promotes deposition of metallic manganese. Clusters of metallic manganese have been linked to the catalysis of electrolyte decomposition. The products of this deposition rapidly increase the thickness of the SEI layer, increasing cell polarization and ultimately resulting in rapid capacity fade.

There is some debate as to the details of the manganese dissolution mechanism but it is generally believed to be aided by the presence of  $\text{LiPF}_6$ .<sup>18</sup> The most widely accepted scenario is that trace amounts of water promote the formation of HF from the decomposition of  $\text{LiPF}_6$ . The HF then reacts with the manganese containing oxide, yielding decomposition products which include soluble manganese and water. Thus the reaction acts as a positive feedback loop promoting further manganese dissolution.

One of the more contentious issues surrounding the capacity fade mechanism is the oxidation state of the dissolved manganese cations. Some of the earliest reports suggested that  $\text{Mn}^{3+}$  is the initial oxidation state dissolved, which is followed by disproportionation

into  $\text{Mn}^{2+}$  and  $\text{Mn}^{4+}$ .<sup>19</sup> However, recent studies have contested this traditional view suggesting an average oxidation state closer to  $\text{Mn}^{3+}$  but with significant proportions of  $\text{Mn}^{2+}$  and  $\text{Mn}^{4+}$ .<sup>20</sup> The question of oxidation state becomes more important when considering methods of mitigating the damage caused by manganese.

Commonly employed methods include physical coatings on the cathode material to physically prevent dissolution<sup>21</sup> or electrolyte additives<sup>22</sup> which suppress dissolution and/or promote resistance of the anode to capacity fade. A more recent proposed alternative is to trap dissolved manganese in the separator through the use of chelating agents.<sup>20,23</sup> This has the advantage of being independent of the cathode or anode chemistry and readily applicable to existing battery manufacture without major modifications.

Crown ethers are extensively studied chelating agents which have properties that are well suited to the sequestration of manganese. Not least of these is the size selectivity obtained by tuning the radius of the macrocycle to the size of cation being trapped.<sup>24</sup> Complicating matters is the question of manganese oxidation state having a direct influence on cation size and thus on the appropriate choice of macrocycle. In an environment where the concentration of lithium is at least 2-3 orders of magnitude greater than the manganese concentration, it is crucial that there is preferential trapping of manganese over lithium.

A systematic method of screening trapping efficiency is useful to determine candidates most suitable for testing during battery operation. This needs to be conducted not just for the free molecule but also in the bound state as it exists in the polymer. Such a

comparison could yield both the maximum and practical trapping efficiency of the selected macrocycle. Nuclear magnetic resonance spectroscopy (NMR) is suited to this kind of characterization through the relatively simple monitoring of lithium chemical shift variation in the presence of manganese and crown ether. An example of this type of characterization is the subject of chapter 4 of this thesis.

Besides the TMOs there are next generation cathode materials which can provide significant LIB performance increases, in contrast to the incremental gains over the last 25 years. Among these are the lithium-sulfur<sup>25</sup> and lithium-air chemistries.<sup>26</sup> In the case of lithium-sulfur there is a two electron reduction of elemental sulfur from  $S^0$  to  $S^{2-}$  whereas in the lithium air cell metallic lithium is directly oxidized to yield  $Li_2O_2$ . In both cases the lack of heavy transition metals greatly increases the gravimetric capacity. Of these, lithium-sulfur is the closest to commercialization but its biggest drawback lies in capacity fade due to active material dissolution through polysulfide intermediates.

### **1.2.2 - Anodes**

Anode materials can be broadly summarized as being intercalation compounds such as graphite and lithium titanium oxide, alloys including lithium-silicon and lithium-tin, or lithium metal itself. Of these, graphite is the most commonly utilized. It has a capacity of 372 mAh/g at an intercalation voltage of 0.1V with great safety characteristics and excellent cyclability.<sup>27</sup> Lithium titanium oxide does find niche applications owing to an excellent rate capability but its high reduction potential of 1.5V versus lithium metal and low capacity (150mAh/g) significantly reduces energy density.<sup>28</sup> Any further

development in anode performance will require the incorporation of either lithium alloys or the metal itself whose capacities range from 1000 to 4200 mAh/g at reduction potentials of 0.5V and lower.

In this sense, lithium metal appears the obvious candidate however its main limiting features are safety characteristics. Namely, re-deposition of lithium during the charge phase occurs unevenly. Over time these form lithium dendrites (Figure 1.3) which can eventually pierce the separator and short circuit the cell.<sup>29</sup>

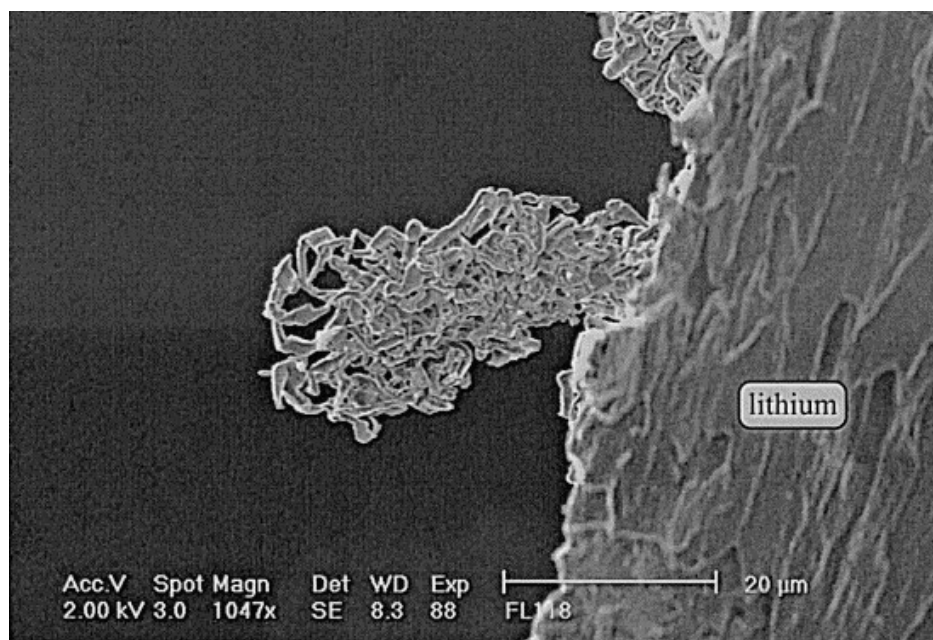


**Figure 1.3.** Representative lithium dendrite formation (Orsini, F.; Du Pasquier, A.; Beaudoin, B.; Tarascon, J. M.; Trentin, M.; Langenhuisen, N.; De Beer, E.; Notten, P. In *Situ Scanning Electron Microscopy (SEM) Observation of Interfaces within Plastic Lithium Batteries*. *J. Power Sources* **1998**, 76 (1), 19–29.) (Reproduced with permission from The Journal of Power Sources)

This would result in immediate cell failure and excessive heat production with the potential for an explosive event. While there is work ongoing to solve the issue of dendrite formation, lithium alloys represent a dendrite free alternative, though with significant caveats.

Silicon metal is the predominant lithium alloy anode with a large body of research surrounding it.<sup>30</sup> It has a theoretical capacity on the order of 4200 mAh/g based on a final alloy composition of  $\text{Li}_{22}\text{Si}_5$  with an insertion/de-insertion voltage of approximately 0.2V and 0.4V respectively. The lithiation of crystalline silicon does not proceed as a direct reaction to the final theoretical lithiation phase but rather is thought to occur in stages. Namely, a lithium rich reaction front approximating the  $\text{Li}_{22}\text{Si}_5$  stoichiometry develops. The reaction front is nanometers thick and in its wake leaves amorphous and increasingly more lithiated  $\text{Li}_x\text{Si}_x$  phases. This continues until the extent of lithiation approaches  $\text{Li}_{22}\text{Si}_5$  where sudden recrystallization of  $\text{Li}_{15}\text{Si}_4$  is instead suspected to occur.<sup>31</sup>

The primary drawback of silicon alloy anodes is the significant volume expansion of 300% upon full lithiation. The repeated expansion and contraction with repeated cycling can cause delamination of the anode from the current collector.<sup>32</sup> This is especially true when using the traditional PVDF binder which is not suited to accommodating such strain. More troublesome is the repeated fracturing of the SEI layer, promoting the formation of an excessively thick SEI which ultimately serves to electrically isolate the silicon particles from the conductive carbon matrix.<sup>33</sup>

Approaches to address this issue often include the use of additives, novel binders, encapsulation, silicon nanostructures, and others.<sup>34</sup> Alternatively, there has been recent

interest in silicon monoxide as a substitute for metallic silicon.<sup>35</sup> Its primary benefit over silicon metal is the 200% reduction in volume expansion while still retaining practical reversibility capacities of approximately 1000 mAh/g.<sup>36</sup> It achieves this through a microstructure consisting of intermixed SiO<sub>2</sub> and Si metal domains as opposed to a homogenous SiO phase.<sup>37</sup> Lithiation of the material results in the formation of Li<sub>4</sub>SiO<sub>4</sub> and Li<sub>2</sub>O in addition to the reversible Li<sub>x</sub>Si<sub>x</sub> phases.<sup>38</sup> The generation of Li<sub>4</sub>SiO<sub>4</sub> and Li<sub>2</sub>O is an irreversible process and consumes precious lithium derived from the cathode. However, the fact that it remains stable during cycling and is distributed throughout the anode allows it to function as an expansion buffer to the Li<sub>x</sub>Si<sub>x</sub>. So while the initial capacity decay is significant and inevitable, it substantially reduces capacity fade on subsequent cycles.

The research effort towards silicon monoxide as an LIB anode is only a fraction of that applied towards metallic silicon. This leaves a number of unanswered questions with regard to the specifics of its chemistry. For instance, a thorough experimental investigation on the identity of the Li<sub>x</sub>Si<sub>x</sub> phases has not been conducted. While it is implicitly assumed they follow a trend similar to silicon metal, this has not been explicitly confirmed. Features including crystalline/amorphous characteristics or how the lithium silicide domains are distributed amongst the lithium silicate buffer have captured limited attention. The majority of research which does exist on SiO anodes follows a synthetic approach with the primary purpose of testing performance and little emphasis on mechanistic aspects. NMR characterization of SiO is particularly sparse with only a

handful of studies having been conducted.<sup>39,40</sup> This state of affairs leaves substantial room for novel contributions.

### 1.2.3 - Electrolytes

The choice of electrolyte plays an exceedingly important role in overall performance. For an electrolyte to be considered ideal it must exhibit a wide range of physical properties including minimal flammability, low toxicity, good lithium ion conductivity, high dielectric constant, low freezing point, high oxidative stability, formation of stable SEI layers, and many more. No electrolyte yet discovered can cover all the desired points for an ideal electrolyte, but a specific chemistry has become the predominant solution. In particular, organic carbonate solvents containing weakly bonded lithium salts possess the right sets of properties. Of these 1M LiPF<sub>6</sub> in a combination of organic carbonate solvents is the standard.<sup>41</sup> Carbonate solvents have a wide liquid range and high dielectric constant coupled with the prerequisite oxidative stability and SEI formation potential. Additionally, LiPF<sub>6</sub> is a highly soluble, oxidatively stable, SEI forming lithium salt with an ionic conductivity in a 1M LiPF<sub>6</sub> ethylene carbonate/dimethyl carbonate (EC/DMC) mixture of over 10 mS/cm.

The current electrolyte solution does have drawbacks. Specifically the use of LiPF<sub>6</sub> represents an HF generation hazard, the EC/DMC solvent is flammable, insufficient oxidative stability beyond 4.9V versus lithium, drastically reduced performance at low temperature, and more. Research into better performing alternatives is primarily hindered by the requirement of a sufficiently stable SEI layer coupled with high oxidative stability.

This limits the list of potential candidates greatly and has driven interest in non-traditional solutions including ionic liquids<sup>42</sup>, solid electrolytes<sup>43</sup>, and deep eutectic electrolytes.<sup>44</sup>

The primary issue for alternative electrolytes is to achieve comparable diffusional characteristics while maintaining their positive benefits. Consider an ionic liquid, comprised solely of a mixture of cations and anions where a mismatch in the cation/anion size promotes their existence in a liquid state. They are typically comprised of components which have high oxidative stability and can be tailored to provide good SEI forming properties. Coupled with their relative non-flammability they appear to be attractive candidates. However, overall ionic conductivity generally falls short of their organic carbonate counterparts.<sup>45</sup> Also the fraction of the ionic conductivity contributed via lithium diffusion (e.g. the lithium transference number) is much lower in ionic liquids because of competition with the primary cation. The combination of low conductivity and lithium transport number conspire to severely hamper the adoption of ionic liquids despite their positive qualities.

Solid electrolytes are a means to circumvent the transference number issues. By virtue of their solid anionic matrix supporting diffusion of lithium cations, a pure solid electrolyte has by definition a lithium transference number of 1. This means that all ionic conductivity is the result of lithium ion diffusion. Unfortunately, ionic conductivity in solids is constrained by the limited mobility environment and results in an insufficient ionic conductivity, despite the sole contribution from lithium cations.

Deep eutectic electrolytes are generally less well studied than either ionic liquids or

deep eutectic electrolytes. They are typically comprised of a highly polar, small organic molecule coupled with a weakly coordinating lithium salt at molar ratios where the amount of the organic component and salt are comparable. The decrease in entropy promotes a freezing point depression in the mixture which can go substantially below the freezing point of either pure component.<sup>46</sup> A manifestation of this phenomenon is observed when a pure organic molecule, solid at room temperature, is mixed with a weakly coordinating solid lithium salt. In the right proportions these two components can yield a room temperature liquid. Expansion of the sample selection to solid organic species allows for the utilization components with high oxidative stability. Additionally, the high lithium salt content tends to promote anodic stability such that unstable organic molecules can become viable in a deep eutectic formulation.<sup>47</sup> Generally, they also possess total ionic conductivities at or above ionic liquids while maintaining lithium transference numbers greater than 0.5, in comparison to the  $\approx 0.4$  more typical of organic carbonate electrolytes.

To understand what factors determine the properties of deep eutectic liquids it is necessary to grasp the underlying solution state structure and dynamics. NMR is a particularly well suited tool to studying these types of materials. Primary constituents of deep eutectic electrolytes for lithium ion battery applications include  $^1\text{H}$ ,  $^7\text{Li}$ , and  $^{19}\text{F}$  nuclei, which are all distinguished by their high abundance and sensitivity to NMR measurements. Monitoring all three nuclei allows for chemical environment and diffusivity to be characterized. Additionally, use of the empirically collected diffusivity to

validate molecular dynamics simulations can provide unique insights into their solution state structure and how this impacts their transport properties.

#### **1.2.4 - Separators**

With their importance in electrical isolation and lithium ion conduction, the choice of separator plays an integral part in determining LIB performance. To achieve electrical isolation, the membrane must be sufficiently thick with low porosity and overall pore size. However, these are the direct opposite of the characteristics necessary for acceptable lithium ion conductivity.<sup>48</sup> Thus a compromise is reached depending on whether long cycle life applications or those requiring high power are desired. Other relevant parameters include mechanical strength, wettability, and the capacity to halt battery operation in the event of thermal runaway. And finally, it must be simultaneously resistant to the harsh oxidizing and reducing environment it is exposed to.

Almost all separators involve the use of semi-crystalline polyolefin materials including polyethylene, polypropylene, and blends therein. These are usually applied at thickness of approximately 25 microns with a porosity of 40%. They are optimized to achieve many of the required characteristics, but do so mainly at the expense of ionic conductivity. In fact, the presence of these separators can increase the effective resistance of the electrolyte by a factor of 4-5.

Some recent work has investigated the possibility of expanding the functionality of battery separators. Specifically, incorporation of transition metal chelating agents has been suggested as possible means to trap manganese cations.<sup>20</sup> This has important

consequences in the use of manganese containing cathodes as it would mitigate damage by trapping them in the separator before they reach the anode.

### **1.2.5 - Current Collectors**

The current collectors function as the substrate upon which the anode and cathode materials are deposited and as the name suggests facilitate the collection of electrical current to and from the active materials. Typical configurations include the anode and cathode cast on copper and aluminum foil respectively. While copper is not ideal due to its higher cost, the choice of current collector is dependent on how a candidate material behaves under oxidative/reductive conditions.

Aluminum would serve as a cheaper alternative to copper at the anode but it is not reductively stable. Specifically, at potentials below 0.6V versus lithium an Al-Li alloy reaction begins. Just as with Li-Si alloys, the Li-Al chemistry can be used as an anode material itself with a reversible capacity of 1000 mAh/g.<sup>49</sup> However, as with many other alloy chemistries, the associated volume expansion and contraction results in a rapid decay in reversible capacity.

The use of graphite as an anode material requires a dimensionally stable anode. Copper is substantially less reactive at the 0.1V versus lithium potential it is exposed to, making it suitable for use as an anode current collector. However, it is not oxidatively stable at potentials much beyond 3V versus lithium and results in copper dissolution into the electrolyte. Aluminum can also dissolve at high cathodic potentials, but this can be mitigated given the appropriate electrolyte. Specifically, the commonly used LiPF<sub>6</sub> salts

yields a stable passivation layer of aluminum fluoride which prevents further dissolution while maintaining electrical conductivity.<sup>50</sup>

While this makes aluminum suitable as a cathode material up to potentials of 5V versus lithium, this is only true for the LiPF<sub>6</sub> salt. Research into alternative lithium salts including, lithium triflate, lithium bis(trifluorosulfonyl)imide, and lithium bis(trifluoromethane)sulfonimide suggests the lack of an insoluble passivation layer on aluminum current collectors.<sup>51</sup> The end result is the rapid dissolution of the aluminum current collector. While the effect can be mitigated through the introduction of LiPF<sub>6</sub> as an additive it is nevertheless a concern when investigating alternatives to LiPF<sub>6</sub>.

### **1.3 - Thesis Overview**

As the previous sections have demonstrated, there are many avenues for further LIB research. Described in this document are select examples of the application of NMR to LIB research. It serves to demonstrate the versatility of NMR in its characterization of lithium ion batteries. To this end, isolated topics in LIB characterization are described which are all enabled by the relevant NMR measurements. It should be noted, however, that these only represent a small sampling of the kinds of NMR experiments that are possible.

Chapter 2 details the fundamentals of NMR including how the fundamental physical properties of atomic nuclei can determine the feasibility of a given NMR experiment. This chapter also includes a description of additional techniques used to supplement the information gathered through NMR.

Chapter 3 is an investigation of the transport properties for a specific deep eutectic

electrolyte formulation. By using NMR measurements of diffusion coefficients in combination with molecular dynamics (MD) simulations it describes the structure and properties of these understudied materials.

Chapter 4 describes a method to quantify the trapping of manganese ions by crown ethers via distinct changes in the  $^7\text{Li}$  chemical shift. It involves the fitting of the experimental data to an expression derived from the original equilibrium expressions in the fast exchange regime.

Chapters 5 investigates SiO and metallic silicon as LIB anode materials. They emphasize the use of in-situ  $^7\text{Li}$  NMR, ex-situ  $^{29}\text{Si}$  NMR and how these measurements were enabled through aqueous active material deposition on cellulosic substrates.

Chapter 6 represents a progress report on attempts to develop an in-situ lithium ion battery that can be wireless charged and discharged under magic angle spinning conditions.

Finally, chapter 7 summarizes the results of these investigations and lays the groundwork for further research.

#### **1.4 - References**

- (1) Change, I. P. on C. *Climate Change 2014 – Impacts, Adaptation and Vulnerability: Regional Aspects*; Cambridge University Press, 2014.
- (2) Hansen, J.; Ruedy, R.; Sato, M.; Lo, K. Global Surface Temperature Change. *Rev. Geophys.* **2010**, 48 (4), RG4004.

- (3) Doney, S. C.; Ruckelshaus, M.; Emmett Duffy, J.; Barry, J. P.; Chan, F.; English, C. A.; Galindo, H. M.; Grebmeier, J. M.; Hollowed, A. B.; Knowlton, N.; et al. Climate Change Impacts on Marine Ecosystems. *Annu. Rev. Mar. Sci.* **2012**, *4* (1), 11–37.
- (4) Church, J. A.; White, N. J. A 20th Century Acceleration in Global Sea-Level Rise. *Geophys. Res. Lett.* **2006**, *33* (1), L01602.
- (5) Hansen, J. E.; Sato, M. Paleoclimate Implications for Human-Made Climate Change. In *Climate Change*; Berger, A., Mesinger, F., Sijacki, D., Eds.; Springer Vienna, 2012; pp 21–47.
- (6) Sherwood, S. C.; Huber, M.; Emanuel, K. A. An Adaptability Limit to Climate Change due to Heat Stress. *Proc. Natl. Acad. Sci. U. S. A.* **2010**, *107* (21), 9552–9555.
- (7) Publication: Key World Energy Statistics 2015  
<http://www.iea.org/publications/freepublications/publication/key-world-energy-statistics-2015.html> (accessed Apr 25, 2016).
- (8) Hadjipaschalis, I.; Poullikkas, A.; Efthimiou, V. Overview of Current and Future Energy Storage Technologies for Electric Power Applications. *Renew. Sustain. Energy Rev.* **2009**, *13* (6–7), 1513–1522.
- (9) Thackeray, M. M.; Wolverton, C.; Isaacs, E. D. Electrical Energy Storage for Transportation—approaching the Limits Of, and Going Beyond, Lithium-Ion Batteries. *Energy Environ. Sci.* **2012**, *5* (7), 7854–7863.

- (10) Marom, R.; Amalraj, S. F.; Leifer, N.; Jacob, D.; Aurbach, D. A Review of Advanced and Practical Lithium Battery Materials. *J. Mater. Chem.* **2011**, *21* (27), 9938–9954.
- (11) Schaefer, J. L.; Lu, Y.; Moganty, S. S.; Agarwal, P.; Jayaprakash, N.; Archer, L. A. Electrolytes for High-Energy Lithium Batteries. *Appl. Nanosci.* **2012**, *2* (2), 91–109.
- (12) Käbitz, S.; Gerschler, J. B.; Ecker, M.; Yurdagel, Y.; Emmermacher, B.; André, D.; Mitsch, T.; Sauer, D. U. Cycle and Calendar Life Study of a graphite|LiNi<sub>1/3</sub>Mn<sub>1/3</sub>Co<sub>1/3</sub>O<sub>2</sub> Li-Ion High Energy System. Part A: Full Cell Characterization. *J. Power Sources* **2013**, (239), 572–583.
- (13) Lee, H.; Choi, S.; Choi, S.; Kim, H.-J.; Choi, Y.; Yoon, S.; Cho, J.-J. SEI Layer-Forming Additives for LiNi<sub>0.5</sub>Mn<sub>1.5</sub>O<sub>4</sub>/graphite 5 V Li-Ion Batteries. *Electrochem. Commun.* **2007**, *9* (4), 801–806.
- (14) Xu, J.; Chou, S.-L.; Gu, Q.; Liu, H.-K.; Dou, S.-X. The Effect of Different Binders on Electrochemical Properties of LiNi<sub>1/3</sub>Mn<sub>1/3</sub>Co<sub>1/3</sub>O<sub>2</sub> Cathode Material in Lithium Ion Batteries. *J. Power Sources* **2013**, (225), 172–178.
- (15) Patoux, S.; Sannier, L.; Lignier, H.; Reynier, Y.; Bourbon, C.; Jouanneau, S.; Le Cras, F.; Martinet, S. High Voltage Nickel Manganese Spinel Oxides for Li-Ion Batteries. *Electrochimica Acta* **2008**, *53* (12), 4137–4145.
- (16) Arora, P.; White, R. E.; Doyle, M. Capacity Fade Mechanisms and Side Reactions in Lithium-Ion Batteries. *J. Electrochem. Soc.* **1998**, *145* (10), 3647–3667.

- (17) Xiao, X.; Liu, Z.; Baggetto, L.; Veith, G. M.; More, K. L.; Unocic, R. R. Unraveling Manganese Dissolution/deposition Mechanisms on the Negative Electrode in Lithium Ion Batteries. *Phys. Chem. Chem. Phys.* **2014**, *16* (22), 10398–10402.
- (18) Gummow, R. J.; de Kock, A.; Thackeray, M. M. Improved Capacity Retention in Rechargeable 4 V Lithium/lithium-Manganese Oxide (Spinel) Cells. *Solid State Ion.* **1994**, *69* (1), 59–67.
- (19) Jang, D. H.; Shin, Y. J.; Oh, S. M. Dissolution of Spinel Oxides and Capacity Losses in 4 V Li / Li X Mn<sub>2</sub> O<sub>4</sub> Cells. *J. Electrochem. Soc.* **1996**, *143* (7), 2204–2211.
- (20) Li, Z.; Pauric, A. D.; Goward, G. R.; Fuller, T. J.; Ziegelbauer, J. M.; Balogh, M. P.; Halalay, I. C. Manganese Sequestration and Improved High-Temperature Cycling of Li-Ion Batteries by Polymeric Aza-15-Crown-5. *J. Power Sources* **2014**, *272*, 1134–1141.
- (21) Yi, T.-F.; Zhu, Y.-R.; Zhu, X.-D.; Shu, J.; Yue, C.-B.; Zhou, A.-N. A Review of Recent Developments in the Surface Modification of LiMn<sub>2</sub>O<sub>4</sub> as Cathode Material of Power Lithium-Ion Battery. *Ionics* **2009**, *15* (6), 779–784.
- (22) Wang, R.; Li, X.; Wang, Z.; Guo, H. Manganese Dissolution from LiMn<sub>2</sub>O<sub>4</sub> Cathodes at Elevated Temperature: Methylene Methanedisulfonate as Electrolyte Additive. *J. Solid State Electrochem.* **2015**, *20* (1), 19–28.
- (23) Ziv, B.; Levy, N.; Borgel, V.; Li, Z.; Levi, M. D.; Aurbach, D.; Pauric, A. D.; Goward, G. R.; Fuller, T. J.; Balogh, M. P.; et al. Manganese Sequestration and Li-Ion

Batteries Durability Enhancement by Polymeric 18-Crown-6 Ethers. *J. Electrochem. Soc.* **2014**, *161* (9), A1213–A1217.

(24) Bradshaw, J. S.; Izatt, R. M. Crown Ethers: The Search for Selective Ion Ligating Agents. *Acc. Chem. Res.* **1997**, *30* (8), 338–345.

(25) Manthiram, A.; Fu, Y.; Chung, S.-H.; Zu, C.; Su, Y.-S. Rechargeable Lithium–Sulfur Batteries. *Chem. Rev.* **2014**, *114* (23), 11751–11787.

(26) Girishkumar, G.; McCloskey, B.; Luntz, A. C.; Swanson, S.; Wilcke, W. Lithium–Air Battery: Promise and Challenges. *J. Phys. Chem. Lett.* **2010**, *1* (14), 2193–2203.

(27) Aurbach, D.; Markovsky, B.; Weissman, I.; Levi, E.; Ein-Eli, Y. On the Correlation between Surface Chemistry and Performance of Graphite Negative Electrodes for Li Ion Batteries. *Electrochimica Acta* **1999**, *45* (1–2), 67–86.

(28) Yang, Z.; Choi, D.; Kerisit, S.; Rosso, K. M.; Wang, D.; Zhang, J.; Graff, G.; Liu, J. Nanostructures and Lithium Electrochemical Reactivity of Lithium Titanites and Titanium Oxides: A Review. *J. Power Sources* **2009**, *192* (2), 588–598.

(29) Li, Z.; Huang, J.; Yann Liaw, B.; Metzler, V.; Zhang, J. A Review of Lithium Deposition in Lithium-Ion and Lithium Metal Secondary Batteries. *J. Power Sources* **2014**, (254), 168–182.

- (30) Su, X.; Wu, Q.; Li, J.; Xiao, X.; Lott, A.; Lu, W.; Sheldon, B. W.; Wu, J. Silicon-Based Nanomaterials for Lithium-Ion Batteries: A Review. *Adv. Energy Mater.* **2014**, *4* (1).
- (31) McDowell, M. T.; Lee, S. W.; Nix, W. D.; Cui, Y. 25th Anniversary Article: Understanding the Lithiation of Silicon and Other Alloying Anodes for Lithium-Ion Batteries. *Adv. Mater.* **2013**, *25* (36), 4966–4985.
- (32) Teki, R.; Datta, M. K.; Krishnan, R.; Parker, T. C.; Lu, T.-M.; Kumta, P. N.; Koratkar, N. Nanostructured Silicon Anodes for Lithium Ion Rechargeable Batteries. *Small* **2009**, *5* (20), 2236–2242.
- (33) Wu, H.; Cui, Y. Designing Nanostructured Si Anodes for High Energy Lithium Ion Batteries. *Nano Today* **2012**, *7* (5), 414–429.
- (34) Ma, D.; Cao, Z.; Hu, A. Si-Based Anode Materials for Li-Ion Batteries: A Mini Review. *Nano-Micro Lett.* **2014**, *6* (4), 347–358.
- (35) Miyachi, M.; Yamamoto, H.; Kawai, H.; Ohta, T.; Shirakata, M. Analysis of SiO Anodes for Lithium-Ion Batteries. *J. Electrochem. Soc.* **2005**, *152* (10), A2089–A2091.
- (36) Feng, X.; Yang, J.; Yu, X.; Wang, J.; Nuli, Y. Low-Cost SiO-Based Anode Using Green Binders for Lithium Ion Batteries. *J. Solid State Electrochem.* **2013**, *17* (9), 2461–2469.
- (37) Friede, B.; Jansen, M. Some Comments on so-Called “silicon Monoxide.” *J. Non-Cryst. Solids* **1996**, *204* (2), 202–203.

- (38) Jung, S. C.; Kim, H.-J.; Kim, J.-H.; Han, Y.-K. Atomic-Level Understanding toward a High-Capacity and High-Power Silicon Oxide (SiO) Material. *J. Phys. Chem. C* **2016**, *120* (2), 886–892.
- (39) Kim, T.; Park, S.; Oh, S. M. Solid-State NMR and Electrochemical Dilatometry Study on Li + Uptake/Extraction Mechanism in SiO Electrode. *J. Electrochem. Soc.* **2007**, *154* (12), A1112–A1117.
- (40) Kim, J.-H.; Park, C.-M.; Kim, H.; Kim, Y.-J.; Sohn, H.-J. Electrochemical Behavior of SiO Anode for Li Secondary Batteries. *J. Electroanal. Chem.* **2011**, *661* (1), 245–249.
- (41) Aurbach, D.; Talyosef, Y.; Markovsky, B.; Markevich, E.; Zinigrad, E.; Asraf, L.; Gnanaraj, J. S.; Kim, H.-J. Design of Electrolyte Solutions for Li and Li-Ion Batteries: A Review. *Electrochimica Acta* **2004**, *50* (2–3), 247–254.
- (42) Ishikawa, M.; Sugimoto, T.; Kikuta, M.; Ishiko, E.; Kono, M. Pure Ionic Liquid Electrolytes Compatible with a Graphitized Carbon Negative Electrode in Rechargeable Lithium-Ion Batteries. *J. Power Sources* **2006**, *162* (1), 658–662.
- (43) Fergus, J. W. Ceramic and Polymeric Solid Electrolytes for Lithium-Ion Batteries. *J. Power Sources*, **2010**, *195* (15), 4554–4569.
- (44) Boisset, A.; Menne, S.; Jacquemin, J.; Balducci, A.; Anouti, M. Deep Eutectic Solvents Based on N-Methylacetamide and a Lithium Salt as Suitable Electrolytes for Lithium-Ion Batteries. *Phys. Chem. Chem. Phys.* **2013**, *15* (46), 20054–20063.

- (45) Matsumoto, H. Recent Advances in Ionic Liquids for Lithium Secondary Batteries. In *Electrolytes for Lithium and Lithium-Ion Batteries*; Jow, T. R., Xu, K., Borodin, O., Ue, M., Eds.; Modern Aspects of Electrochemistry; Springer New York, 2014; pp 209–225.
- (46) Abbott, A. P.; Boothby, D.; Capper, G.; Davies, D. L.; Rasheed, R. K. Deep Eutectic Solvents Formed between Choline Chloride and Carboxylic Acids: Versatile Alternatives to Ionic Liquids. *J. Am. Chem. Soc.* **2004**, *126* (29), 9142–9147.
- (47) Yamada, Y.; Furukawa, K.; Sodeyama, K.; Kikuchi, K.; Yaegashi, M.; Tateyama, Y.; Yamada, A. Unusual Stability of Acetonitrile-Based Superconcentrated Electrolytes for Fast-Charging Lithium-Ion Batteries. *J. Am. Chem. Soc.* **2014**, *136* (13), 5039–5046.
- (48) Zhang, S. S. A Review on the Separators of Liquid Electrolyte Li-Ion Batteries. *J. Power Sources* **2007**, *164* (1), 351–364.
- (49) Kuksenko, S. P. Aluminum Foil as Anode Material of Lithium-Ion Batteries: Effect of Electrolyte Compositions on Cycling Parameters. *Russ. J. Electrochem.* **2013**, *49* (1), 67–75.
- (50) Myung, S.-T.; Hitoshi, Y.; Sun, Y.-K. Electrochemical Behavior and Passivation of Current Collectors in Lithium-Ion Batteries. *J. Mater. Chem.* **2011**, *21* (27), 9891–9911.
- (51) Krämer, E.; Schedlbauer, T.; Hoffmann, B.; Terborg, L.; Nowak, S.; Gores, H. J.; Passerini, S.; Winter, M. Mechanism of Anodic Dissolution of the Aluminum Current

Collector in 1 M LiTFSI EC:DEC 3:7 in Rechargeable Lithium Batteries. *J. Electrochem.*

*Soc.* **2013**, *160* (2), A356–A360.



## Chapter 2: Introduction to Nuclear Magnetic Resonance

### 2.1 – Fundamentals of Nuclear Magnetic Resonance Spectroscopy

Spectroscopy in the broadest sense is concerned with investigating interactions between light and matter. One of its foremost uses is in the characterization of chemical species using the entire breadth of the electromagnetic spectrum. To illustrate this utility, infrared (IR) spectroscopy serves as a convenient example. In an IR spectrometer, the sample of interest is irradiated through sweeping over a narrow range of IR frequencies. Any decrease in light intensity as a function of the applied frequency corresponds to absorption bands characteristic of the sample. The decreased intensity arises from the excitement of vibrational transitions. These transitions are a consequence of the energy required to effect vibrational motion such as the stretching of chemical bonds. The Planck-Einstein relation (eq. 1) relates the frequency of the light applied to energy where  $E$  corresponds to energy,  $\nu$  to the frequency, and  $h$  to the Planck constant.

$$(1) \quad E = h\nu$$

Since vibrational energy levels are quantized, when a photon with the specific energy required interacts with the sample it can excite a vibrational transition (Figure 2.1). This is observed as a decrease in signal intensity as the photon energy is converted into the kinetic energy of the vibration.<sup>1</sup> The collection of vibrational modes ultimately serves as the vibrational “fingerprint” for the molecule and allows for insight into the chemical structure of the sample.

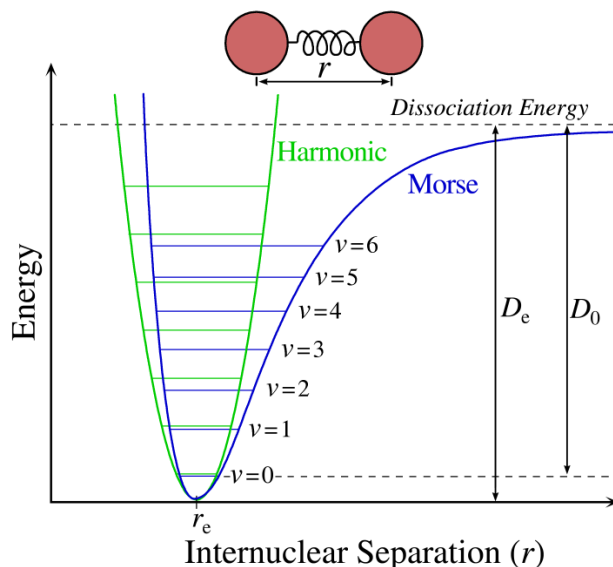


**Figure 2.1.** The Morse potential (blue) and harmonic oscillator potential (green). The potential at infinite internuclear distance is the dissociation energy for pure vibrational spectra. For vibronic spectra there are two potential curves and the dissociation limit is the *upper* state energy at infinite distance. (Used with permission from Mark Somoza via Wikipedia under the CC BY-SA 3.0 License)

Many other spectroscopies operate on the same principle, whether that is rotational transitions in the microwave regime or electronic transitions in the ultraviolet; they are all related through the observation of discrete transitions. However, these spectroscopies probe systems which naturally possess non-degeneracy. NMR spectroscopy differs from this trend such that the energy levels of the associated nuclear transitions are degenerate except for under the influence of an external magnetic field. To understand how this degeneracy is broken for the purposes of spectroscopy, it is important to consider the fundamentals of nuclear transitions.

An atomic nucleus (with the notable exception of hydrogen) is comprised of a number of protons and neutrons which are held together via the strong nuclear force. Similar to the electrons which surround the nucleus, the nucleons possess a certain intrinsic angular momentum which is characterized by its spin or  $I$ . The individual protons and neutrons can assume half integral values of spin with  $I = \pm\frac{1}{2}$ .<sup>2</sup> The sum of the individual spins across the entire nucleus dictates the ultimate aggregate value for the nuclear spin. A more thorough explanation of this is beyond the scope of this chapter, though from an empirical standpoint, a nucleus with an odd number of nucleons must add to a half integer value for  $I$ , whereas even numbered nuclei must add to a whole integer. If the sum of the nuclear spins is  $I > 0$ , then the nucleus possesses a magnetic moment which can be manipulated. The simplest case of these is the spin  $\frac{1}{2}$  nucleus which will be sufficient for the purposes of this discussion.

A nucleus with a spin  $I = \frac{1}{2}$  (e.g.  $^1\text{H}$ ) does not typically exhibit an energetic preference for either the positive or negative spin state. To perform useful spectroscopy the degeneracy must be broken such that a preference for one spin state over the other is created. This is done through the application of an external magnetic field.<sup>3</sup> It creates an energetic preference for spin  $\frac{1}{2}$  nuclei to orient themselves in the same direction as the external magnetic field. The potential energy for a nucleus being with (spin-up) versus against (spin-down) the external magnetic field is called the Zeeman energy and is exemplified in Figure 2.<sup>3</sup>

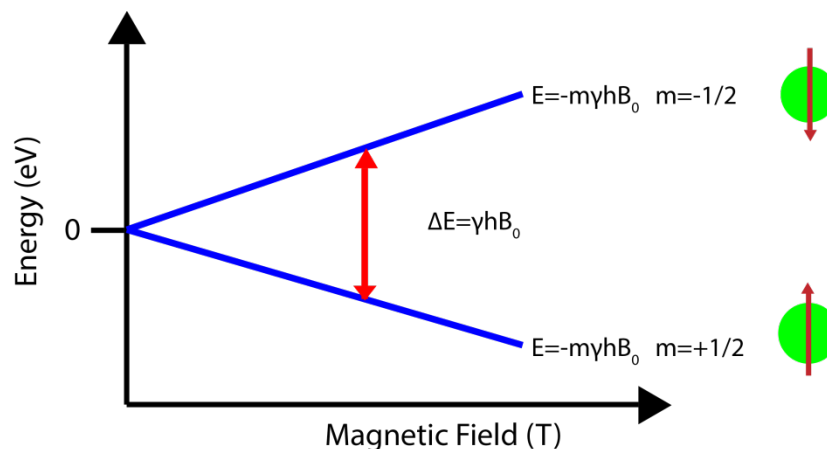


**Figure 2.2.** Zeeman splitting diagram for a spin  $\frac{1}{2}$  nucleus placed in a magnetic field. Used with permission from UC-Davis University of California under the CC NC-SA 3.0 License. Contributors include Derrick Kaseman and Revathi Srinivasan Ganesh Lyer. Figure is available through the following URL:  
[http://chem.libretexts.org/Core/Physical\\_Chemistry/Spectroscopy/Magnetic\\_Resonance\\_Spectroscopies/Nuclear\\_Magnetic\\_Resonance/Nuclear\\_Magnetic\\_Resonance\\_II](http://chem.libretexts.org/Core/Physical_Chemistry/Spectroscopy/Magnetic_Resonance_Spectroscopies/Nuclear_Magnetic_Resonance/Nuclear_Magnetic_Resonance_II)

Typically this energy corresponds to photon frequencies in the tens to hundreds of MHz regime. However, the potential energy difference is on the order of a thousand times less than the available thermal energy at room temperature. A primary consequence of this is the weak polarization characteristic to NMR which for a given  $^1\text{H}$  sample is on the order of parts per million. This has severe implications on the achievable signal to noise (S/N) ratio as it is only the aligned protons which can be brought to an excited state. Nevertheless the polarization is sufficient to produce a net magnetic dipole which precesses about the external field at a characteristic frequency known as its Larmor

frequency (eq. 2). Here the frequency  $\omega$  is the product of the gyromagnetic ratio  $\gamma$  and the magnitude of the external magnetic field  $B$ .<sup>4</sup>

$$(2) \quad \omega = -\gamma B$$

At a given field strength  $B$ , the value for  $\gamma$  determines the precession frequency which have been tabulated for all stable nuclei with magnetic moments.

An external magnetic field breaks the associated nuclear degeneracy to create a net polarization observable as a macroscopic magnetic moment. The lowest energy state of the system is that in which net magnetization exists in the direction of the external magnetic field. To observe an NMR signal a radio frequency (RF) pulse corresponding to the Zeeman energy is applied. The resulting relaxation of the net magnetic moment as it precesses back to equilibrium is detected as an oscillating voltage signal through electronic induction in the metallic detection coil.<sup>5</sup> This continues until the signal has fully relaxed back to its equilibrium state. The entirety of the oscillating signal plotted as a function of relaxation time is termed the free induction decay (FID)

The FID thus acquired is typically Fourier transformed to reveal the range of frequencies characteristic to the sample as distinct lineshapes. For a spin  $\frac{1}{2}$  nucleus the Zeeman interaction is of the largest significance showing up at a frequency value characteristic to the Larmor frequency of the nucleus. However, upon closer inspection the corresponding lineshape is often split by other interactions. One of the most useful for chemists is the effect of electron density about the nucleus.

Chemical shift is a consequence of the influence that moving electrons have on the

magnetic field observed at the nucleus. This arises from the imposition of the external magnetic field on the circulating electrons. Specifically, additional motion about the direction of the magnetic field is superimposed on their normal behaviour. In doing so the electrons generate a local net magnetic field that functions in opposition to the applied external field.<sup>6</sup> The reduced magnetic field intensity has a direct impact on the nuclei causing a reduction in the Larmor frequency.

Overall the effect is small with the impact on Larmor frequency measurable to the ppm scale. Nevertheless the difference is substantial enough to differentiate nuclei in electron rich versus electron poor environments. Since structure and bonding is intimately tied with the electron density distribution there are profound implications for the detailed characterization of molecules. It is difficult to overstate how enormously useful chemical shift detection is to various chemical disciplines. It finds the most widespread use in small molecule characterization where it is commonly used towards identification of novel compounds. Other more specialized applications include characterization of proteins,<sup>7</sup> amorphous solids,<sup>8</sup> single crystals, complex mixtures,<sup>9</sup> and others. Besides simple chemical shift assignment, the long lifetimes of the excited state allow for a significant period within which it is possible to perform numerous RF manipulations, enabling some highly complex yet informative experiments. The broader NMR literature describes this in extensive detail,<sup>10</sup> but for the purpose of this document only the techniques that were of importance to the work presented here are discussed.

### 2.1.1 - Solution State NMR

Chemical shift measurements under ideal conditions allow for the resolution of individual nuclei in chemically distinct electronic environments. These conditions exist when the predominant factor influencing the distribution of larmor frequencies is the electron density. There are other factors which can cause a much wider distribution of chemical shifts and would overwhelm the contribution of electron shielding. Chemical shielding anisotropy (CSA) is one example of this.<sup>11</sup>

In a polycrystalline solid, individual crystallites are oriented across all possible angles with respect to the magnetic field. Since the electronic environment about a nucleus is often asymmetric, the result is a chemical shift dependence on orientation. This chemical shift orientation dependence is termed the CSA and can broaden signals so significantly that subtle differences in their structure are difficult to ascertain. Fortunately, analysis in the solution state can circumvent this problem as the rapid molecular tumbling enabled in liquids rotates individual nuclei across all possible orientations. This ultimately results in the collapse of the CSA to a single isotropic chemical shift value. The rapid tumbling also averages out dipolar coupling and significantly reduces line broadening in quadrupolar nuclei. Equations detailing these interactions are presented in section 2.1.4 (eq. 5).

Solution state NMR experiments take advantage of the orientational average to yield data with extraordinary resolution. The molecular structure of small molecules can be elucidated completely with each chemically distinct nucleus yielding lineshapes that are almost completely resolved from the other signals.<sup>12</sup> Furthermore, the application of

advanced 1D, as well as 2D and 3D pulse sequences dramatically increases the information obtainable beyond simple chemical shift information.

Of particular importance to the work presented here is the utility of solution state NMR in assessing cation trapping by crown ethers. Specifically, crown ethers covalently attached to a polymeric backbone had been shown to be amenable towards the selective trapping of manganese cations in a lithium electrolyte solution.<sup>13</sup> As the dissolution of manganese from the commonly utilized cathode materials is linked to severe capacity fade,<sup>14</sup> immobilizing it would provide a large boost to capacity retention. Solution state NMR measurements were used as a screening method in this context to assess the relative affinity of crown ethers to manganese versus lithium. The sharp resonances arising from the rapid molecular tumbling allowed for the detection of subtle changes in chemical shift, thus providing insight into the bonding environment. Further detail on this topic is described in Chapter 4.

### **2.1.2 - Diffusion NMR**

Besides the chemical and structural information typically obtained via NMR, it is possible to obtain dynamical information. Among these are diffusion coefficient measurements where the average displacement of the measured nuclei is measured. To measure the displacement of a nucleus requires a means to spatially label the sample volume being measured. Under typical circumstances all locations in the sample volume experience the same magnetic field strength. However, through the application of a short electromagnetic pulse a linear magnetic field gradient can be created (e.g. pulsed field

gradient or PFG).

The generation of a linear field gradient causes a systematic change in the Larmor frequency of the affected nuclei as a function of position. If a nucleus moves within the field gradient it is not refocused properly and results in signal attenuation.<sup>15</sup> The magnitude of the attenuation at a given strength of the field gradient is directly correlated to a diffusion coefficient. An illustration of a typical pulse sequence for the measurement of diffusion is depicted in Figure 2.3.<sup>16</sup>

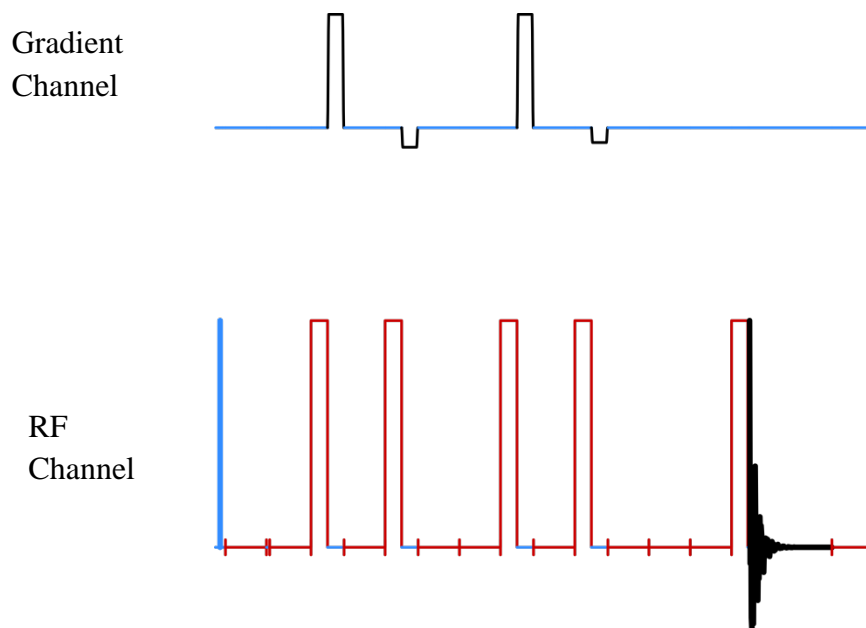


**Figure 2.3.** Longitudinal eddy current delay gradient pulse (LEDGP2S), pulse sequence

The pulse sequence begins with a  $90^\circ$  RF pulse on the nucleus channel followed immediately by a gradient pulse. This creates the spatially dependent distribution of

Larmor frequencies. Shortly after the gradient pulse, a second  $90^\circ$  pulse is applied to bring the magnetization vector into Z storage. This is an important step as it mitigates the effect of  $T_2$  related decoherence which could significantly reduce signal intensity during the diffusion waiting period. Immediately following Z storage is a spoiler gradient of opposite sign and limited intensity to correct for any errors in the first gradient pulse. During the subsequent diffusion waiting period those spins which have been labeled with the Larmor frequency of their original location have the opportunity to diffuse across the sample volume. Immediately after the waiting period are the refocusing gradient and RF pulses which only affect those nuclei which have not moved significantly during the diffusion period. A final RF pulse and acquisition at the end of the experiment yields a reduced signal intensity that is directly related to the diffusivity of the species in question (eq. 3).<sup>16</sup>

$$(3) \quad I_F = I_0 \cdot e^{(-D \cdot \sqrt{(2 \cdot \pi \cdot \gamma \cdot G \cdot \delta)} \cdot \frac{(\Delta - \delta)}{3})}$$

The constants include the diffusion delay ( $\Delta$ ), gradient pulse length ( $\delta$ ), gyromagnetic ratio ( $\gamma$ ), and the initial signal intensity ( $I_0$ ). The signal intensity ( $I_F$ ) is measured as a function of the gradient strength ( $G$ ), and the resultant exponential curve fitted to the corresponding diffusion coefficient ( $D$ ). An example of this curve fitting is shown in Figure 2.4.

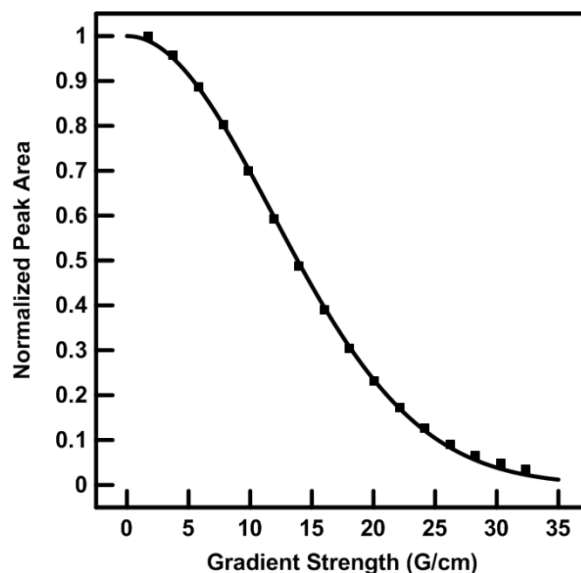


**Figure 2.4.** Example of curve fitting for the diffusion coefficient using data for  $^7\text{Li}$  in a 50/50 wt% ethylene carbonate/dimethyl carbonate solution of 1M  $\text{LiPF}_6$

The information obtained through PFG-NMR on diffusion coefficients can provide significant information on the associated dynamics.<sup>17</sup> In particular, this type of analysis was employed in Chapter 3 to investigate alternatives to lithium ion battery electrolytes. Diffusion coefficients thus obtained were used to both validate the molecular dynamics simulations and analyze diffusion trends in their own right.

### 2.1.3 - Molecular Dynamics

Molecular dynamics represent a computer simulation method whereby chemical species are represented by rigid spheres and bonds and their interaction approximated using classical mechanics. While this has the clear drawback of not properly representing chemical reactions, it has the advantage of being much easier to simulate. Whereas

computational methods based on quantum mechanics struggle in the range of hundreds of atoms, molecular dynamics routinely simulate system of over 100,000 atoms with ease.<sup>18</sup> For systems where aggregate properties are desired and the important considerations are primarily electrostatic, molecular dynamics provides a convenient way to obtain structural and dynamical information at macroscopically relevant scales.

Building an MD simulation requires first that a starting configuration of molecules with their associated connectivities is constructed. This begins with the atomic parameters which involve basic information on the size of the individual atoms or ions being considered. Next, the connectivities need to be established, which requires knowledge of bond lengths, angles, dihedrals and the partial charges of the atoms involved. Typically this information is obtained through a combination of quantum mechanical simulations and associated experimental data to verify the calculations.

After constructing the molecular geometry, the resultant molecules need to be arranged properly in the simulation space. For a solid this typically means starting from the crystal structure and proceeding accordingly, however, liquids require a different consideration. Namely, since long range order is generally absent in liquids the molecules have to be arranged randomly in the simulation space and this requires an appropriately constructed algorithm to achieve.<sup>20</sup>

With an adequately sized system in place it is necessary to define the interaction energies which will determine how the simulation evolves with time. These involve kinetic and potential energy terms which govern the interactions. An example of one such

energy term is the Lennard-Jones potential<sup>20</sup> which approximates the Van-Der-Waals interaction between neutral atoms or molecules.

$$(4) \quad V_{LJ} = 4\epsilon \left[ \left( \frac{\sigma}{r} \right)^{12} - \left( \frac{\sigma}{r} \right)^6 \right]$$

The terms described include  $\epsilon$  or the depth of the potential energy well,  $\sigma$ , the singular point at which the interatomic potential is zero, and  $r$ , the distance between the particles. Other considerations include the electrostatic potential and factors which include the influence of polarizability. Taken together the assembly of interatomic potentials, atomic and molecular parameters are termed the force field. Dozens of different force fields have been developed for various applications with some of the more recent work including polarizable force fields<sup>21</sup> and quantum mechanics/molecular mechanics hybrid forcefields.<sup>22</sup>

Molecular dynamics has been applied to a range of different problems including protein dynamics<sup>23</sup> determination to interfacial chemistry.<sup>24</sup> Of particular importance to the work presented in this thesis are details surrounding the MD simulation of liquids, and specifically of lithium electrolyte solutions and ionic liquids. One of the most widely used force-fields to model such substances is the optimized potentials for liquid simulations, all atom variant (OPLS-AA).<sup>25</sup> The standard implementation includes explicit treatment of bond lengths, angles and dihedrals, while including a non-bonded component which describes van-der-Waals interactions and coulombic forces. Its popularity has resulted in a wide range of parameter sets for various molecules.<sup>26-28</sup>

However, despite examples of success in modeling lithium electrolyte solutions<sup>29</sup> there are still discrepancies between the physical properties predicted by MD simulations and experimentally determined values, especially for highly concentrated solutions, as is the case for ionic liquids. As alluded to previously, the inclusion of polarizability into the force field such as with OPLS-AAP variant<sup>29</sup> or the APPLE&P forcefield<sup>31</sup>, has yielded improved accuracy for such systems and is the subject of ongoing development.

These developments, while often focused on ionic liquids, can also be applied to the characterization of a substantially less well known electrolyte class termed deep eutectic solvent (DES) or deep eutectic electrolyte (DEE).<sup>32</sup> This class of electrolyte is characterized through the extreme melting point depression observed upon the mixing of a highly polar small organic molecule and a weakly associating ionic salt in an appropriate ratio. The resulting increase in entropy is sufficient to enable melting point depression on the order of 100°C below that of the pure components. The choice of the two components and resultant mixture can have properties which promote electrochemical stability and minimize flammability, important considerations for a lithium ion battery electrolyte.

MD simulation parameters optimized for ionic liquids are still particularly relevant for DES. Many of the anions used for ionic liquids such as bistrifluorosulfonamide (TFSI) are characterized by significant charge delocalization. This property makes them capable of supporting a large melting point depression. However, where a polarizable model does not exist for the chemical species of interest, it is possible to substitute via an overall charge scaling methodology.<sup>33</sup> This accounts for the anomalously low transport properties

for MD simulations of DEEs or ionic liquids by reducing the coulombic charge of all species by a constant fraction. To determine the extent of this fraction and to validate the resultant structure, it is useful to couple these simulations with experimental parameters. In particular a comparison can be made to macroscopically measured properties including density or molecular diffusivity. Towards this end NMR is well suited to measure the diffusivities of liquids modeled through MD. The capacity for NMR to measure the individual diffusion coefficients for all the components of a given ionic liquid or DES provides a large set of variables by which the simulation can be parameterized. This procedure is described in further detail within Chapter 3.

#### **2.1.4 - MAS-NMR**

Unlike solution state NMR, characterization of solids introduces additional complications. In addition to the prevalence of CSA effects, dipolar coupling and quadrupole effects can serve to generate linewidths which greatly reduce spectral resolution.<sup>34</sup> However, the presence of these extra coupling effects can also yield important information as to their solid connectivity and local structure. The key to both obtaining spectral resolution while retaining information of solid state structure comes through the use of magic angle spinning (MAS).

The use of MAS serves to mimic the effects of rapid molecular tumbling in the solution state by spinning a solid sample at exactly  $54.74^\circ$  with respect to the external magnetic field (Figure 2.5). Note that the present figure includes the depiction of magic

angle gradient coils which while note a standard configuration can allow for the same diffusion experiments encountered in solution state experiments.

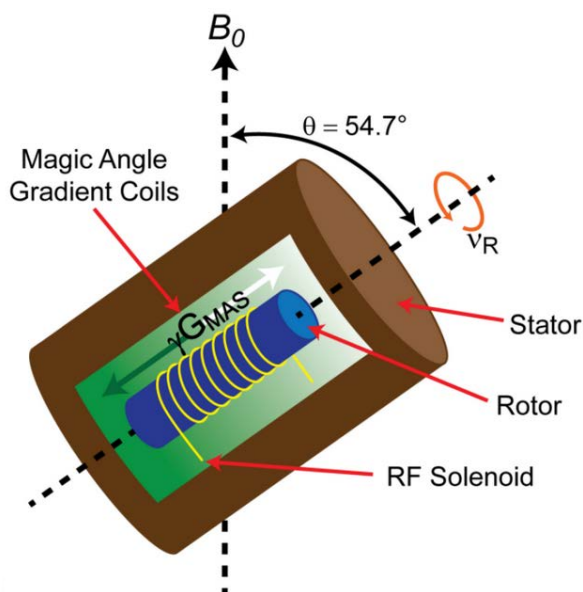


**Figure 2.5.** Schematic of a HR-MAS stator depicted with the additional inclusion of gradient coils orientated along the magic angle. (Todd M. Alam and Janelle E. Jenkins (2012). HR-MAS NMR Spectroscopy in Material Science, Advanced Aspects of Spectroscopy, Dr. Muhammad Akhyar Farrukh (Ed.), InTech, DOI: 10.5772/48340. Available from: <http://www.intechopen.com/books/advanced-aspects-of-spectroscopy/hr-mas-nmr-spectroscopy-in-material-science>)

The angle dependence of MAS can be noted from the time independent Hamiltonians associated with the interactions.<sup>35</sup>

$$\begin{aligned}
 H_{cs} &= \left( \omega \sigma_{iso} + \frac{\omega \sigma_{\sigma}}{2} \cdot [(3 \cdot \cos^2 \theta - 1) - \eta_{\sigma} \sin^2 \theta \cos 2\phi] \right) \cdot I_z \\
 (5) \quad H_Q^{(1)} &= \frac{e V_{zz} Q}{4I(2I-1)\hbar} - [(3 \cdot \cos^2 \theta - 1) - \eta_{\sigma} \sin^2 \theta \cos 2\phi] \cdot 3(I_z^2 - I^2) \\
 H_D^{(1)} &= \frac{\mu_0 \gamma_I \gamma_S \hbar}{4\pi r_{IS}^3} \cdot \frac{(3 \cdot \cos^2 \theta - 1)}{2} \cdot \begin{cases} 3I_{IZ}I_{SZ} - (I_I \cdot I_S) & \text{if } I = S \\ 2I_{IZ}I_{SZ} & \text{if } I \neq S \end{cases}
 \end{aligned}$$

The variables described include the Larmor frequency  $\omega$ , isotropic chemical shift  $\sigma_{iso}$ , chemical shielding anisotropy (CSA)  $\sigma_{\sigma}$ , the asymmetry parameter  $\eta_{\sigma}$  electronic charge  $e$ , the largest component of the electric field gradient tensor  $V_{zz}$ , reduced Planck constant  $\hbar$ , the gyromagnetic ratios of two spins  $I$  and  $S$  represented using the same symbols, the orientation of the spin with respect to the magnetic field axis,  $\theta$ , and the x-y plane,  $\phi$ . The terms involving  $(3 \cdot \cos^2 \theta - 1)$  go to zero at the magic angle whereas other spatially dependent terms can be partially or completely averaged with sufficiently fast spinning to yield the isotropic chemical shift.

However, achieving the spinning speeds sufficient to completely average out certain interactions can be quite challenging as alluded to in their relative magnitude (Table 1).

Interaction	Magnitude (Hz)
Zeeman	$10^8$
Quadrupolar	$10^6$
Chemical Shift	$10^3$
Dipole	$10^3$
J	$10^1$

**Table 2.1.** Relative magnitudes of different interactions that influence the NMR spectra of solids

For instance, chemical shift anisotropy has an interaction strength on the order of  $10^3$  Hz and would require a spinning speed of at least that order to effectively average.

Furthermore, homonuclear dipolar interactions of nuclei with large gyromagnetic ratios such as  $^1\text{H}$  can require spinning speeds in the tens of kHz regime. Quadrupolar couplings have a very broad range of interaction strengths but some of the stronger ones approach MHz values which are to date technically impossible to physically average through rapid spinning.

Nevertheless, the use of small ceramic rotors and precise engineering enables rotational speeds of over 100 kHz, often sufficient for a wide range of samples. These are achieved by suspending the ceramic rotor on a gas cushion termed the bearing gas while simultaneously rotating the assembly. This is done through the application of drive gas onto a grooved plastic cap which both seals the rotor and serves as a surface upon which to effect rotation. The end result of these experiments is often a substantial improvement in spectral resolution (Figure 2.6)

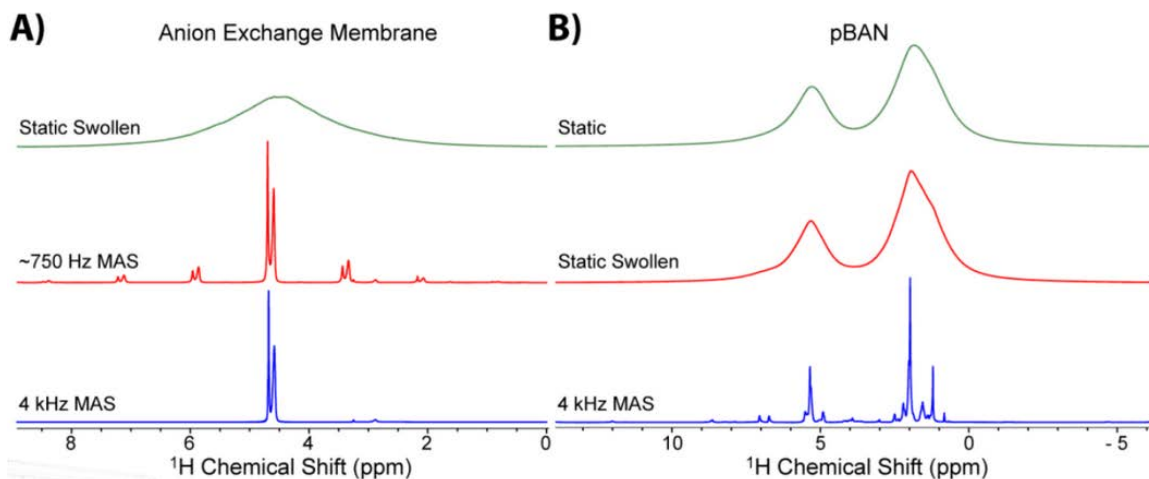


**Figure 2.6.** Example of resolution enhancement as demonstrated by using high resolution magic angle spinning (HR–MAS) NMR for A) methanol swollen anion exchange membrane, and B)  $\text{CDCl}_3$  swollen pBAN (polyButadiene-AcryloNitrile) polymer. (Todd M. Alam and Janelle E. Jenkins (2012). HR-MAS NMR Spectroscopy in Material Science, *Advanced Aspects of Spectroscopy*, Dr. Muhammad Akhyar Farrukh (Ed.), InTech, DOI: 10.5772/48340. Available from: <http://www.intechopen.com/books/advanced-aspects-of-spectroscopy/hr-mas-nmr-spectroscopy-in-material-science>)

It is however worth considering the constraints fast spinning has on experimental design. For one, high spinning speeds are made possible through a reduction in the rotor size. However, for less sensitive nuclei this can be problematic as longer acquisition times would be required to achieve acceptable spectra. Furthermore, viscous liquids can also benefit from relatively slow rotation (e.g. several kHz). Although, their characterization requires spherical inserts to ensure centripetal force does not place pressure on and remove the cap during rotation. Such an event could result in rapid deceleration in what is colloquially termed a “rotor crash”, likely causing significant

damage to the assembly.

With respect to the experiments discussed in Chapter 6, spin stability is an important consideration. As the chapter describes progress towards in-situ NMR measurements of a lithium ion battery under MAS conditions, the experimental design implemented can significantly impact spin performance. For instance the incorporation of highly conducting metals can produce eddy currents which halt rotation completely. As well, the geometry of the in-situ cell can incorporate balancing issues which increase instability and limit the maximum achievable rotational speed.

Ultimately, for purposes of the discussion here, a complete description of more complex MAS-NMR and the insightful experiments therein is unnecessary. The more detailed MAS-NMR experiments described were performed on the  $^{29}\text{Si}$  nucleus in a favourable configuration. Specifically,  $^{29}\text{Si}$  is a spin  $\frac{1}{2}$  nucleus which mitigates quadrupolar interactions. It exists at 5% natural abundance which, while decreasing overall sensitivity, mitigates homonuclear dipolar coupling significantly. A list of specific nuclear properties for all nuclei used in both solid and solution state experiments is presented in Table 2.2 below. Additional details on the MAS experiments performed are presented in Chapters 5 and 6.

Nucleus	Spin	NMR Frequency @ 7.046 T (MHz)	Percent Natural Abundance	Sensitivity Rel. to $^1\text{H}$
$^1\text{H}$	$\frac{1}{2}$	300.000	99.98%	1
$^7\text{Li}$	$\frac{3}{2}$	116.590	92.58%	0.27
$^{19}\text{F}$	$\frac{1}{2}$	282.231	100%	0.83
$^{29}\text{Si}$	$\frac{1}{2}$	59.595	4.70%	3.69E-4

**Table 2.2.** Nuclear properties for relevant nuclei investigated in this thesis

### 2.1.5 - In-Situ NMR of Lithium Ion Battery Electrodes

Solid state NMR can provide a wealth of information on the chemical changes a battery undergoes over its operational lifespan. Most NMR experiments of battery materials are conducted ex-situ via the disassembly of a cycled battery at a specific point of charge and preparation of the active material for analysis.<sup>36</sup> This procedure has the advantage of allowing for the application of detailed NMR pulse sequences under MAS without the myriad of complications associated with characterization during operation. However, ex-situ characterization is much slower and precludes state of charge resolution possible during in-situ experiments. Also, disassembly provides an opportunity for changes in the active material to occur during handling and eliminates the possibility of observing metastable charge states that are only visible under an applied electric potential. For these reasons and others, in-situ NMR experiments are deemed worthwhile, despite the significant technical difficulties which accompany them.

In large part, in-situ NMR of lithium ion batteries is enable because of the highly favourable properties of the  $^7\text{Li}$  nucleus. Under sufficiently fast magic angle spinning  $^7\text{Li}$

spectra typically result in relatively narrow lineshapes across a small chemical shift range. This is despite the presence of a weak quadrupole moment whose contribution is generally only noticed when comparing it to  $^6\text{Li}$  which has an even smaller quadrupole moment. While the small chemical shift range can be problematic in differentiating chemical environments, the 92.58% natural abundance and large gyromagnetic ratio contribute to it having a particularly high NMR sensitivity. However,  $^7\text{Li}$  in-situ experiments typically require a static experimental configuration where chemical shift anisotropy contributes greatly to the line broadening. Fortunately, this is mitigated by the often spherical electronic environment surrounding  $^7\text{Li}$  nuclei. Additionally, the high inherent NMR sensitivity allows even the broadened signal to be detected with relative ease. When coupled with the chemical nature of lithium ion batteries, where paramagnetism and electronic effects of conducting materials can greatly expand the chemical shift range, static  $^7\text{Li}$  NMR becomes substantially more viable.

This potential has been recognized over the past two decades. A range of different in-situ NMR experiments have been designed to measure the change in chemical environment of LIB cathodes and anodes. While the absolute number of studies has been limited due to the difficulty in performing the experiments, there has nevertheless been success acquiring significant insights into LIB operation. For instance, one of the first in-situ NMR studies was conducted on the lithiation of hard-carbon anode materials by Rouzaud et. al.<sup>37</sup> The study suggested that initial lithiation involves intercalation in-between graphite sheets but that the majority of the reversible capacity is ultimately quasi-metallic lithium located in the bulk carbon. Subsequent in-situ studies have

considered other materials including a seminal paper by Grey et. al.<sup>38</sup> In it are shown silicon metal anodes where the formation of a metastable crystalline lithium silicide phase towards the end of lithiation is observed. This phase however was too unstable to be seen in a more typical ex-situ NMR analysis. The field continues to see additional contributions including a 2016 study which monitored  $^7\text{Li}$ ,  $^{23}\text{Na}$ , and  $^{31}\text{P}$  resonances during in-situ NMR of  $\text{LiFePO}_4$  and  $\text{NaFePO}_4$ .<sup>39</sup> The work included the introduction of an automatic tune/match circuit to increase the S/N ratio, a problem which has commonly plagued in-situ experiments.

From an experimental perspective there are few options with regard to the methodological specifics of an in-situ NMR experiment, though generally there are two primary variations. The first involves a vertical geometry where two cylindrical conducting plates are coated with electrode materials and compressed about a polypropylene separator. The pressure from the plates helps to ensure adequate cyclability while the vertical orientation makes such cells ideally suited to in-situ  $^7\text{Li}$  imaging experiments. However, the restricted surface area and required use of a saddle coil both have a detrimental effect on the S/N ratio.

For those experiments requiring increased time resolution or utilizing difficult to characterize materials, the vertical plate geometry becomes especially problematic. Towards this end a horizontal geometry is typically employed. These cells are often encased in a plastic, sealable bag inside of which the battery components are assembled and isolated from the outside environment. Copper and aluminum mesh current collectors are employed to allow RF penetration and the flat geometry enables the use of greater

sample quantities. The entire assembly is then surrounded by a solenoid coil which possesses enhanced sensitivity in comparison to the saddle coil used in vertical geometries.<sup>40</sup>

The primary disadvantage for the flat plate, horizontal configuration is the use of metallic components. The skin depth effect of the metallic current collectors typically used prevents RF penetration to the active material components. While this effect can be mitigated by using mesh current collectors it nevertheless significantly reduces the practical S/N ratio obtainable. Another side effect for the use of metallic current collectors is the necessity for a flat design as the skin depth effects previously mentioned would prevent the excitation of nuclei towards the center of the battery assembly. This significantly reduces the total amount of accessible sample which is even more deleterious as it is a static setup without the linewidth narrowing effect of magic angle spinning. Other problems of note include electronic noise introduction, magnetic field inhomogeneity, variable tune and match conditions, and ease of cell construction. To both circumvent and mitigate these issues the concept of using non-metallic current collectors is thus discussed. While the result specific information is contained in subsequent thesis chapters, this section is meant to highlight the procedural aspects of their use and how they might improve in-situ NMR characterization of lithium ion batteries.

Cellulose itself is a non-conducting porous medium with significant mechanical strength, porosity, chemical resistivity, and represents a biodegradable and renewable resource. In an unmodified state cellulose serves as an electrical insulator, but its porous and hydrophilic surface properties allow the use of aqueous binders to coat its surface in

electrically conductive carbon or appropriate active material slurry. One of the more obvious advantages for cellulosic substrates is the significantly increased RF penetration. This not only increases signal intensity directly but enables an alternative cell design. Specifically, the presence of electrochemically accessible electrode material on the outer surface enables a cylindrical as opposed to more commonly used flat geometry. This retains the use of a solenoid coil but increases the total surface area by a factor proportional to the outer diameter of the cylinder. Furthermore, the nature of the substrate supports substantially greater amounts of active material per unit area.

The combination of factors thus described can be effective in improving the overall sensitivity and time resolution of associated in-situ NMR measurements. However, questions may arise concerning the validity of using cellulosic substrates in place of a metallic current collector. Fortunately, short term cycling data helps to ensure their applicability in this regard. Also, the concept of using a non-metallic current collector is not strictly limited to the use of cellulose. Other porous, yet sufficiently conductive support materials could also serve this purpose. An expanded discussion on these considerations is presented in Chapter 5.

## **2.2 - References**

- (1) Pimentel, G. C. Infrared Spectroscopy: A Chemist's Tool. *J. Chem. Educ.* **1960**, 37 (12), 651.

- (2) Meusinger, R.; Chippendale, A. M.; Fairhurst, S. A. Nuclear Magnetic Resonance and Electron Spin Resonance Spectroscopy. In *Ullmann's Encyclopedia of Industrial Chemistry*; Wiley-VCH Verlag GmbH & Co. KGaA, 2000.
- (3) Levitt, M. H. *Spin Dynamics: Basics of Nuclear Magnetic Resonance*; John Wiley & Sons, 2013.
- (4) Kitayama, T.; Hatada, K. *NMR Spectroscopy of Polymers*; Springer Science & Business Media, 2013.
- (5) Cowan, B. *Nuclear Magnetic Resonance and Relaxation*; Cambridge University Press, 2005.
- (6) Gerothanassis, I. P.; Kalodimos, C. G. NMR Shielding and the Periodic Table. *J. Chem. Educ.* **1996**, 73 (8), 801.
- (7) Cavanagh, J.; Fairbrother, W. J.; III, A. G. P.; Skelton, N. J. *Protein NMR Spectroscopy: Principles and Practice*; Academic Press, 1995.
- (8) Yannoni, C. S.; Kendrick, R. D. NMR Nutation Spectroscopy: A Method for Determining Molecular Geometry in Amorphous Solids. *J. Chem. Phys.* **1981**, 74 (1), 747–749.
- (9) Dutta Majumdar, R.; Gerken, M.; Mikula, R.; Hazendonk, P. Validation of the Yen–Mullins Model of Athabasca Oil-Sands Asphaltenes Using Solution-State <sup>1</sup>H NMR Relaxation and 2D HSQC Spectroscopy. *Energy Fuels* **2013**, 27 (11), 6528–6537.

- (10) Braun, S.; Kalinowski, H.-O.; Berger, S. *150 and More Basic NMR Experiments: A Practical Course*; Wiley, 1998.
- (11) Popov, M. *Modern Nmr Techniques and Their Application in Chemistry*; CRC Press, 1990.
- (12) Claridge, T. D. W. *High-Resolution NMR Techniques in Organic Chemistry*; Newnes, 2009.
- (13) Li, Z.; Pauric, A. D.; Goward, G. R.; Fuller, T. J.; Ziegelbauer, J. M.; Balogh, M. P.; Halalay, I. C. Manganese Sequestration and Improved High-Temperature Cycling of Li-Ion Batteries by Polymeric Aza-15-Crown-5. *J. Power Sources* **2014**, *272*, 1134–1141.
- (14) Jang, D. H.; Shin, Y. J.; Oh, S. M. Dissolution of Spinel Oxides and Capacity Losses in 4 V Li / Li X Mn<sub>2</sub> O<sub>4</sub> Cells. *J. Electrochem. Soc.* **1996**, *143* (7), 2204–2211.
- (15) Stejskal, E. O.; Tanner, J. E. Spin Diffusion Measurements: Spin Echoes in the Presence of a Time-Dependent Field Gradient. *J. Chem. Phys.* **1965**, *42* (1), 288–292.
- (16) Altieri, A. S.; Hinton, D. P.; Byrd, R. A. Association of Biomolecular Systems via Pulsed Field Gradient NMR Self-Diffusion Measurements. *J. Am. Chem. Soc.* **1995**, *117* (28), 7566–7567.
- (17) Holz, M.; Heil, S. R.; Sacco, A. Temperature-Dependent Self-Diffusion Coefficients of Water and Six Selected Molecular Liquids for Calibration in Accurate <sup>1</sup>H NMR PFG Measurements. *Phys. Chem. Chem. Phys.* **2000**, *2* (20), 4740–4742.

- (18) Brooks, B. R.; Brooks, C. L.; Mackerell, A. D.; Nilsson, L.; Petrella, R. J.; Roux, B.; Won, Y.; Archontis, G.; Bartels, C.; Boresch, S.; et al. CHARMM: The Biomolecular Simulation Program. *J. Comput. Chem.* **2009**, *30* (10), 1545–1614.
- (19) Martínez, L.; Andrade, R.; Birgin, E. G.; Martínez, J. M. PACKMOL: A Package for Building Initial Configurations for Molecular Dynamics Simulations. *J. Comput. Chem.* **2009**, *30* (13), 2157–2164.
- (20) Jones, J. E. On the Determination of Molecular Fields. II. From the Equation of State of a Gas. *Proc. R. Soc. Lond. Math. Phys. Eng. Sci.* **1924**, *106* (738), 463–477.
- (21) Shi, Y.; Xia, Z.; Zhang, J.; Best, R.; Wu, C.; Ponder, J. W.; Ren, P. Polarizable Atomic Multipole-Based AMOEBA Force Field for Proteins. *J. Chem. Theory Comput.* **2013**, *9* (9), 4046–4063.
- (22) Metz, S.; Kästner, J.; Sokol, A. A.; Keal, T. W.; Sherwood, P. ChemShell—a Modular Software Package for QM/MM Simulations. *Wiley Interdiscip. Rev. Comput. Mol. Sci.* **2014**, *4* (2), 101–110.
- (23) Karplus, M.; Kuriyan, J. Molecular Dynamics and Protein Function. *Proc. Natl. Acad. Sci. U. S. A.* **2005**, *102* (19), 6679–6685.
- (24) Ishiyama, T.; Morita, A. Molecular Dynamics Study of Gas–Liquid Aqueous Sodium Halide Interfaces. I. Flexible and Polarizable Molecular Modeling and Interfacial Properties. *J. Phys. Chem. C* **2007**, *111* (2), 721–737.

- (25) Jorgensen, W. L.; Maxwell, D. S.; Tirado-Rives, J. Development and Testing of the OPLS All-Atom Force Field on Conformational Energetics and Properties of Organic Liquids. *J. Am. Chem. Soc.* **1996**, *118* (45), 11225–11236.
- (26) Damm, W.; Frontera, A.; Tirado-Rives, J.; Jorgensen, W. L. OPLS All-Atom Force Field for Carbohydrates. *J. Comput. Chem.* **1997**, *18* (16), 1955–1970.
- (27) Price, M. L. P.; Ostrovsky, D.; Jorgensen, W. L. Gas-Phase and Liquid-State Properties of Esters, Nitriles, and Nitro Compounds with the OPLS-AA Force Field. *J. Comput. Chem.* **2001**, *22* (13), 1340–1352.
- (28) Sambasivarao, S. V.; Acevedo, O. Development of OPLS-AA Force Field Parameters for 68 Unique Ionic Liquids. *J. Chem. Theory Comput.* **2009**, *5* (4), 1038–1050.
- (29) Ganesh, P.; Jiang, D.; Kent, P. R. C. Accurate Static and Dynamic Properties of Liquid Electrolytes for Li-Ion Batteries from Ab Initio Molecular Dynamics. *J. Phys. Chem. B* **2011**, *115* (12), 3085–3090.
- (30) Acevedo, O.; Jorgensen, W. L. Exploring Solvent Effects upon the Menshutkin Reaction Using a Polarizable Force Field. *J. Phys. Chem. B* **2010**, *114* (25), 8425–8430.
- (31) Borodin, O. Polarizable Force Field Development and Molecular Dynamics Simulations of Ionic Liquids. *J. Phys. Chem. B* **2009**, *113* (33), 11463–11478.

- (32) Abbott, A. P.; Boothby, D.; Capper, G.; Davies, D. L.; Rasheed, R. K. Deep Eutectic Solvents Formed between Choline Chloride and Carboxylic Acids: Versatile Alternatives to Ionic Liquids. *J. Am. Chem. Soc.* **2004**, *126* (29), 9142–9147.
- (33) Schröder, C. Comparing Reduced Partial Charge Models with Polarizable Simulations of Ionic Liquids. *Phys. Chem. Chem. Phys.* **2012**, *14* (9), 3089–3102.
- (34) Duer, M. J. *Solid State NMR Spectroscopy: Principles and Applications*; John Wiley & Sons, 2008.
- (35) Polenova, T.; Gupta, R.; Goldbourn, A. Magic Angle Spinning NMR Spectroscopy: A Versatile Technique for Structural and Dynamic Analysis of Solid-Phase Systems. *Anal. Chem.* **2015**, *87* (11), 5458–5469.
- (36) Grey, C. P.; Dupré, N. NMR Studies of Cathode Materials for Lithium-Ion Rechargeable Batteries. *Chem. Rev.* **2004**, *104* (10), 4493–4512.
- (37) Letellier, M.; Chevallier, F.; Clinard, C.; Frackowiak, E.; Rouzaud, J.-N.; Béguin, F.; Morcrette, M.; Tarascon, J.-M. The First in Situ  $^7\text{Li}$  Nuclear Magnetic Resonance Study of Lithium Insertion in Hard-Carbon Anode Materials for Li-Ion Batteries. *J. Chem. Phys.* **2003**, *118* (13), 6038–6045.
- (38) Key, B.; Bhattacharyya, R.; Morcrette, M.; Seznéc, V.; Tarascon, J.-M.; Grey, C. P. Real-Time NMR Investigations of Structural Changes in Silicon Electrodes for Lithium-Ion Batteries. *J. Am. Chem. Soc.* **2009**, *131* (26), 9239–9249.

- (39) Pecher, O.; Bayley, P. M.; Liu, H.; Liu, Z.; Trease, N. M.; Grey, C. P. Automatic Tuning Matching Cyclers (ATMC) in Situ NMR Spectroscopy as a Novel Approach for Real-Time Investigations of Li- and Na-Ion Batteries. *J. Magn. Reson.* **2016**, (265), 200–209.
- (40) Hoult, D. I.; Richards, R. E. The Signal-to-Noise Ratio of the Nuclear Magnetic Resonance Experiment. *J. Magn. Reson.* 1969 **1976**, 24 (1), 71–85.



### **Chapter 3 - Combined NMR and Molecular Dynamics Modeling Study of Transport Properties in Sulfonamide Based Deep Eutectic Lithium Electrolytes in LiTFSI Based Binary Systems**

The chapter described here was concerned with transport property measurements via NMR of deep eutectic electrolyte mixtures in addition to their application in a molecular dynamics context. Such measurements showed distinct trends in transport number and diffusion coefficient as a function of temperature and composition. Additionally, they confirmed the concrete influence of hydrogen bonding on transport properties. Molecular dynamics simulations further influenced the interpretations, ultimately allowing for a detailed discussion of the implications of solution state structure on the observed dynamics.

This work was published in the Journal of Physical Chemistry Chemical Physics (PCCP) where the authors include Allen D. Pauric, Ion C. Halalay, and Gillian R. Goward. Data collection, initial analyses, and initial draft manuscript preparation were conducted by Allen D. Pauric. Final analyses and manuscript edits included contributions from all authors.

#### **3.1 - Introduction**

The electrochemical and transport properties of  $\text{LiPF}_6$  and organic carbonate-based electrolytes have enabled the proliferation of lithium ion batteries (LIBs) in applications ranging from portable consumer electronics to electrified vehicles. However, their thermal abuse tolerance behaviour is less than optimal, at least in some practical

applications (portable consumer electronics and computers). In addition, while their electrochemical window is sufficient for present day electrode chemistries, the trend toward the use of positive electrode materials with higher operation voltages (in excess of 4.3 and preferably 5.0 V vs.  $\text{L/Li}^+$ ) requires electrolyte solutions with greater electrochemical stability. In order to address these concerns, alternative electrolytes have been proposed and investigated over the past ten to fifteen years.

One of the most prominent classes of alternative electrolytes are ionic liquids (ILs)<sup>1</sup>. An ionic liquid is a molten salt (thus comprised solely of a cations and anions mixture) with a close-to-ambient (<40 °C) melting temperature. The keen interest in ILs stems from a number of properties advantageous for various battery applications. Pertinent to the context of LIBs are exceptionally low vapour pressures (often in the nano-Torr range), leading to negligible flammability<sup>2</sup>, and very wide electrochemical stability windows<sup>3</sup>. Unfortunately, these very desirable properties are often accompanied by a very high viscosity and low mobility of the  $\text{Li}^+$  cation, which is a potential showstopper for automotive LIB applications. Even more challenging, however, is the temperature dependence of the transport properties of ILs. The introduction of a lithium salt into an ionic liquid often results in a very low transference number, typically less than 0.2 as a consequence of  $\text{Li}^+$  not being the sole cation present in the electrolyte solution. Furthermore, the migration and accumulation of positive ions other than  $\text{Li}^+$  cations near the electrode surfaces produces a concentration gradient which opposes the direction of  $\text{Li}^+$  migration and diffusion,<sup>4</sup> thus leading to a serious impairment of the rate performance of most LIBs containing IL-based electrolyte solutions.

Deep eutectic electrolytes (DEEs), sometimes also called deep eutectic solvents (or DESs<sup>5</sup>) have been investigated as alternative electrolytes which may avoid the issue of the low lithium transference number that plagues LIB electrolytes with an IL as a major component. The primary difference between DEEs and ILs is that, whereas ILs are composed solely of cations and anions, DEEs are mixtures of a charge-delocalized organic salt with a small polar organic molecule. Such an arrangement disrupts the ionic bonding of the salt and also weakens any strong molecular interactions (e.g., hydrogen bonding) present in the polar organic solvent. Note that in their pure states, all components of a DEE are solids. Upon homogenization in appropriate proportions, a DEE will display a melting point depression which can be more than 100 °C below the lowest melting point of either pure component. A prominent and well-studied example of a binary DEE is composed of urea and choline chloride<sup>6-8</sup>. Note that, while DEEs display transport and electrochemical properties similar to those of other concentrated electrolyte solutions based on solutions of lithium salts in low vapor pressure solvents such as propylene carbonate, dimethyl sulfoxide, sulfones, or glymes<sup>9</sup>, the essential distinction of DEEs is that both the solvents and salts entering their composition are solids at above-ambient temperatures, in their pure states.

Many of the properties inherent in ILs are also present in DEEs, including an extremely low vapor pressure (hence minimal flammability) and a wide electrochemical stability window (reaching 5.5 V vs. Li/Li<sup>+</sup> in some cases). The distinct advantage of DEEs over ILs for LIB applications is the presence of a single cation, namely Li<sup>+</sup>. ILs typically require a relatively high concentration of dissolved lithium salt in order to be

useful for LIBs. This leads to the presence of at least three separate ionic species, a common anion and two different cations. The presence of the additional cation causes a significant reduction of the  $\text{Li}^+$  transference number in ILs; values lower than 0.15 are not uncommon. The importance of the  $\text{Li}^+$  transference number is often overlooked in the literature on ILs. Note that a specific conductivity increased at the expense of a considerably reduced  $\text{Li}^+$  transference number to values in the 0.05 to 0.15 range<sup>10</sup> is of no relevance for LIBs used in automotive applications; which, e.g., generally require charge/discharge rates of at least C/3. In commonly used liquid organic electrolyte solutions, transference numbers do not exhibit much variation, having mostly values in the 0.25 to 0.45 range<sup>11</sup>. However, DEEs can display significantly higher transport numbers (reaching 0.7 for some discussed here) and may therefore demonstrate acceptable cycling performance in full cells even at specific conductivity values lower than those typical for LIB industry state-of-the-art  $\text{LiPF}_6$  in organic carbonates electrolyte solutions. (Note: While transference numbers and transport numbers do not have the same physical meaning, they typically agree within a few (2 to 5) percent and so their “mixed comparison” is legitimate for the purpose of an approximate comparison, as is the case for the present discussion. See the Appendix for further justification why transport numbers can act as surrogates for transference numbers in the present case, for a limited number of DEEs of interest, i.e., those with the highest specific conductivity values from the present study.) In addition to the advantage of increased transference numbers, even when compared with liquid electrolytes, DEEs are less expensive to produce than ILs, due to the considerably greater ease in the manufacture of simple organic molecules.

They do, however, suffer from some of the drawbacks of ionic liquids. These include a high viscosity and a specific conductivity significantly lower than liquid organic electrolyte solutions, particularly at low temperatures. Of particular interest for LIBs are DEEs comprised of a mixture of an organic lithium salt such as lithium bis(trifluoromethanesulfonyl)imide (LiTFSI) and a solvent consisting of small, polar, organic molecules<sup>12-15</sup>.

Note that most DEEs contain organic molecules with the propensity for hydrogen bonding. This has traditionally been considered detrimental to LIBs performance, although recent work suggests otherwise<sup>16</sup>. Hydrogen bonds in the organic solvent component are important for deep eutectics formation because they can be broken through the introduction of an organic salt. In this context, it should be noted that hydrogen bonds can be represented by a strong permanent dipole. Any molecular organic solid with molecules that participate in strong dipolar interactions should, in principle, be suitable for use in a DEE. When considering a solution state system, the term “Coulombic interaction”<sup>17</sup> refers to the electrostatic forces between two ions. For both polar and non-polar molecules, the sum of their interactions are described by their van der Waals interactions<sup>18</sup>. The strongest of these are interactions between permanent dipoles, followed by those between induced dipoles and permanent dipoles, and finally by the interaction between two instantaneous (induced) dipoles. A practically useful deep eutectic would minimize the sum of all these forces to the greatest extent possible. This would result in the least resistance to diffusion and thus very likely translate into an increased  $\text{Li}^+$  conductivity.

While the number of DEE studies reported in the literature is increasing<sup>19</sup>, there exists a need for research addressing fundamental properties, including solution state structure and transport properties, to guide the search for DEEs with improved properties for various applications, including Li-ion batteries. To this end, the present study is concerned with LiTFSI-based binary deep eutectic electrolytes based on lithium fluorinated imide salts and a sulfonamide organic component. A specific emphasis is placed on experimental measurements of the individual diffusion coefficients for the anion, cation, and organic components through pulsed field gradient nuclear magnetic resonance (PFG-NMR)<sup>20</sup>. These data are complemented by molecular dynamics simulations over a range of component ratios. The MD models were validated against the measured diffusion coefficients and the simulation results were further interpreted, to yield insights into structural justifications for the observed behavior.

### **3.2 - Experimental**

Methanesulfonamide (MSA, melting point 85 °C) and dimethylmethanesulfonamide (DMMSA, melting point 49 °C) (Figure 3.1) were purchased from Sigma Aldrich (>97%) and dried under vacuum before handling in an argon-filled glove box. Electrochemical grade lithium bis(trifluoromethanesulfonyl)imide (LiTFSI, melting point 235 °C) was also obtained from Sigma Aldrich (99.95%). <sup>1</sup>H NMR of the resultant deep eutectic electrolyte mixtures did not reveal any water within the NMR detection limit of ~1000 ppm.

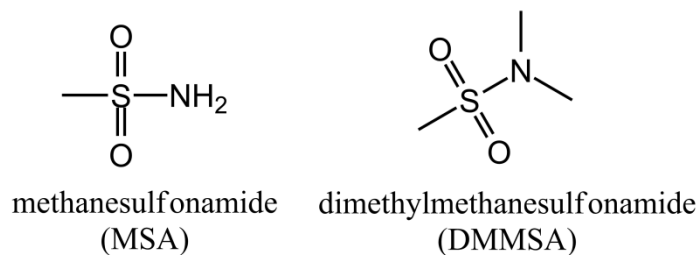


**Figure 3.1.** Structural formulae of the organic components considered in this work, methanesulfonamide (MSA) and dimethylmethanesulfonamide (DMMSA)

The diffusion coefficients of the  $\text{Li}^+$  cation, TFSI<sup>-</sup> anion, and neutral component (MSA or DMMSA) were studied independently, by monitoring the motion of the  $^7\text{Li}$ ,  $^{19}\text{F}$ , and  $^1\text{H}$  nuclei, respectively, by pulsed field gradient NMR (a.k.a. PFG NMR). The diffusion measurements were conducted as a function of temperature with a Bruker AV300HD instrument equipped with a Diff50 diffusion probe. Given a maximum gradient strength of  $\sim 2,700$  G/cm, it was possible to measure diffusion coefficients as small as  $10^{-14}$   $\text{m}^2/\text{s}$ . Samples were prepared, loaded, and sealed into 5 mm NMR tubes inside of a glove box and subsequently measured over the 25 - 80 °C temperature range, to determine the  $^7\text{Li}$  (116.642 MHz) and  $^{19}\text{F}$  (282.404 MHz) diffusion coefficients. All  $^1\text{H}$  (300.130 MHz) spectra were collected at temperatures lower than 60 °C, due to physical limitations related to the coil materials. A pulsed field gradient pulse sequence with the inclusion of longitudinal eddy current delays was utilized as previously described by Byrd et al.<sup>21</sup>. This sequence was considered most suitable for this work since it only contains two gradient pulses and two spoiler gradients. This was beneficial, as the relatively short relaxation time  $T_2^*$  ( $\approx 5$  ms) observed in the present case can sometimes

significantly reduce the S/N ratio if long and/or numerous gradient pulses are used. In addition, the pulse sequence still incorporates eddy current delays which are necessary for samples with a high salt concentration, as in the present case.

Pulses were calibrated to 90° with 9  $\mu$ s pulses at 40 W, with 4096 points in the time domain, 1 s duration relaxation delay, and 50 ms eddy current delay. Each measurement was temperature-calibrated using an external NMR shift reference. Prior to measurements,  $\approx$ 20 minutes of temperature equilibration were applied via the use of an appropriate number of dummy scans. Measurements consisted of 8 to 64 scans per gradient increment over a total of 32 increments. The specific number of scans was adjusted in order to achieve a similar S/N ratio for the mixture at all temperatures. The absolute value of the maximum gradient strength was also varied as a function of temperature, in order to enable a measuring range of 5 to 95% for total signal attenuation. This was necessary for achieving optimal sensitivity to the changes in the observed diffusion coefficient. Both gradient pulses were kept at a 2 ms duration, whereas the two spoiler gradients were limited to 1 ms using a diffusion delay which varied from 10 to 50 ms as needed for achieving full resolution of the decay curve. Data processing was performed through the Bruker Topspin 3.2 software using the  $T_1/T_2$  relaxation module. In particular, this involved fitting the attenuation in peak area for the signal of interest. The decay was then fit to an exponential function using known values of the gradient pulse strength, duration, as well as diffusion delay. The resultant fit provided diffusion coefficient values for the nucleus being monitored at a given temperature.

### 3.3 - Molecular Dynamics Simulations

Initial molecular dynamics simulation parameters involved a total of 500 molecules placed in random spatial positions and orientations using the Packmol software<sup>22</sup>. Simultaneously, an initial set of molecular topologies from the OPLS-AA force field were developed using the MKTOP automatic routine<sup>23</sup>. These topologies were then further modified using parameters from the modified OPLSA-AA force field of Lopes et al.<sup>24</sup>. All partial charges were scaled by a factor necessary to reproduce NMR measured diffusion coefficients, typically 85% of their initially calculated values (0.85c). It is important to note however that, while charge scaling performs reasonably well in reproducing the experimentally observed dynamics, there may exist concerns regarding the validity of the overall structure.<sup>25</sup> A comparison between the computed density and experimental data served as an independent check of the validity of the charge scaling procedure in our study and yielded a discrepancy of ~5%, which should alleviate such concerns. Nevertheless, the effects of charge scaling combined with finite-size effects<sup>26</sup> must always be carefully considered when evaluating results from MD simulations. The MD simulations were performed with the GROMACS 4.62 software package.<sup>27</sup> All simulations were conducted with periodic boundary conditions, with each initial simulation including an energy minimization step through a steepest descent method. This was followed by several isobaric-isothermal (NPT) ensemble simulated annealing steps from the desired temperature (e.g., 298 K) to 600 K over a period of 4 ns, followed by a 2 ns equilibration time at the desired temperature. This was performed in order to reach an equilibrium starting configuration at each desired temperature. The higher

temperatures helped in overcoming the slow dynamics of the system and reduced the amount of time required for equilibration. Final runs were conducted in a canonical (NVT) ensemble at the desired temperature over a duration of 30 ns, with 1 ps time steps. Analysis of the simulations was performed through use of select radial distribution functions visualized through the VMD software program.

### **3.4 - Results and Discussion**

Initial performance characterization of deep binary eutectic electrolytes of LiTFSI with MSA and DMMSA was conducted by Halalay et. al., who measured their density and transport properties (dynamic viscosity and specific conductivity) as functions of temperature and composition.<sup>28</sup> The room temperature ionic conductivity of DMMSA/LiTFSI eutectic mixtures of ~1 mS/cm, while not high enough for use in commercial Li-ion batteries, provides sufficient justification for a more detailed investigation, which is the subject of the present work. The previously measured DEE properties served as parameters for validating the molecular dynamics simulations.

#### **3.4.1 - PFG-NMR Results**

Figure 3.2 displays Arrhenius plots for the temperature dependence of the cation, anion, and neutral component diffusion coefficients at three DMMSA:LiTFSI compositions. An identical analysis performed for MSA:LiTFSI mixtures at the same solvent-to-salt mole ratios is shown in Figure 3.3.

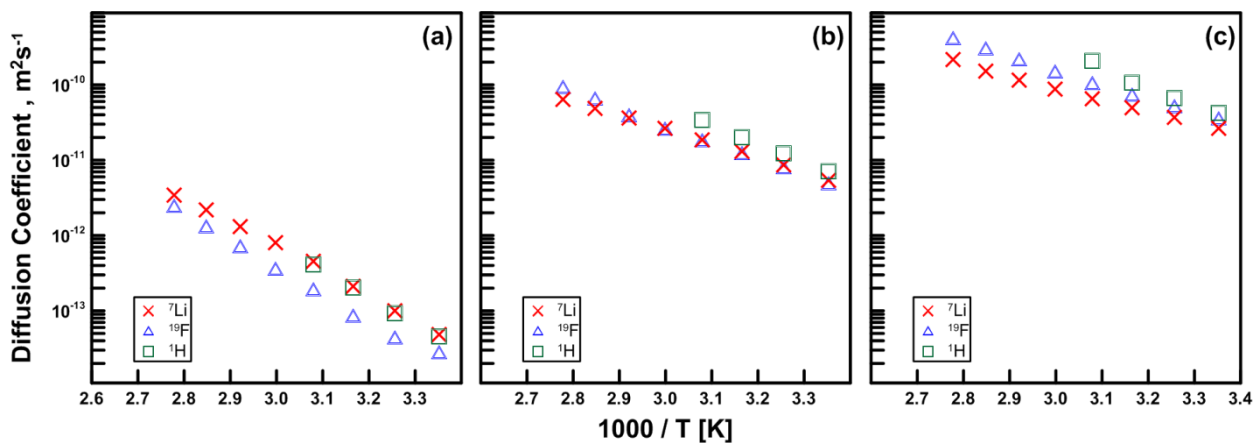


**Figure 3.2.** Temperature dependence of the  $^1\text{H}$ ,  $^7\text{Li}$ , and  $^{19}\text{F}$  diffusion coefficients in DMMSA:LiTFSI mixtures at (a) 1:1, (b) 3:1, and (c) 6:1 molar ratios, determined by PFG-NMR.

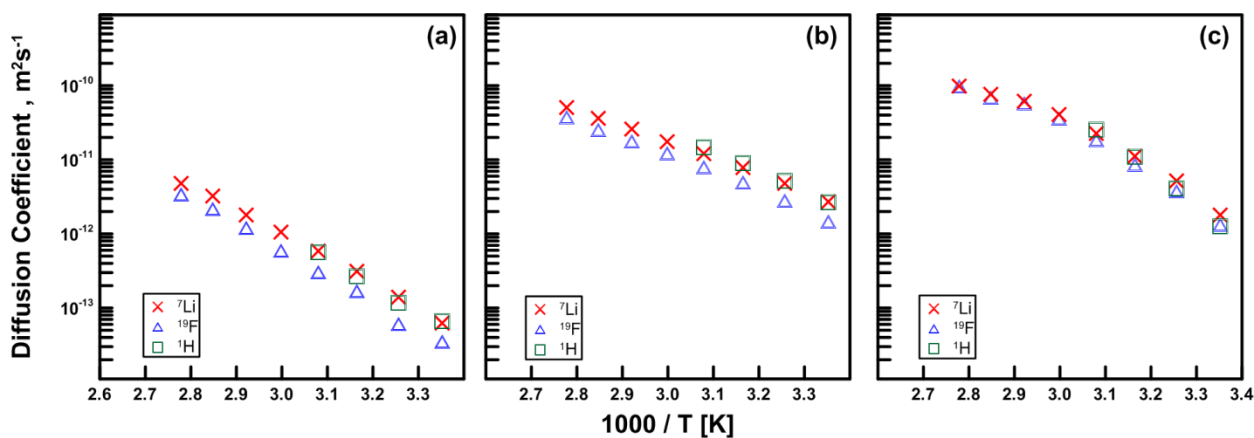


**Figure 3.3.** Temperature dependence of the  $^1\text{H}$ ,  $^7\text{Li}$ , and  $^{19}\text{F}$  diffusion coefficients at 1:1 (a), 3:1 (b) and 6:1 (c) MSA:LiTFSI molar ratios, determined through PFG-NMR.

All diffusion coefficients increase monotonically with temperature over the temperature interval investigated in the present study. A monotonic increase in diffusion coefficients with DMMSA content is evident at all temperatures (Fig. 3.2.). In contrast, for MSA-based DEEs all diffusion coefficients increase at high temperatures and exhibit

a non-monotonic behaviour at the lowest two temperatures when the solvent-to-salt mole ratio changes from 1:1 to 3:1 to 6:1 (Fig. 3.3.).

At 298 K the  $^7\text{Li}$  diffusion coefficients are  $4.8 \times 10^{-14}$ ,  $5.4 \times 10^{-12}$ , and  $2.6 \times 10^{-11} \text{ m}^2/\text{s}$  respectively for 1:1, 3:1, and 6:1 DMMSA:LiTFSI mole ratios. Note that these  $\text{Li}^+$  diffusion coefficients are lower by an order of magnitude than values typical for organic solvent:LiTFSI electrolytes.<sup>29</sup> The  $^{19}\text{F}$  diffusion coefficients are smaller than those for  $^7\text{Li}$ , but their relative differences decrease as the temperature increases toward 353 K. A similar trend was observed for the  $^1\text{H}$  diffusion coefficients. These results correlate well with the decrease in lattice energy associated with the weakening of both Coulombic interactions in LiTFSI and the van der Waals forces between DMMSA molecules. The general trend indicates that an increase in the proportion of the solvent significantly increases the diffusion coefficients of all species. However, there exists a preferential increase in the mobility of both TFSI anions and DMMSA molecules relative to  $\text{Li}^+$  cations. (Note also that increasing the DMMSA:LiTFSI ratio beyond 6:1 results in the development of regions where recrystallization of DMMSA can be readily observed by visual inspection.)

The  $^7\text{Li}$  diffusion coefficients for MSA-based DEEs are lower than the corresponding DMMSA-based mixtures, especially at near-ambient temperatures. At 298 K, the  $^7\text{Li}$  diffusion coefficients are  $6.2 \times 10^{-14}$ ,  $2.7 \times 10^{-12}$  and  $1.8 \times 10^{-12} \text{ m}^2/\text{s}$  for 1:1, 3:1, and 6:1 MSA:LiTFSI ratios, respectively. In contrast to DMMSA, the 6:1 MSA:LiTFSI composition exhibits a reduced diffusion coefficient at room temperature relative to the 3:1 composition. The high temperature behaviour is more akin to that observed for the

DMMSA-based DEEs. The  $^{19}\text{F}$  diffusion coefficients become approximately half of those observed for  $^7\text{Li}$  at the 1:1 and 3:1 compositions, and exhibit a moderate relative increase at the 6:1 composition. These trends were observed at all investigated temperatures. At 298 K,  $^1\text{H}$  diffusion coefficients have values very similar to those for  $^7\text{Li}$  for the 1:1 and 3:1 compositions, with a modest decrease observed at the 6:1 mole ratio. At elevated temperatures, the decrease in  $^1\text{H}$  diffusion coefficient relative to that of  $^7\text{Li}$  becomes less pronounced.

For MSA-based DEEs the trends differ somewhat from those for the DMMSA-based DEEs at near-ambient temperatures and with increasing solvent-to-salt ratio. Specifically, comparison of the diffusion coefficients at 298K for the 3:1 and 6:1 MSA:LiTFSI molar ratios shows values which are lower at 6:1 than at 3:1. However, as the temperature increases, the diffusion coefficients quickly achieve and then surpass the values measured at the 3:1 composition. A possible explanation of the observed differences in behaviour may result from the substitution of one dialkylamine in DMMSA by one amine functional group in MSA. This configuration gives MSA an increased hydrogen bonding capacity, which is the likely cause for the observed change in behaviour. The hydrogen bonding capacity can directly influence the diffusion of MSA molecules and TFSI anions, since both can form hydrogen bonds which hinder diffusion. However, this dynamical limitation is overcome at higher temperatures, because of the directional nature and relatively the low strength of the hydrogen bonds. Ultimately this yields the deviation from linearity, i.e., deviation from Arrhenius behaviour, of the diffusion coefficient as a function of temperature at 6:1 MSA:LiTFSI as compared to the 3:1 composition.

It is useful to examine how the diffusivity and conductivity of the DEEs considered here compare with electrolyte solutions based on organic solvents or ionic liquids with LiTFSI as the lithium salt. This is particularly important, given the roles that the relative values of diffusivity and transport properties play in determining the overall LIB performance. From a comparison of the Hayamizu et al. results determining the diffusion coefficients of fourteen LiTFSI solutions in organic solvents [29], it is immediately apparent that  $^7\text{Li}$  diffusivities in organic liquids are more than an order of magnitude higher than those for the DEEs examined in the present work. However, the respective ionic conductivities vary considerably less, by factors ranging from 3 to 8 [28]. The observed differences stem from a variety of factors, including the relative ease of dissociating LiTFSI, and that the DEEs contain larger concentrations of Li salt compared with LiTFSI solutions in aprotic organic solvents. Therefore, the handicap of a considerably slower  $\text{Li}^+$  dynamics in the deep eutectic electrolytes compared with liquid electrolyte solutions is made up to some extent by the increased lithium salt concentration in the former.

In contrast to organic solvents, ILs display similarly low diffusivities as do DEEs, although this is due to the high electrostatic (a.k.a. Coulombic) interaction energies. While modifications to the anion or cation geometry are often performed in order to weaken Coulombic interactions, they nevertheless remain the limiting factor. (For comparison, note that the diffusion coefficient of lithium in the ternary [emim<sup>+</sup>][TFSI][Li<sup>+</sup>] ionic liquid is approximately  $10^{-11} \text{ m}^2/\text{s}$  at 298 K.<sup>30</sup> Also note that, while the specific conductivity of this IL is several times higher than that the values reported for the

DEEs from the present work, a significant fraction of this conductivity is not due to  $\text{Li}^+$  cations, as indicated by its extremely low  $\text{Li}^+$  transport number ( $\approx 0.02$ ). (While transference numbers and transport numbers do not have – in the strictest sense – identical meanings, since they are ratios of physical quantities with different dimensions,<sup>31</sup> they differ by less than 5% in most cases of interest. They can therefore be used interchangeably to some extent, especially when encountering large differences between these ratios during materials comparisons, as in the present case.) A low  $\text{Li}^+$  transport number leads to the development of detrimental concentration gradients, particularly at high current densities. In contrast, the transport numbers for the DEEs investigated in the present work is (shown as a function of temperature in Figure 3.4.) have considerably larger values, ranging from 0.40 to 0.70 for DMMSA:LiTFSI and from 0.55 to 0.70 for MSA:LiTFSI at temperatures of interest for the LIBs operation. Immediately apparent are the high lithium transport numbers at the 1:1 compositions, with values near 0.7 at room temperature, which are significantly higher than the 0.25 to 0.4 values typical for organic carbonate based electrolytes.<sup>32</sup> Decreasing trends in the lithium transport number were obtained both as a function of temperature and solvent-to-salt mole ratio. It is noteworthy that for the MSA-based DEEs the transport numbers exceed 0.5 even for the dilute solution, and for DMMSA-based DEEs transport numbers similar to those of state-of-the-art liquid electrolyte solutions are obtained for the dilute (6:1 mole ratio) solution. Thus the transport numbers for these DEEs are at least 25x greater than those for the  $[\text{EMIM}^+][\text{TFSI}^-][\text{Li}^+]$  ionic liquids. Therefore, despite a lower ionic conductivity, they may enable LIB performance, provided they exhibit

electrochemical stability windows which accommodate electrode materials typical for LIBs and also have favourable film-forming properties.

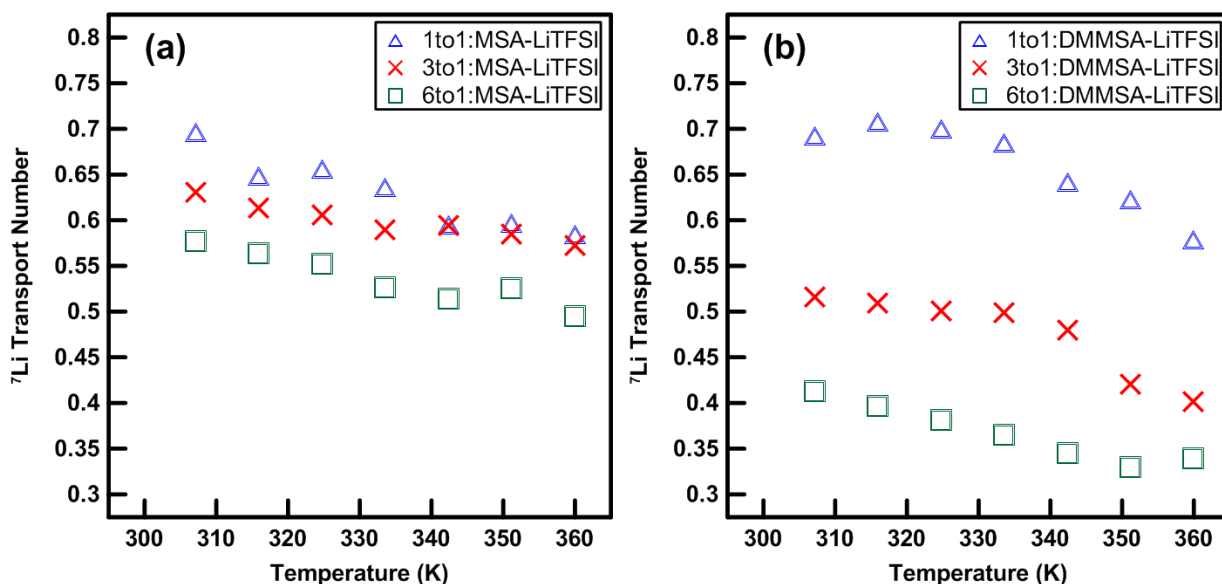


**Figure 3.4.** Variation of the lithium transport numbers with temperature derived from  ${}^1\text{H}$ ,  ${}^7\text{Li}$ , and  ${}^{19}\text{F}$  diffusion coefficient measurements for 1:1, 3:1 and 6:1 mole ratios of MSA:LiTFSI (a) and DMMSA:LiTFSI (b).

One rationalization of the observed transport number behaviour comes from a consideration of the lithium coordination environment. The high positive charge density of the  $\text{Li}^+$  cations tends to center the coordination environment on it. Therefore one must consider three kinds of diffusion: independent movement of  $\text{Li}^+$  cations from one coordination environment to another, concerted diffusion of  $\text{Li}^+$  together with its coordination environment, and independent movement of the coordination environment components. If all components diffuse as at the same rate, transport numbers of 0.5 will result for both cations and anions. Deviations from 0.5 can only result from the faster

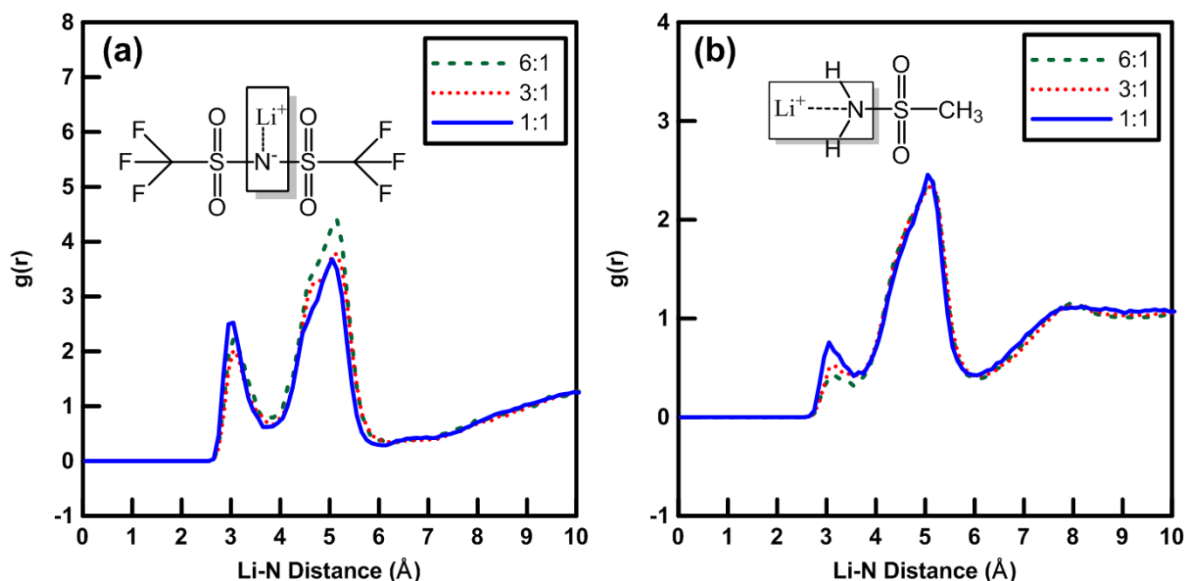
diffusion of one species relative to the others. When the viscosity is high, the energy barrier to independent movement for a large molecule such as TFSI<sup>-</sup> is greater than that for unsolvated Li<sup>+</sup>. The limiting case for this situation would be a solid lithium conductor where only Li<sup>+</sup> is diffusing relative to a stationary anionic matrix. As the viscosity decreases, the energy barrier for independent TFSI<sup>-</sup> diffusion may become equal to or even smaller than that for the Li<sup>+</sup> cation. Such behaviour must originate from a change in the relative magnitude of the intermolecular forces which limit the diffusion of ions. Further support for this argument is provided by Figure 3.4, which displays a decrease in the lithium transport number of DMMSA based DEEs relative to MSA based ones at the two more dilute compositions. The capacity for hydrogen bonding of MSA increases the magnitude of the van der Waals (vdW) interactions, i.e., the dipole-dipole forces. These contribute to the slowing of TFSI<sup>-</sup> diffusion to a greater extent than Li<sup>+</sup> diffusion, as the anion is disproportionately affected by van der Waals forces. Unfortunately, the introduction of hydrogen bonding also leads to a slowing of overall diffusion. Nevertheless, its incorporation may increase the lithium transport number by slowing the diffusion of anions.

Furthermore, evaluation of the transport properties with respect to ionicity was conducted. However, the limited access to temperature dependent conductivity data has relegated the data to Figure 7.3.1.1 in section 7.3.1 of the appendix. The trend in ionicity mirrors that observed in the lithium transport numbers. However, their overall magnitude appears anomalously low and as such there is still some question about their reliability.

### 3.4.2 - Molecular Dynamics Simulation Results

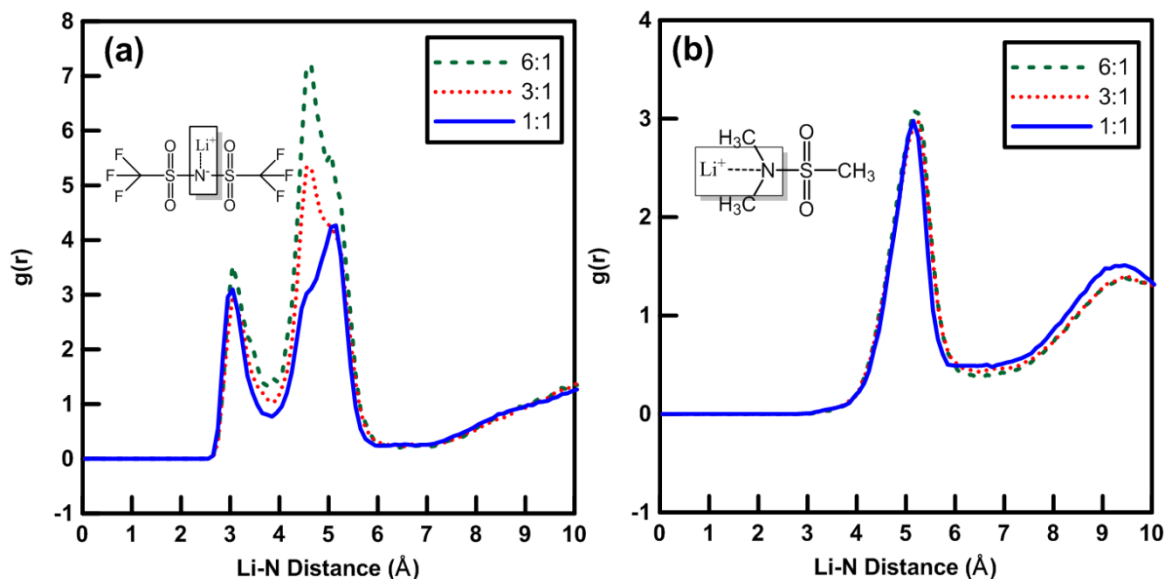
Molecular dynamics (MD) simulations were conducted to obtain further insights into the solution state structure of the deep eutectic electrolytes and thus aid the interpretation of the diffusion data obtained by NMR. The primary method we used for interpreting the results of MD simulations is based on the radial distribution function (RDF)<sup>33</sup>, a powerful tool for characterizing the time dependent atomic environment surrounding a chemical species of interest. The RDF is a particularly valuable investigation tool for systems devoid of long-range order such as liquids and glasses.

Figure 3.5 displays the RDFs of  $\text{Li}^+$  cations relative to the nitrogen atoms in TFSI (panel a) and MSA (panel b). Three peaks are visible in both cases. The smaller peak at the shortest ( $\sim 3 \text{ \AA}$ ) distance corresponds to direct lithium-nitrogen coordination. Since nitrogen is a site with negative charge density, direct coordination is possible, though relatively unlikely. However, this interaction is stronger with TFSI than with MSA. The two larger peaks at  $\sim 4.5$ , and  $5.0 \text{ \AA}$  distances are the result of the (Coulombically-driven) lithium-oxygen coordination. They specifically correspond to bidentate and monodentate coordination of TFSI to  $\text{Li}^+$ , respectively.



**Figure 3.5.** Lithium-nitrogen radial distribution functions for  $\text{Li}^+$  contact with TFSI (a) and MSA (b) at 298K in MSA:LiTFSI mixtures.

Comparison of this data with the RDFs for the DMMSA:LiTFSI system (see Figure 3.6) indicates no direct coordination of  $\text{Li}^+$  cations by nitrogen in DMMSA, but a slightly increased coordination by N in TFSI<sup>-</sup> over what is observed for MSA:LiTFSI (Fig. 3.5). The proportion between the bidentate and monodentate coordinations increases as a function of greater organic content. Though for MSA the effect is substantially smaller than for DMMSA. This is a consequence of MSA being better able to compete for lithium coordination than DMMSA. Also, the greater favourability of the TFSI<sup>-</sup> to  $\text{Li}^+$  contacts with DMMSA is further exemplified by the increasing proportion of bidentate to monodentate coordination.



**Figure 3.6.** Lithium-nitrogen radial distribution functions for intermolecular between contact between Li<sup>+</sup> and TFSI<sup>-</sup> (a) or DMMSA (b) at 298 K in DMMSA:LiTFSI mixtures.

Comparison of Figures 3.7 and 3.8 reveal some important features of the lithium coordination environment with regard to direct lithium-oxygen contacts. Foremost are the amplitudes of the RDFs at 3 Å being well above that in the RFD values for the Li<sup>+</sup> cation coordination by nitrogen at the same (nearest-neighbor) distance. This indicates a strong correlation between the presence of lithium and oxygen at this distance, suggesting that these are the strongest intermolecular interactions in the system. Referring to Figure 3.7 in particular, the small differences in the RDFs for TFSI<sup>-</sup> and MSA show that the differences in their coordination of Li<sup>+</sup> are surprisingly small. This indicates that, despite its neutral charge profile, MSA competes quite effectively for lithium coordination and is

a key factor for the deep eutectic formation, since it is the competition for the lithium cation which breaks the ionic bonds in the LiTFSI salt.

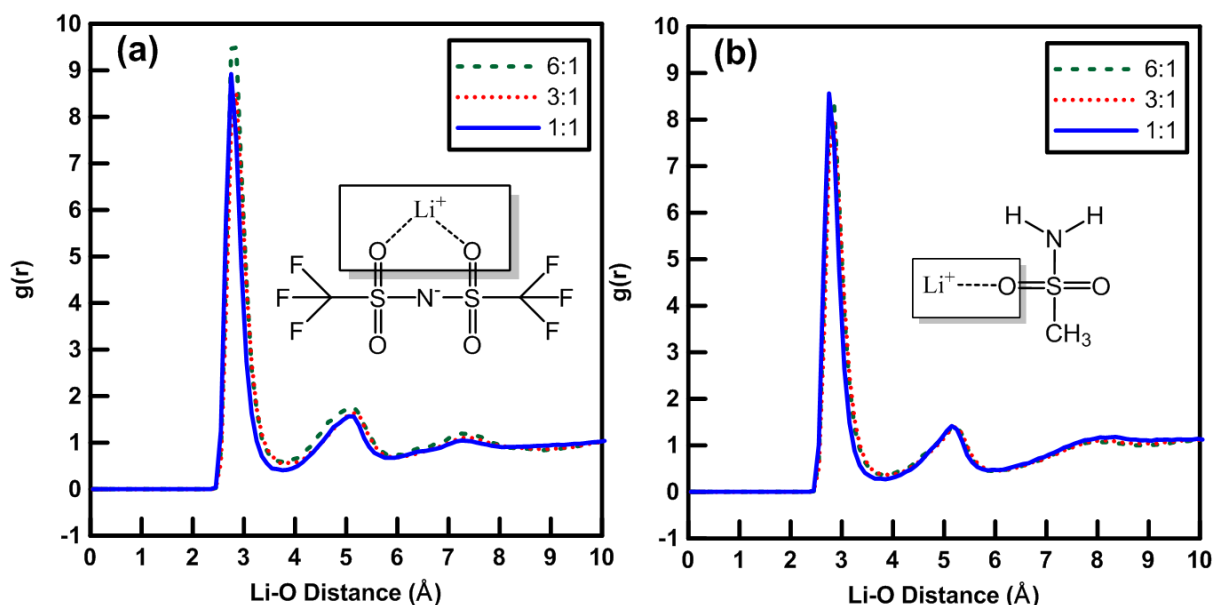


**Figure 3.7.** Lithium – oxygen radial distribution functions for intermolecular contact between  $\text{Li}^+$  and TFSI (a) or MSA (b) at 298 K for MSA:LiTFSI mixtures.

MSA-based  $\text{Li}^+$ -O contacts display no substantial changes in the RDFs with changing MSA content in the DEE. This is, however, not the case for DMMSA (Figure 3.8) where the RDF associated with the  $\text{Li}^+$  coordination by the O atoms in TFSI displays a significant increase with DMMSA content, whereas the coordination of  $\text{Li}^+$  by the O atoms in DMMSA does not change. This discrepancy can be attributed to the preferential association of  $\text{Li}^+$  with TFSI over DMMSA. Since the DMMSA molecule does not have any easily accessible sites with significant positive charge density, it cannot compete with  $\text{Li}^+$  for coordinating TFSI and hence there is an increase in the density of TFSI in the vicinity of  $\text{Li}^+$  cations. This contrasts with MSA, where the positively charged hydrogen

in the amine functional group competes successfully with  $\text{Li}^+$  for oxygen coordination. The result is increased competition for TFSI $^-$  by MSA, which competitively reduces the extent of TFSI $^-$  coordination with lithium.

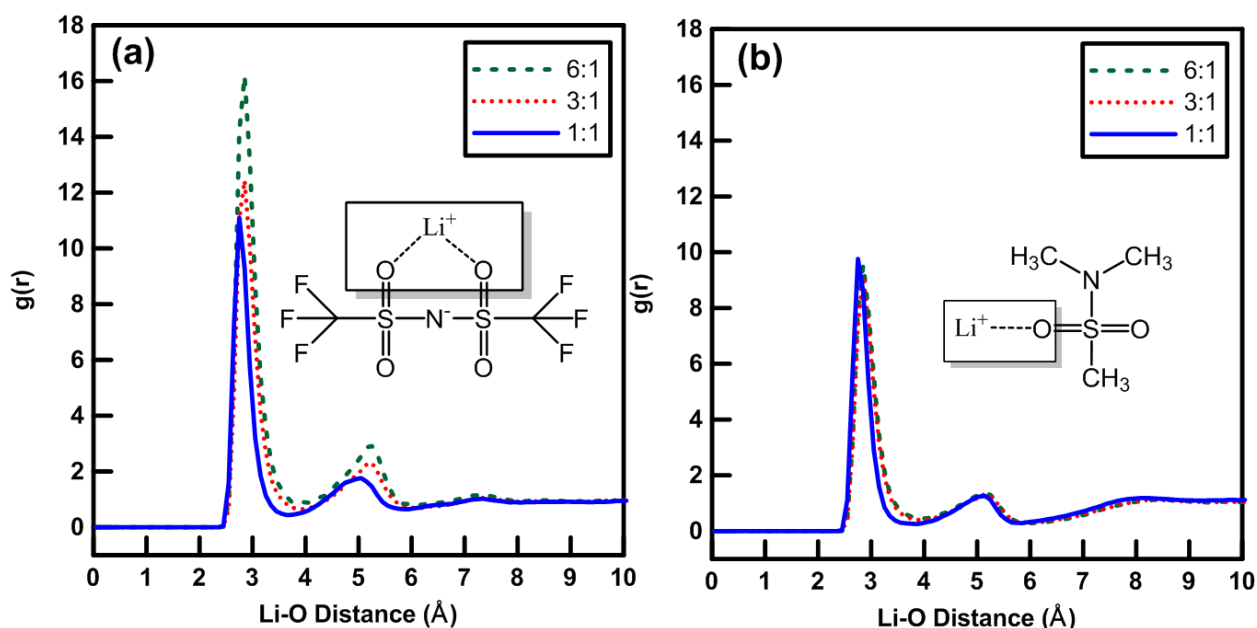


**Figure 3.8.** Lithium – oxygen radial distribution functions for intermolecular contact between  $\text{Li}^+$  cations and TFSI $^-$  (a) or DMMSA (b) in DMMSA:LiTFSI at 298 K.

Since the extent of hydrogen bonding appears to have such a significant impact on DEEs properties, we determined and then examined the RDFs for oxygen-hydrogen contacts. Figure 3.9 confirms the existence of hydrogen bonding via the intermolecular peak that appears at  $\sim 1.8$  Å. As expected, hydrogen bonding exists between MSA molecules as well as between MSA and TFSI $^-$ . Additionally, the intensity of the peak corresponding to the hydrogen bond increases with MSA content, consistent with the

increase in sites available for hydrogen bonding.

An interesting temperature dependence was observed for hydrogen bonding interactions, which is illustrated with Figures 3.9 and 3.10. The extent of hydrogen bonding was observed to diminish, as revealed by a significant decrease in intensity, well beyond that observed for any other atom pair. This observation is consistent with an increase in the diffusion coefficients with temperature shown in Figure 3.2, which can now be attributed to the weakening of the hydrogen bonding network. As a point of comparison, Figures 3.11 and 3.12 indicate the absence of the hydrogen bonding peak in DMMSA:LiTFSI mixtures, which is to be expected because DMMSA is incapable of participating in hydrogen bonding. This further confirms the trends observed in Figure 3.2 (b) and (c), where the diffusion coefficients of all species in DMMSA:LiTFSI at low temperatures are considerably higher than the values observed for the same diffusion coefficients in MSA:LiTFSI, as shown in Figure 3.2 (b) and (c).

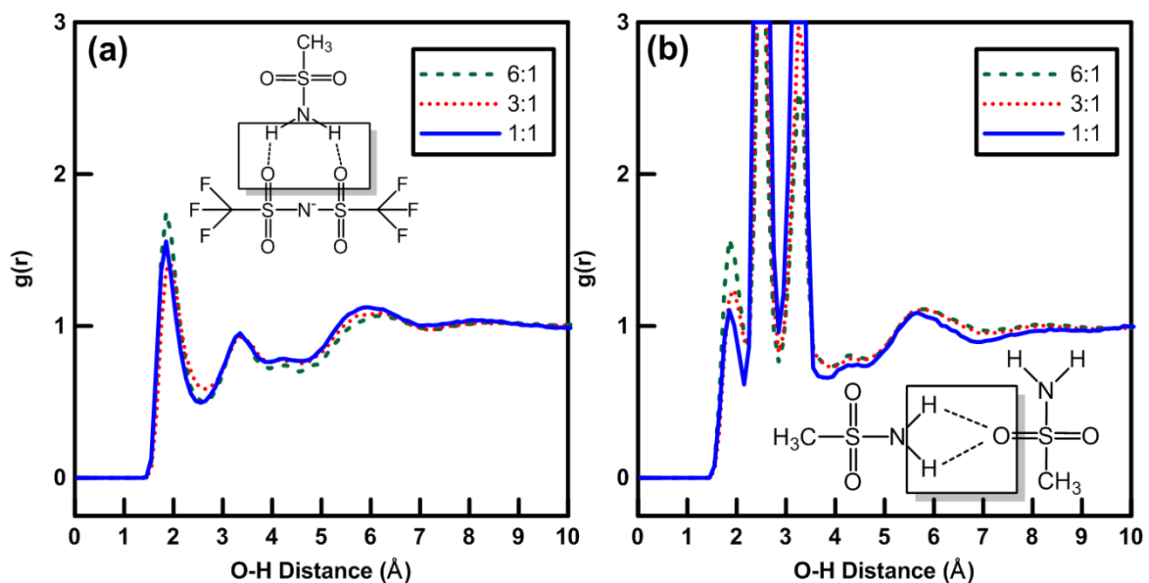


**Figure 3.9:** Oxygen – hydrogen radial distribution functions for intermolecular contact between MSA and TFSI (a) or MSA (b) in MSA:LiTFSI mixtures at 298 K.

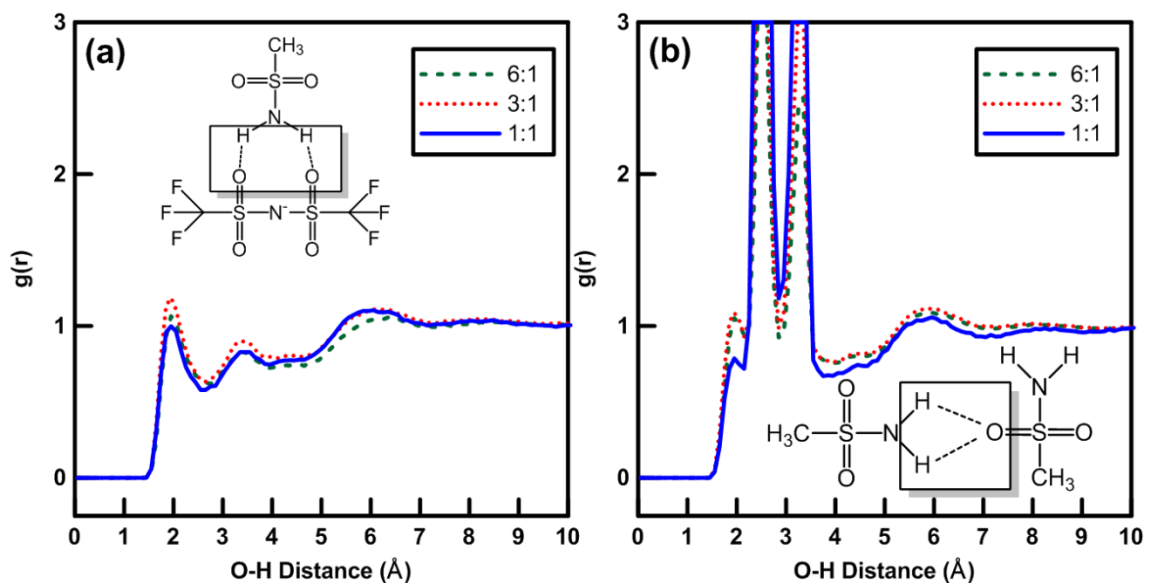


**Figure 3.10.** Oxygen – hydrogen radial distribution functions for intermolecular contact between MSA and TFSI (a) or MSA (b) in MSA:LiTFSI mixtures at 358 K.

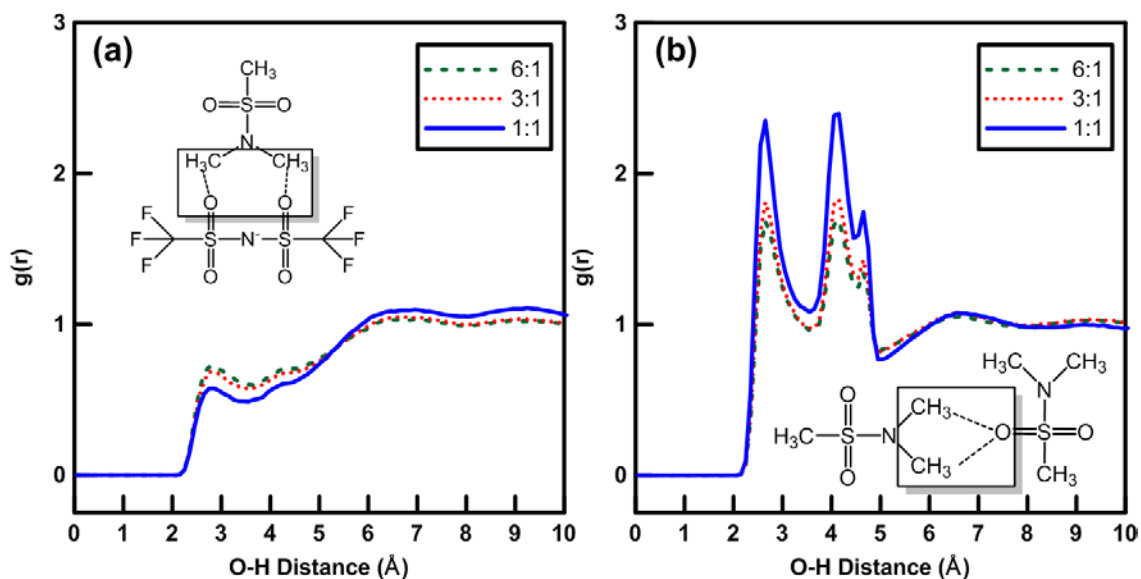


**Figure 3.11.** Oxygen – hydrogen radial distribution functions for intermolecular contact between DMMSA and TFSI (a) or DMMSA (b) in DMMSA:LiTFSI mixtures at 298 K.

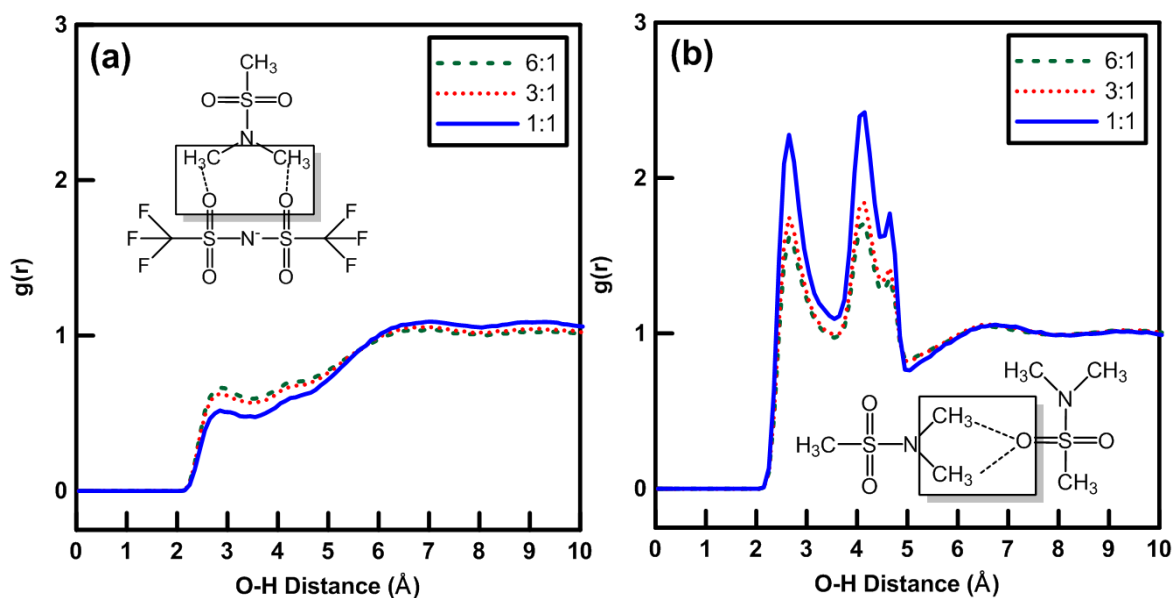


**Figure 3.12.** Oxygen – hydrogen radial distribution functions for intermolecular contacts between DMMSA and TFSI (a) or DMMSA (b) in DMMSA:LiTFSI mixtures at 358 K.

### 3.5 - Conclusions

Sulfonamide-based deep eutectic electrolytes (DEEs) were previously shown to have lithium conductivities within less than a factor of 3 from traditional  $\text{LiPF}_6$ /carbonates electrolytes. The PFG NMR measurements reported here indicate that the lithium transport number varies significantly with DEEs composition. Its magnitude was found to be at least the same as, and often significantly higher, than transport numbers of state-of-the-art ( $\text{LiPF}_6$ /mixed organic carbonates) LIB electrolytes, i.e., in the 0.40 to 0.71 range. Reasons for this behaviour were proposed using a combination of the NMR experiments and MD simulations.

The systems studied here are dominated by interactions between the  $\text{Li}^+$  cation and oxygen from both the anion and the organic component. It is this competitive feature which allows the eutectic formation. However, fine-tuning of the fluid and diffusion properties depends very significantly on van der Waals interactions. Dipole-dipole attractive interactions, while hindering overall diffusion, can nevertheless enhance the lithium transport number by slowing the translational motion of the TFSI anions more than that of the  $\text{Li}^+$  cations. In principle, any molecule with a significant amount of accessible positive charge density could influence the anion in a similar manner and therefore increase the  $\text{Li}^+$  transport (or transference) number, although at a possible decrease in overall diffusivity.

Deep eutectic electrolytes represent a relatively unexplored class of electrolytes that are promising from both cost and practical utility perspectives. While DEEs based on hydrogen bonding are the most common, as they often correspond to molecules with

large dipole moments, the latter is not a prerequisite for the formation of eutectics.

Significant room for further research into this topic is still available through an expansion of the sample space, in the search for formulations with improved properties from a practical point of view (i.e., increased specific conductivity over a broad temperature range, improved transference numbers over those typical for LiPF<sub>6</sub>/carbonates, oxidation potentials exceeding 5 V vs. Li/Li<sup>+</sup>).

### 3.6 - References

- (1) Lewandowski, A. Ionic liquids as electrolytes for Li-ion batteries - An overview of electrochemical studies. *J. Power Sources* **194** (2009) 601–609.
- (2) Zhang, S.; Sun, N.; He, X.; Lu, X.; Zhang, X. Physical properties of ionic liquids: database and evaluation. *J. Phys. and Chem. Ref. Data* **35** (2006) 1475.
- (3) Hayyan, M.; Mjalli, F. S.; Hashim, M. A.; Al Nashef, I. M.; Mei, T. X. Investigating the electrochemical windows of ionic liquids. *J. Ind. Eng. Chem.* **19** (2013) 106–112.
- (4) Krachkovskiy, S. A.; Pauric, A. D.; Halalay, I. C.; Goward, G. R. Slice-selective NMR diffusion measurements: a robust and reliable tool for in situ characterization of ion-transport properties in lithium-ion battery electrolytes. *J. Phys. Chem. Lett.* **4** (2013) 3940–3944.
- (5) Zhang, Q.; Vigier, K. D. O.; Royer, S.; Jérôme, F. Deep eutectic solvents: syntheses, properties and applications. *Chem. Soc. Rev.* **41** (2012) 7108–7146.

- (6) Abbott, A. P.; Boothby, D.; Capper, G.; Davies, D. L.; Rasheed, R. K. Deep eutectic solvents formed between choline chloride and carboxylic acids: versatile alternatives to ionic liquids. *J. Am. Chem. Soc.* **126** (2004) 9142–9147.
- (7) Sun, H.; Li, Y.; Wu, X.; Li, G. Theoretical study on the structures and properties of mixtures of urea and choline chloride. *J. Mol. Model.* **19** (2013) 2433–2441.
- (8) Pandey, A.; Rai, R.; Pal, M.; Pandey, S. How polar are choline chloride-based deep eutectic solvents? *Phys. Chem. Chem. Phys.* **16** (2013) 1559–1568.
- (9) Ueno, K.; Yoshida, K.; Tsuchiya, M.; Tachikawa, N.; Dokko, K.; Watanabe, M. Glyme–Lithium Salt Equimolar Molten Mixtures: Concentrated Solutions or Solvate Ionic Liquids? *J. Phys. Chem. B* **116** (2012) 11323–11331.
- (10) Frömling, T.; Kunze, M.; Schönhoff, M.; Sundermeyer, J.; Roling, B. Enhanced Lithium Transference Numbers in Ionic Liquid Electrolytes. *J. Phys. Chem. B* **2008**, *112* (41), 12985–12990.
- (11) Zugmann, S.; Fleischmann, M.; Amereller, M.; Gschwind, R. M.; Wiemhöfer, H. D.; Gores, H. J. Measurement of Transference Numbers for Lithium Ion Electrolytes via Four Different Methods, a Comparative Study. *Electrochimica Acta* **2011**, *56* (11), 3926–3933.
- (12) Liang, H.; Li, H.; Wang, Z.; Wu, F.; Chen, L.; Huang, X. New binary room-temperature molten salt electrolyte based on urea and LiTFSI. *J. Phys. Chem. B* **105** (2001) 9966–9969.

- (13) Hu, Y.; Li, H.; Huang, X.; Chen, L. Novel room temperature molten salt electrolyte based on LiTFSI and acetamide for lithium batteries. *Electrochemistry Communications* **6** (2004) 28–32.
- (14) Chen, R.; Wu, F.; Liang, H.; Li, L.; Xu, B. Novel binary room-temperature complex electrolytes based on LiTFSI and organic compounds with acylamino group. *J. Electrochem. Soc.* **152** (2005) A1979–A1984.
- (15) Boisset, A.; Menne, S.; Jacquemin, J.; Balducci, A.; Anouti, M. Deep eutectic solvents based on N-methylacetamide and a lithium salt as suitable electrolytes for lithium-ion batteries. *Phys. Chem. Chem. Phys.* **15** (2013) 20054–20063.
- (16) Menne, S.; Pires, J.; Anouti, M.; Balducci, A. Protic ionic liquids as electrolytes for lithium-ion batteries. *Electrochemistry Communications* **31** (2013) 39–41.
- (17) Fehrmann, R.; Riisager, A.; Haumann, M. *Supported Ionic Liquids: Fundamentals and Applications*; John Wiley & Sons, New York, 2013.
- (18) Israelachvili, J. N.; Tabor, D. The measurement of van der Waals dispersion forces in the range 1.5 to 130 Nm. *Proc. Royal Soc. London A* **331** (1972) 19–38.
- (19) Tang, B. Recent developments in deep eutectic solvents in chemical sciences. *Monatshefte Chem.* **144** (2013) 1427–1454.
- (20) Stejskal, E. O.; Tanner, J. E. Spin diffusion measurements: spin echoes in the presence of a time-dependent field gradient. *J. Chem. Phys.* **42** (1965) 288–292.

- (21) Altieri, A. S.; Hinton, D. P.; Byrd, R. A. Association of biomolecular systems via pulsed field gradient NMR self-diffusion measurements. *J. Am. Chem. Soc.* **117** (1995) 7566–7567.
- (22) Martínez, L.; Andrade, R.; Birgin, E. G.; Martínez, J. M. PACKMOL: A package for building initial configurations for molecular dynamics simulations. *J. Comput. Chem.* **30** (2009) 2157–2164.
- (23) Ribeiro, A. A. S. T.; Horta, B. A. C.; Alencastro, R. B. de. MKTOP: a program for automatic construction of molecular topologies. *J. Brazilian Chem. Soc.* **19** (2008) 1433–1435.
- (24) Canongia Lopes, J. N.; Deschamps, J.; Pádua, A. A. H. Modeling ionic liquids using a systematic all-atom force field. *J. Phys. Chem. B* **108** (2004) 2038–2047.
- (25) Schröder, C. Comparing Reduced Partial Charge Models with Polarizable Simulations of Ionic Liquids. *Phys. Chem. Chem. Phys.* **2012**, *14* (9), 3089–3102.
- (26) Baumketner, A.; Chushak, Y. Correction for Finite-Size Effects in Molecular Dynamics Simulation of Liquid Alloys. *J. Non-Cryst. Solids* **1999**, *250–252, Part 1*, 354–359.
- (27) Van Der Spoel, D.; Lindahl, E.; Hess, B.; Groenhof, G.; Mark, A. E.; Berendsen, H. J. C. GROMACS: fast, flexible, and free. *J. Comput. Chem.* **26** (2005) 1701–1718

- (28) Geiculescu, O. E.; Des Marteau, D. D.; Creager, S. E.; Haik, O.; D. Hirshberg, D.; Shilina, Y.; Zinigrad, E.; Levi, M.D.; Aurbach, D; and Halalay, I. C.; Binary deep eutectic electrolytes for rechargeable Li-ion batteries based on mixtures of sulfonamides and lithium perfluorosulfonimide salts, accepted for publication in *J. Power Sources* (2016).
- (29) Hayamizu, K.; Aihara, Y.; Arai, S.; Garcia. Pulse-Gradient Spin-Echo  $^1\text{H}$ ,  $^7\text{Li}$ , and  $^{19}\text{F}$  NMR diffusion and ionic conductivity measurements of 14 organic electrolytes containing  $\text{LiN}(\text{SO}_2\text{CF}_3)_2$ . *J. Phys. Chem. B* **103** (1999) 519–524.
- (30) Lesch, V.; Jeremias, S.; Moretti, A.; Passerini, S.; Heuer, A.; Borodin, O. A Combined theoretical and experimental study of the Influence of Different anion ratios on lithium ion dynamics in ionic liquids. *J. Phys. Chem. B* **118** (2014) 7367–7375.
- (31) Sethurajan, A.K; Krachkovskiy, S.K.; Halalay, I.C.; Goward, G.R.; Protas, B. Accurate Characterization of ion transport properties in electrochemical systems using in-situ NMR imaging and inverse modeling, accepted for publication in *J. Phys. Chem. B*. (2015)
- (32) Valøen, L. O.; Reimers, J. N. Transport properties of  $\text{LiPF}_6$ -based Li-ion battery electrolytes. *J. Electrochem. Soc.* **152** (2005) A882–A891.
- (33) Keizer, J. *Statistical Thermodynamics of Nonequilibrium Processes*; Springer Science & Business Media, 1987.



#### **Chapter 4: NMR Determination of the Relative Binding Affinity of Crown Ethers for Manganese Cations in Aprotic Non-Aqueous Lithium Electrolyte Solutions**

The chapter described here was concerned with the application of NMR in characterizing crown ethers used for manganese trapping in LIBs. Using well established principles surrounding binding constant measurements for NMR active alkali metal cations the methodology was modified and extended to the present context. Specifically, the binding constant of lithium cations to crown ethers in non-aqueous organic solvents was directly measured and interpreted under the influence of competitive inhibition by  $Mn^{2+}$  and  $Mn^{3+}$ . This indirectly allowed a determination of manganese binding affinity relative to lithium and thus indicated their suitability towards incorporations as chelating agents in the polymeric separator.

This work was published in the Journal of Physical Chemistry C where the authors include Allen D. Pauric, Susi Jin, Timothy J. Fuller, Michael P. Balogh, Ion C. Halalay, and Gillian R. Goward. Initial data collection related to the manuscript was conducted by Allen D. Pauric and Susi Jin. Final data collection, initial analyses, and initial draft manuscript preparation were conducted by Allen D. Pauric. Polymeric crown ether synthesis was conducted by Timothy J. Fuller whereas scanning electron microscopy (SEM) characterization was performed by Michael P. Balogh. Final analyses and manuscript edits included contributions from Ion C. Halalay and Gillian R. Goward.

## 4.1 - Introduction

Manganese-rich oxides have long been identified as promising lithium-ion battery (LIB) positive electrodes due to a combination of desirable properties, such as low cost, good rate performance, excellent thermal abuse tolerance, and high specific capacity.<sup>1-8</sup> However, it is also well-known that positive electrodes containing manganese are susceptible to leaching of manganese cations into LiPF<sub>6</sub>-based electrolyte solutions.<sup>9-</sup><sup>12</sup> The dissolved Mn cations then migrate through the electrolyte solution and deposit at the negative electrode, which is typically made of graphite or some other carbonaceous material. The subsequent interaction of the manganese at the negative electrode with the electrolyte solution leads to solvent and anion decomposition, as well as loss of electrochemically active lithium, with attendant gas generation and surface film growth, all of which contribute to significant capacity fading and increase in cell resistance, particularly during LIB stand (calendar aging) and operation (cycling) at high ambient temperatures. The traditional approaches for mitigating this degradation mode, consisting mainly of elemental substitutions in the active material lattice, surface coatings, and reduction of the state-of-charge swing during LIB operation, offer only partial solutions to this problem.<sup>13-16</sup> Therefore, additional and perhaps complementary mitigation methods may be necessary for further progress in this area.

Kumagai, Komaba and coworkers<sup>17,18</sup> demonstrated that there exists a concentration threshold (between 40 and 150 ppm) above which the presence of transition metal (TM) cations in the electrolyte solution will significantly impair the performance of the

graphite negative electrode. Furthermore, Tsujikawa et al.<sup>19</sup> showed that, during a 470 days stand at 55 °C at 4.05 V (i.e., at 65% battery state-of-charge), a graphite –  $\text{Li}_x\text{Mn}_2\text{O}_4$  spinel (henceforth called LMO) cell loses 41.9% of its capacity, of which only 5.7% and 18.4% represent irreversible capacity losses due to the dissolution of Mn from the LMO positive electrode and deterioration of the graphite negative electrode structure, respectively, while 17.7% is due to film growth on the negative electrode. Based on these two observations, a novel mitigation strategy was proposed: interruption of the “chemical cross-talk” between the positive and negative electrode by preventing the Mn cations dissolved at the positive electrode from reaching the negative electrode. This may be accomplished through their trapping by suitable polymer-bound chelating agents placed in the inter-electrode space (i.e., coated onto the separator or electrodes, or integrated as part of the separator matrix). Polymer-bound crown ethers appear as prime candidates for this application, due to the well-known capability of crown ethers to selectively trap various ions.<sup>20,21</sup> So far, Ziv et al.<sup>22</sup> have demonstrated that a separator functionalized by polymeric 18-crown-6 can trap Mn cations in graphite - LMO cells, with beneficial effects for capacity retention during high-temperature cycling, while Li et al.<sup>23</sup> showed that it is possible to reduce the capacity loss rate by a factor of 2 during extended cycling of graphite - LMO cells at 50 °C by means of a separator functionalized with polymeric aza-15-crown-5. These proof of concept experiments notwithstanding, crucial questions regarding the details of the cation trapping mechanisms, the access of the manganese or other TM cations to the chelating agent bound to solid polymer matrix, as well as the optimal chelating agent and its embodiment into an optimal polymeric matrix are still

outstanding and need addressing, for the successful implementation of the TM trapping concept in practical Li-ion batteries. In this context it was found that the average oxidation state of Mn cations in the electrolyte solutions from extensively cycled cells is close to +3 and not +2 as commonly accepted.<sup>23</sup> Furthermore, appreciable differences were found in the Mn cation trapping effectiveness of various polymeric crown ethers. In particular, polymeric aza-15-crown-5 promotes significantly more manganese sequestration and associated LIB capacity retention during the high temperature cycling of graphite - LMO cells<sup>23</sup> than polymeric 18-crown-6.<sup>22</sup> Since the backbones of the two chelating polymers as well as the particle morphologies are identical (spherical), the only significant differences between the two polymeric chelating agents are the sizes of the crown ether cavities, as well as the existence and absence of a permanent dipole moment, respectively in aza-15-crown-5 and 18-crown-6. A battery possesses an internal electric field, which enables the migration of ions between its electrodes. An effective cation chelating agent must be able to counteract the force exerted by this internal electric field on the trapped cation. Note that a dipole placed in an externally applied electric field has a minimum potential energy when oriented counter-parallel to the field, i.e., when the force exerted by the electric field of the dipole field onto the ion is exactly opposite to that exerted by the externally applied electric field. Therefore, in a first approximation, one would choose a chelating agent which possesses a permanent dipole moment, to counteract the force exerted onto a Mn cation by the internal electric field of the battery.

Crown ethers have been extensively studied over the past half century, including their ability to sequester metal cations.<sup>24-30</sup> It has been shown that their binding affinities for

specific metal cations can be fine-tuned significantly by changing the electronegative atoms in the ring and also by matching the size of the macrocycle cavity to that of the target cation.<sup>31</sup> The size-matching requirement can be used to choose the appropriate-size crown for the manganese species expected to exist in the electrolyte solution. It is also desirable to characterize the binding affinity of candidate crown ethers and that of crown ether-containing polymers for manganese ions in solvents and electrolyte solutions of interest for LIB applications. Last, but not least, one must also consider the ability of the crown ether to counteract the force exerted by the electric field inside a battery on the trapped ion, i.e., the size of its dipole moment.

Nuclear magnetic resonance (NMR) is a well-recognized tool for measuring binding affinities.<sup>32,33</sup> Prior work has demonstrated that there exists a measurable change in the chemical shift of alkali metal cations between their free state and that bound to crown ethers.<sup>34,35</sup> Since the cation-crown ether system exists in a state of fast exchange, the NMR signal observed is an average of both free and bound states. Thus it should be possible to extract an equilibrium constant from the change observed in chemical shift as a function of increasing alkali metal or crown ether concentration.<sup>36</sup> Of course it should be noted that bound is being used with reference to an equilibrium exchange such that a cation does not stay permanently affixed to any specific crown ether. Nevertheless, for convenience, we will continue using the term “bound” in the present context.

Unfortunately, the  $\text{Mn}^{2+}$ ,  $\text{Mn}^{3+}$  and  $\text{Mn}^{4+}$  cations which are likely to exist in the electrolyte solution of a LIB are paramagnetic and thus undergo fast relaxation, making them not directly observable by NMR. In order to overcome this shortcoming, we have

developed a methodology utilizing lithium cations, via the  $^7\text{Li}$  chemical shift, as a probe for inferring the extent to which manganese cations are coordinated by the chelating agents (crown ethers in the present case). While this is not a direct detection method for determining manganese binding, it has the advantage of enabling the simultaneous evaluation of the competition between lithium and manganese cations for the crown ether. Given the large excess of lithium cations present in battery electrolytes, as compared with the expected amounts of manganese cations dissolved into the electrolyte solution<sup>36,37</sup>, this is an important consideration when assessing the practical utility of various chelating agents for manganese trapping.

## 4.2 - Experimental

Lithium bis(trifluoromethanesulfonyl)imide ( $\text{LiTFSI}$ ),  $\text{Mn(II)}$  chloride ( $\text{MnCl}_2$ ), and  $\text{Mn(III)}$  acetate ( $\text{Mn(OAc)}_3$ ) with 99+% purity were obtained from Sigma Aldrich. Commercial 15-crown-5 and 1-aza-15-crown-5 (Figure 4.1) were obtained from Sigma-Aldrich and IBCMRT, respectively, while the polymeric crown ether was a copolymer of 90 wt% vinylbenzyl-aza-15-crown-5 and 10 wt% crosslinked divinylbenzene, synthesized in-house at GM R&D, according to a procedure described in the Supporting Information of reference 23. All experiments were conducted at 295 K via titration of crown ether into a solution with known concentration of  $\text{Li}^+$  ions, or to a combination of  $\text{Li}^+$  and  $\text{Mn}^{2+}$  or  $\text{Mn}^{3+}$  cations. For the polymeric crown ether in particular, care was taken to maintain a uniform dispersion of the solid through frequent mechanical shaking after each crown ether addition and spinning at 10 Hz during the NMR measurements.

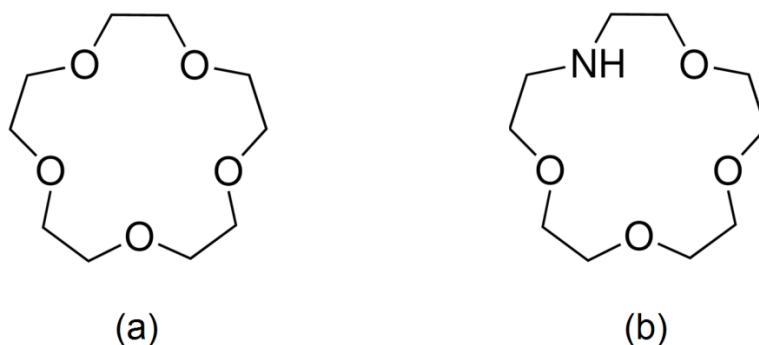


**Figure 4.1.** Chemical structures of the ion trapping agents investigated in the present work, (a) 15-crown-5 and (b) 1-aza-15-crown-5.

NMR measurements were conducted on a Bruker AV300 instrument using a BBI solution state double resonance probe.  $^7\text{Li}$  spectra (116.642 MHz) were collected with a 20 kHz hard excitation pulse ( $11\ \mu\text{s}\ 90^\circ$ ) followed by data acquisition. Relaxation delays were set to 1 s for systems without manganese, and 50 ms otherwise, in order to achieve an improved signal-to-noise ratio in the presence of fast relaxation. Initial shift referencing was performed using an aqueous 1M solution of LiCl, although subsequent binding curves were normalized to the width of the associated chemical shift window. Chemical shift values were recorded in evenly spaced intervals and fitted using the Origin 8.5SR5 non-linear equation fitting module. The equation used for fitting the data was derived from the equilibrium constants associated with lithium and manganese binding, respectively. The derivation was conducted using Maple 16 software, to achieve an expression with the initial crown ether concentration as a function of the observed chemical shift. The initial parameters for lithium-crown ether binding in the absence of manganese were chosen based on the initial concentration of lithium, while setting the manganese concentration and equilibrium constant to zero. The value for  $K_{\text{Li}}$  thus

obtained was subsequently used to fit experiments with a known initial concentration of manganese added to the solution. Despite the uncertainty in ascertaining the exact value for  $K_{Li}$  when greater than  $10^4$ , the  $K_{Li}:K_{Mn}$  ratio exhibited less uncertainty and is an effective tool for measuring trapping ability.

### 4.3 - Modeling of Cation Binding

To be effective in a LIB, manganese trapping must operate in an environment with excess lithium. This can be modeled with equilibrium constants which take two processes into account, as shown in Eq. (1):

$$(1). \quad K_{Li} = \frac{[Li \cup \otimes]}{[Li][\otimes]} \quad K_{Mn} = \frac{[Mn \cup \otimes]}{[Mn][\otimes]}$$

The terms  $[Li \cup \otimes]$  and  $[Mn \cup \otimes]$  represent the molar concentrations of the lithium and manganese cation complexes with the crown ether, respectively. Similarly,  $[Li]$ ,  $[Mn]$ , and  $[\otimes]$  are the molar concentrations of free  $Li^+$ ,  $Mn^{x+}$ , and crown ether, respectively. The two equilibria for lithium and manganese cation binding are related, since both consume the same source of crown ether, giving:

$$(2). \quad K_{Li} = \frac{[Li \cup \otimes]}{([Li_0] - [Li \cup \otimes])([\otimes_0] - [Li \cup \otimes] - [Mn \cup \otimes])}$$

$$K_{Mn} = \frac{[Mn \cup \otimes]}{([Mn_0] - [Mn \cup \otimes])([\otimes_0] - [Mn \cup \otimes] - [Li \cup \otimes])}$$

where the subscripted terms correspond to the initial concentrations of the respective species. From the  $K_{Mn}$  equation,  $[Mn \cup \otimes]$  can be isolated and subsequently substituted

into the expression for  $K_{Li}$ . This results in an expression where the only quantity not immediately known is  $[Li \cup \otimes]$ . NMR measurements of the average chemical shift of the lithium peak can be used to determine  $[Li \cup \otimes]$  via the associated change in chemical shift, (Eq. 3):

$$(3). \quad \delta_{obs} = \delta_{Li} x_{Li} + \delta_{Li \cup \otimes} x_{Li \cup \otimes}$$

For convenience, the observed chemical shift can be normalized on a scale from 0 to 1 those values being the unbound and bound states respectively (Eq. 4)

$$(4) \quad \delta_{obs,n} = \frac{(\delta_{obs} - \delta_{Li})}{(\delta_{Li \cup \otimes} - \delta_{Li})}$$

The term  $\delta_{obs,n}$  can also be expressed in terms of the two characteristic chemical shifts for the bound and unbound states along with initial and bound lithium concentrations.

$$(5). \quad \delta_{obs,n} = \frac{[Li \cup \otimes](\delta_{Li} - \delta_{Li \cup \otimes})}{[Li_0]} + \delta_{Li}$$

Further substitution and rearrangement results in an expression written solely in terms of the initial species, chemical shift values, and equilibrium constants. For the sake of brevity the full expression is not included here and is instead provided in section 7.3.2 of the appendix.

In order to illustrate the proposed method, Figure 4.2 displays the expected chemical shift behaviour for lithium binding to crown ether over a given series of increasing  $K_{Li}$  values. As the concentration of crown ether increases, there is an increase in the proportion of lithium which is in the bound state. The observed chemical shift is thus a

weighted average of these two populations. Equilibrium constants for  $> 10^3$  L/mol crown ether are indistinguishable from each other via NMR since at this limit  $[\otimes] \cong [Li \cup \otimes]$ .<sup>35</sup> The equilibrium population distribution becomes progressively more distinguishable as binding becomes less favourable.

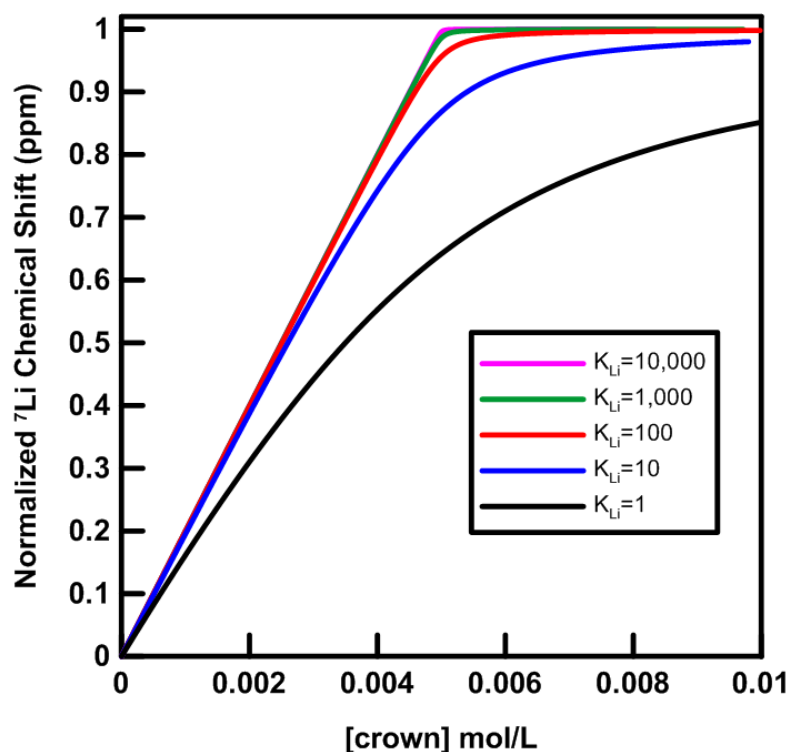


**Figure 4.2.** Theoretical binding curves for  $Li^+$  binding to crown ether with a total  $[Li^+]$  of 0.005 mol/L for  $K_{Li}^+$  values ranging from 1 to 10,000 L/mol.

The expected response changes significantly when adding a competing cation such as manganese,  $Mn^{x+}$ . Figure 4.3 demonstrates this when  $K_{Li}$  is kept constant but the  $K_{Li}:K_{Mn}$  ratio is varied over six orders of magnitude. When  $K_{Li} \gg K_{Mn}$  lithium cations are preferentially bound and a more rapid change in chemical shift with chelating agent concentration is observed. No further chemical shift occurs once the population is

completely bound; i.e., the available sites are filled. In the opposite case, when  $K_{\text{Li}} \ll K_{\text{Mn}}$ , manganese cations are preferentially complexed. The lithium cations remain in their unbound state and no chemical shift change is observed. Once all the manganese ions are bound, the remaining lithium is then complexed and an associated chemical shift change is observed. Even if the absolute values of  $K_{\text{Li}}$  and  $K_{\text{Mn}}$  are large, the ratio between them can still yield useful information, especially with respect to choosing the crown ether which is most suited for manganese sequestration.

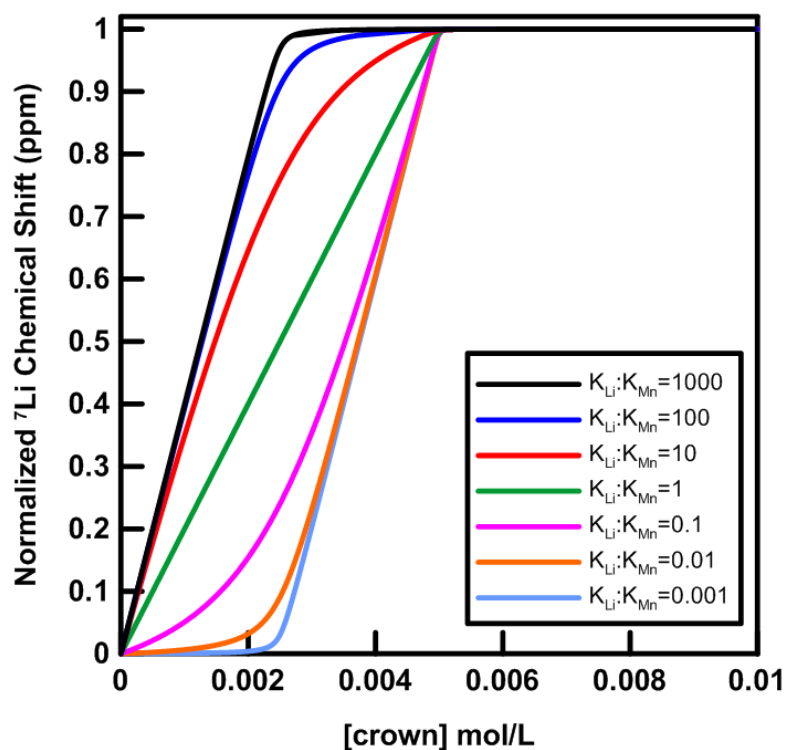


**Figure 4.3.** Theoretical binding curves for  $\text{Li}^+$  binding to crown ether in the presence of manganese cations. Total metal concentration is at  $5 \times 10^{-3}$  mol/L consisting of  $2.5 \times 10^{-3}$  mol/L of lithium and  $2.5 \times 10^{-3}$  mol/L of manganese over a range of equilibrium constant ratios. The equilibrium constant for lithium was kept constant at 1000 L/mol.

#### 4.4 - Results and Discussion

Figure 4.4 shows the binding curves associated with lithium cations complexed by 15-crown-5 and aza-15-crown-5 ethers. While both have significant similarities in their structure, one would nevertheless expect that they exhibit differing behaviour due to their significantly different dipole moments caused by the substitution of an ether oxygen by a nitrogen atom. In both cases the equilibrium constant is higher than  $1 \times 10^4$  L/mol. This, however, does not mean that their binding affinities are equivalent, but merely that they exhibit very strong binding in both cases and that any relative difference cannot be ascertained reliably. A strong binding affinity between  $\text{Li}^+$  and crown ethers has already been noted to increase lithium ion mobility in carbonate solvents.<sup>39-42</sup> Adding crown ethers to ionic liquids or other highly concentrated lithium salt electrolytes may greatly improve the otherwise poor lithium conductivity. However, in the context of manganese trapping, a high affinity for lithium cations represents a significant drawback.

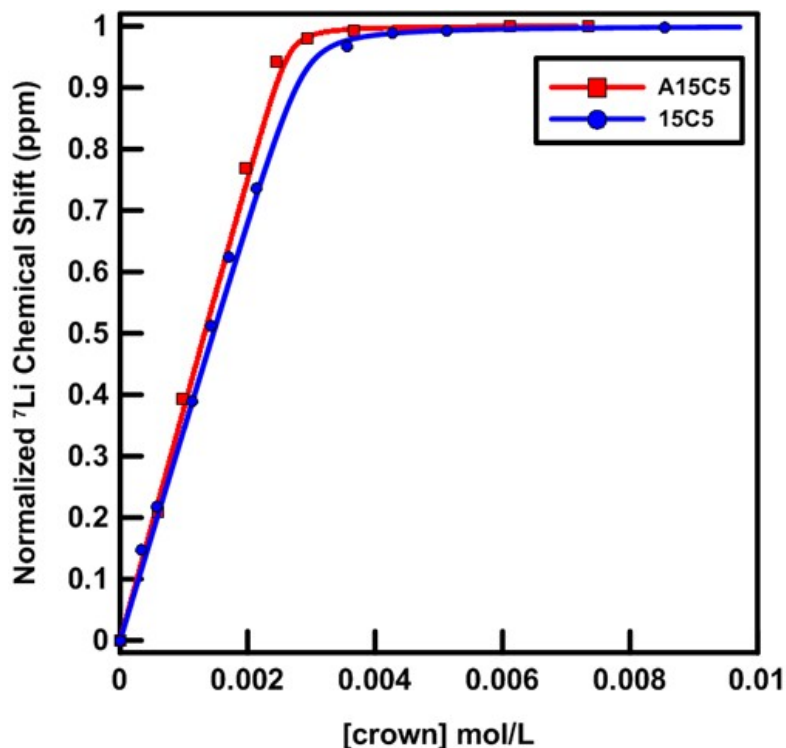


**Figure 4.4** Experimental binding curves for  $\text{Li}^+$  binding to 1-aza-15-crown-5 (A15C5) and 15-crown-5 (15C5) in propylene carbonate solvent at a constant  $\text{Li}^+$  concentration of ~3 mM.

Binding curves for diamagnetic alkali metals such as lithium are relatively straightforward to acquire and interpret.<sup>34,36,43,44</sup> However, the presence of paramagnetic cations such as manganese increases the complexity of the interpretation. The addition of manganese to a solution of lithium salt in an aprotic nonaqueous solvent such as propylene carbonate broadens the lithium resonance and causes a positive change in the chemical shift. This behaviour is in line with expectations, as the paramagnetism associated with manganese decreases relaxation rates, and is also responsible for the chemical shift change.

The addition of a crown ether to an equimolar solution of lithium and manganese cations is more nuanced, as illustrated in Figure 4.5, which displays the  $^7\text{Li}$  chemical shift behavior in propylene carbonate upon systematic additions of 15-crown-5 in the presence of equal amounts of  $\text{MnCl}_2$  and LiTFSI salts (1 mM each). In the absence of manganese one would expect a consistent trend towards more negative chemical shifts. Instead, as manganese binds more strongly to 15-crown-5 than lithium, the chemical shift remains mostly constant until all manganese is coordinated. Upon further additions of 15-crown-5 the lithium resumes the trend towards more negative chemical shift until it is also fully saturated. Looking more closely, however, one can notice a slight positive chemical shift and a broadening in excess of that already caused by manganese in solution without crown ether. One possible reason for the somewhat surprising chemical shift behaviour could be changes to the bulk magnetic susceptibility upon addition of the crown ether. However, this explanation is unlikely, since the change was only observed when  $[\otimes_0] \leq [\text{Li}_0] + [\text{Mn}_0]$  and also since the  $^1\text{H}$  chemical shift of the solvent remained unchanged despite increasing crown concentration.

Alternatively, the initial positive chemical shift trend and associated line broadening could be explained by a pseudo-contact shift resulting from electron-nuclear interactions of the paramagnetic manganese center with lithium.<sup>45,46</sup> This interaction could be facilitated by competition for the crown ether, which brings the ions in close enough proximity to produce the chemical shift change and line broadening.

While this explanation is plausible at least until all the manganese is fully coordinated, it does not explain the continued broadening and then narrowing depicted in the top

portion of Figure 4.5. Preliminary variable temperature experiments suggest that this may be a consequence of chemical exchange, with the details of this behaviour to be discussed in a future manuscript.

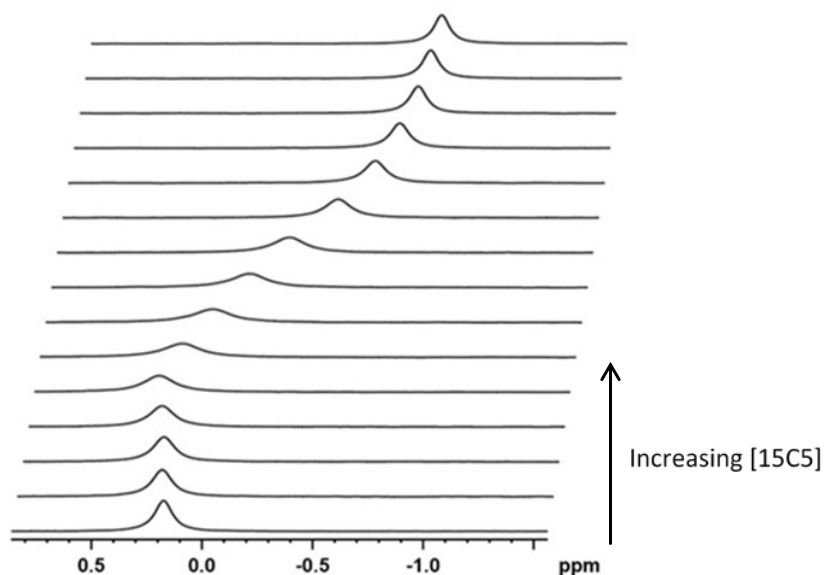


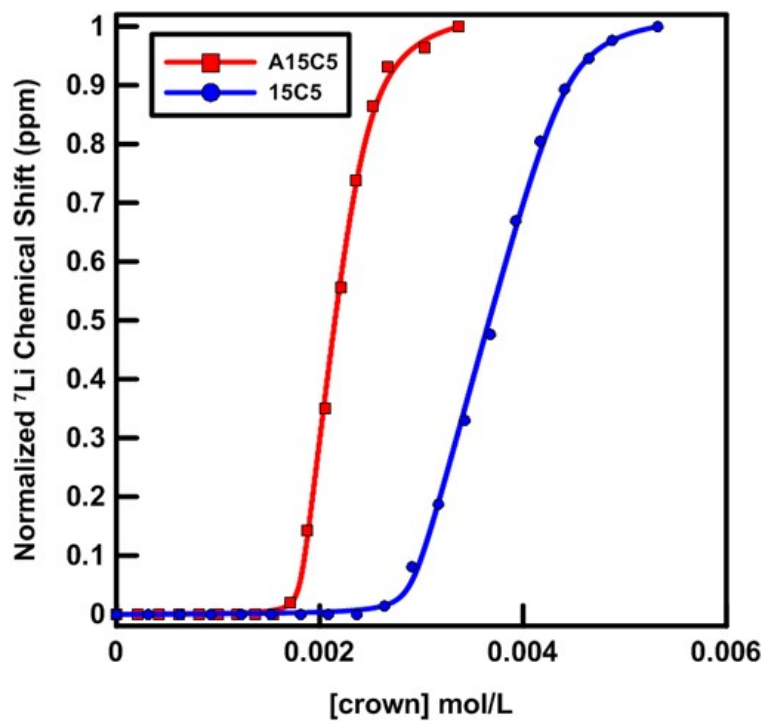
**Figure 4.5.** Experimental  $^7\text{Li}$  chemical shifts for  $\text{Li}^+$  binding with increasing amounts of 15-crown-5 (15C5) from the bottom (0 mM) to the top ( $\sim 3$  mM) of the figure. Each spectrum represents an approximate increase in 15-crown-5 molarity of 0.2 mM. These were all collected in the presence of a constant amount of both  $\text{MnCl}_2$  and  $\text{LiTFSI}$  in the propylene carbonate solvent, each at  $\sim 1$  mM concentration

The effect of the pseudocontact shift was accounted for by appropriately normalizing the titrations involving manganese. (1) In instances where  $K_{\text{Li}} \ll K_{\text{Mn}}$  any positive chemical shift trend was calibrated to a chemical shift of zero, since the primary contribution was a chemical shift change facilitated by manganese and not by the crown ether. (2) All data points which showed negative chemical shift trends were treated as-

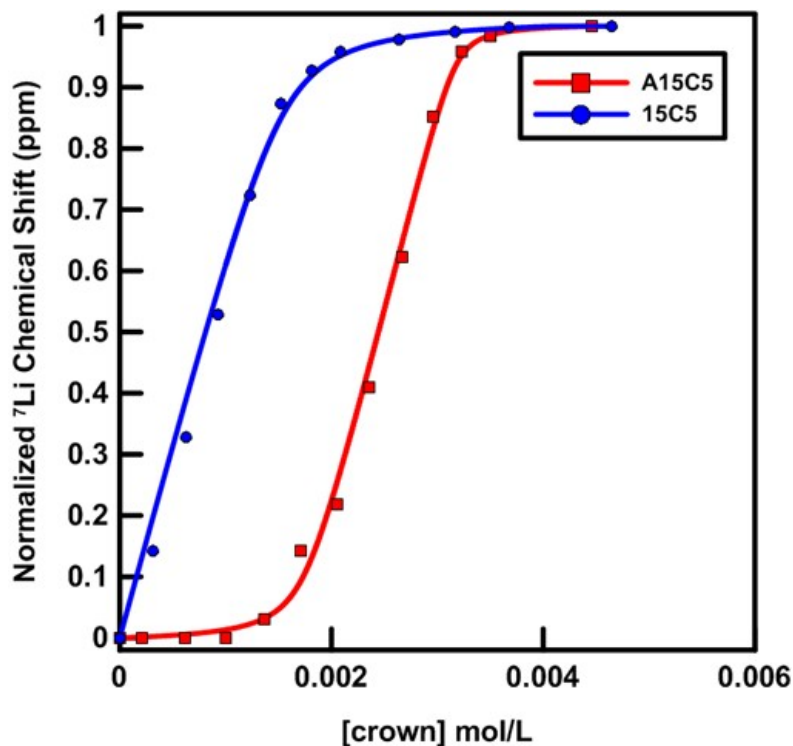
measured. (3) Conversely, for  $K_{Li} \gg K_{Mn}$  lithium is sequestered within the crown ether and does not appear to experience a significant pseudocontact shift. This results in no positive chemical shift trend and is again treated normally. In the regime  $K_{Li} \approx K_{Mn}$  the interpretation becomes more ambiguous. However, since our primary goal is an order of magnitude comparison of relative binding affinities, the state of  $K_{Li} \approx K_{Mn}$  should still be observable, albeit with a higher associated uncertainty.

Figure 4.6 displays binding curves for 1-aza-15-crown-5 and 15-crown-5 towards lithium in the presence of  $Mn^{2+}$ . A strong preference for  $Mn^{2+}$  was found for both A15C5 and 15C5 in the presence of lithium (2000:1 and 630:1  $K_{Mn}:K_{Li}$  respectively). Thus one might anticipate that incorporation of either crown ether into a polymeric support might assist capture of  $Mn^{2+}$  dissolved in the electrolyte. However, given the uncertainties surrounding the oxidation state of manganese cations in LIB solutions<sup>23</sup>, additional binding curves were collected for  $Mn^{3+}$  cations. Figure 4.7 displays the results of these experiments, and aza-15-crown-5 shows a stronger relative affinity for  $Mn^{3+}$  than does 15-crown-5. Specifically, a 60:1 ratio of equilibrium constants was observed in favour of  $Li^+$  for 15-crown-5 and the preference switches to 100:1 in favour of  $Mn^{3+}$  for aza-15-crown-5. These results have significant consequences for the use of crown ethers to capture manganese cations. If  $Mn^{3+}$  is the dominant species produced during electrochemical cycling, then it is unlikely that 15C5 will be able to trap significant amounts of manganese cations, especially given its substantially lower concentration relative to  $Li^+$ . On the other hand, since A15C5 can trap manganese in both oxidation

states effectively in the presence of  $\text{Li}^+$ , it would appear to be the better  $\text{Mn}^{\text{x+}}$  cation chelating agent choice for use in LIBs.



**Figure 4.6.** Experimental  $^7\text{Li}$  chemical shifts for  $\text{Li}^+$  binding to increasing amounts of 1-aza-15-crown-5 (A15C5) and 15-crown-5 (15C5) in the presence approximately equimolar amounts of  $\text{MnCl}_2$  and propylene carbonate solvent.



**Figure 4.7.** Experimental  $^7\text{Li}$  chemical shifts for  $\text{Li}^+$  binding to increasing amounts of 1-aza-15-crown-5 and 15-crown-5 in the presence approximately equimolar amounts of  $\text{Mn}(\text{OAc})_3$  in propylene carbonate solvent.

Work has already been conducted on attaching A15C5 onto a vinylbenzyl-divinylbenzene polymer backbone with varying degrees of cross-linking. The resultant polymers were then incorporated into separators and tested for their influence on cycling performance. While the polymers are not soluble in propylene carbonate, they can be dispersed for long enough time to conduct NMR measurements on homogenous suspensions. Thus the methodology applied to the molecular crown ethers can also be utilized with a polymeric crown ether, with preliminary results presented in Figure 4.8.

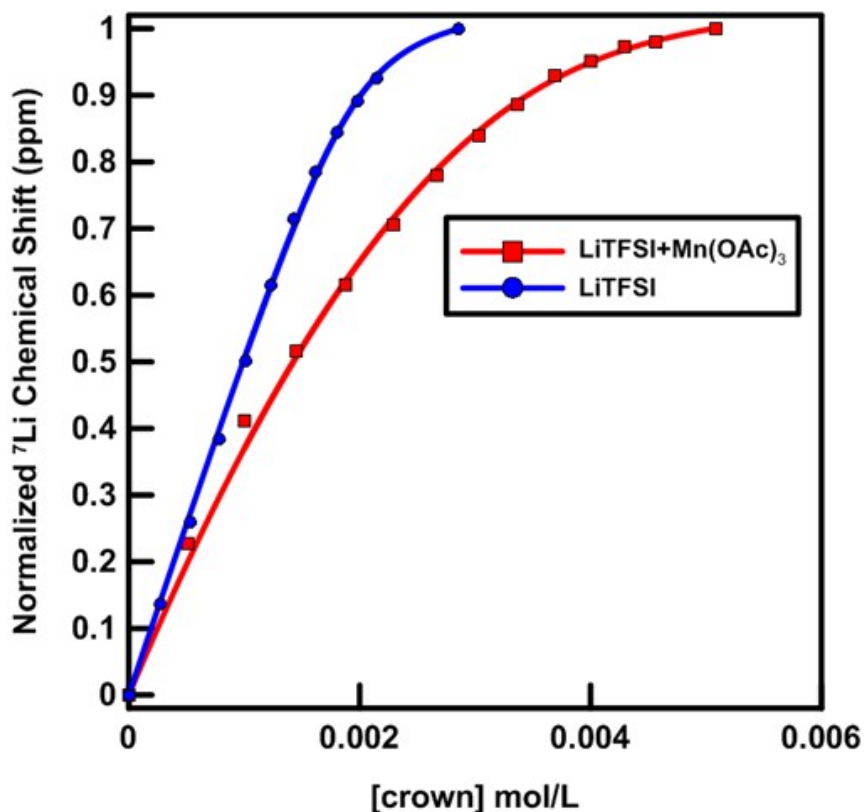


**Figure 4.8.** Experimental <sup>7</sup>Li chemical shifts with Li<sup>+</sup> binding to increasing amounts of 10 wt% divinylbenzene – 90 wt% vinylbenzyl-aza-15-crown-5 in both a manganese free environment and one containing Mn(CH<sub>3</sub>COO)<sub>3</sub> and propylene carbonate solvent.

While the lithium cation binding capacity is maintained with  $K_{Li} > 10^4$  L/mol, the selectivity for manganese cations drops significantly, such that the equilibrium constant ratio is approximately 2:1 in favor of lithium. A possible explanation for this behavior may be the under-utilization of the trapping sites as a combined effect of the spherical particle morphology (see Figure 4.9) and an increased Coulombic repulsion by a factor 9 between two Mn<sup>3+</sup> ions over that between two Li<sup>+</sup> ions.

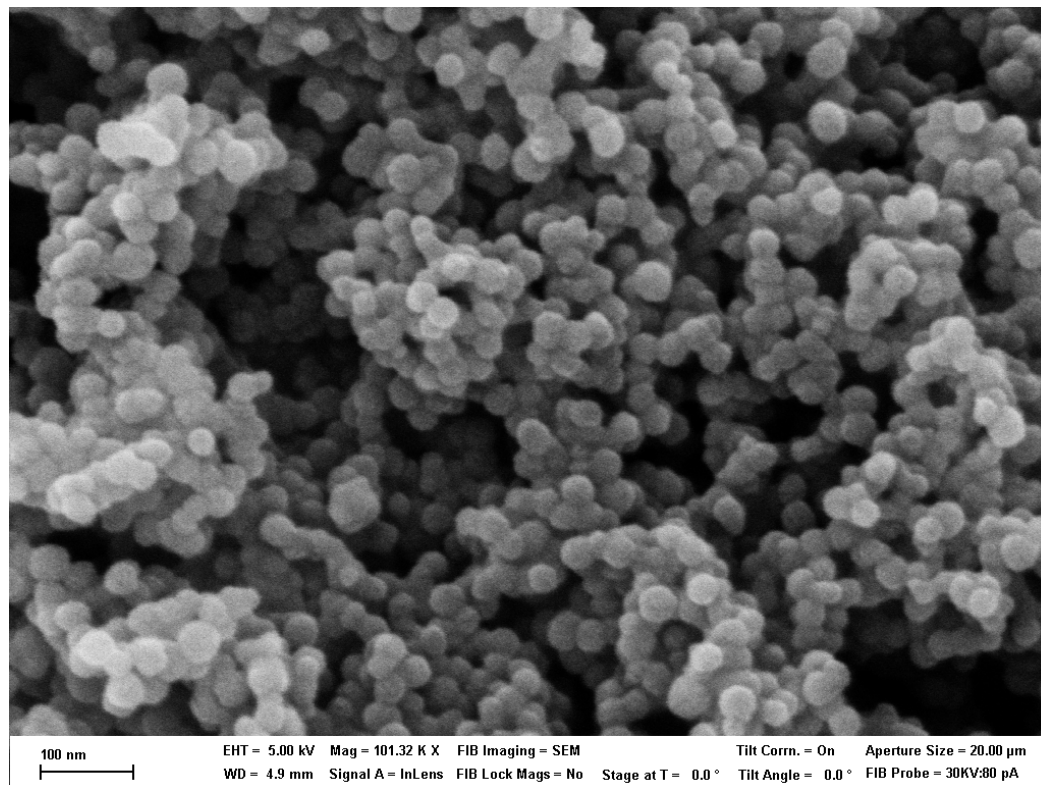


**Figure 4.9.** SEM micrograph of the 10 wt% divinylbenzene – 90 wt% vinylbenzyl-aza-15-crown-5 polymer from the present study. The polymeric particles have a spherical morphology with diameters ranging from 20 to 50 nm.

#### 4.5 - Conclusions and Outlook

NMR measurements of  ${}^7\text{Li}$  chemical shift can be used as an indirect measure of the binding affinity of various chelating agents (crown ethers, iminodiacetic acid salts, EDTA, etc.) for  $\text{Li}^+$  or  $\text{Mn}^{x+}$  ions. As manganese cations were indirectly studied, additional complications related to their paramagnetism had to be accounted for. Lithium itself has a particularly strong affinity for both crown ethers, with an equilibrium constant in excess of  $10^4$  L/mol. Unfortunately, NMR cannot be used to reliably distinguish equilibrium constants higher than this value. However, studies of competitive bonding of

$\text{Li}^+$  and  $\text{Mn}^{2+/3+}$  can shed some light on relative binding strengths. We showed that  $\text{Mn}^{2+}$  has an equilibrium constant more than 100 times greater than  $\text{Li}^+$  with both crown ethers. It is noteworthy that only A15C5 can trap  $\text{Mn}^{3+}$  in the presence of lithium. These results imply that A15C5 is the better choice than 15C5 for trapping manganese cations in lithium ion batteries. However, measurements on a suspension of the polymeric A15C5 revealed a substantial drop in  $\text{Mn}^{3+}$  binding affinity relative to lithium. While still approximately equivalent to lithium in affinity for A15C5, the excess lithium concentration of battery electrolytes renders this decrease particularly significant. The complete understanding for the drop in affinity for  $\text{Mn}^{x+}$  cations between the molecular form of a trap and the factors that maximize the ion trapping ability polymeric chelating agents (type of backbone, morphology, length of linker, amount of cross-linking, etc.) is the subject of ongoing research.

The present study is meant to demonstrate that our methodology is applicable to polymeric materials functionalized with chelating agents and can hence serve as a screening tool to inform and assist the development of more effective manganese cation trapping materials. Of immediate concern is to establish whether the reduced affinity for  $\text{Mn}^{3+}$  cations for azacrown cation traps attached to polymers over their free (molecular) form is an effect intrinsic to the tethering of the chelating agents to a polymer or rather an issue related to trapping site accessibility due to the amount of cross-linking in the polymer and its morphology. This question will be addressed by examining trapping agents (azacrown ethers, iminodiacetic acid salts, etc.) attached to homopolymers (i.e., linear chain polymers) which are devoid of any cross-linking as a possible cause for

limited trapping site accessibility. Other activities worth pursuing in the future are: (1) quantify and rank the relative  $Mn^{x+}$  cation trapping ability of various chelating agents in molecular form; (2) investigate the effect of cross-linking on the manganese cation trapping ability of polymeric trapping agents with spherical morphology; (3) investigate the effect of polymer morphology (linear chains, cross-linked spherical particles, dendrimers) on relative cation affinities; (4) investigate the effect of various electrolyte solution on manganese cations trapping.

#### 4.6 - References

- (1) Thackeray, M.J. Manganese Oxides for Lithium Batteries. *Prog. Solid State Chem.* **1997**, *25*, 1-71.
- (2) Winter, M; Brodd, R.J. What are Batteries, Fuel Cells, and Supercapacitors? *Chem. Rev.* **2004**, *104*, 4245-4269.
- (3) Tarascon, J.-M. Key Challenges in Future Li-Battery Research. *Phil. Trans. R. Soc. A* **2010**, *368*, 3227–3241.
- (4) Manthiram, A. Materials Challenges and Opportunities of Lithium Ion Batteries. *J. Phys. Chem. Rev.* **2011**, *2*, 176–184.
- (5) Goodenough, J.B; Park, K.-S. The Li-ion Rechargeable Battery: A Perspective. *J. Am. Chem. Soc.* **2013**, *135*, 1167–1176.

- (6) Dou, S. Review and Prospect of Layered Lithium Nickel Manganese Oxide as Cathode Materials for Li-ion batteries, *J. Solid State Electrochem.* **2013**, *17*, 911-926.
- (7) Liu, D.; Zhu, W.; Trottier, J.; Gagnon, C.; Barray, F.; Guerfi, A; Mauger A.; Groult, H.; Julien, C. M.; Goodenough, J. B.; Zaghbi, K. Spinel Materials for High-Voltage Cathodes in Li-Ion Batteries. *RSC Adv.* **2014**, *4*, 154–167.
- (8) Dou, S. Review and Prospects of Mn-Based Spinel Compounds as Cathode Materials for Lithium-Ion Batteries. *Ionics* **2015**, *21*, 3001-3030.
- (9) Jang, D. H.; Shin, Y. J.; Oh, S. M. Dissolution of Spinel Oxides and Capacity Losses in 4 V Li /  $\text{Li}_x\text{M}_2\text{O}_4$  cells. *J. Electrochem. Soc.* **1996**, *143*, 2204–2211.
- (10) G. Amatucci, C. N. Schmutz, A. Blyr, C. Sigala, A. S. Gozdz, D. Larcher, and J.-M. Tarascon, Materials' Effects on the Elevated and Room Temperature Performance of C/LiMn<sub>2</sub>O<sub>4</sub> Li-ion Batteries *J. Power Sources* **1997**, *69*, 11-25.
- (11) G. Pistoia, A. Antonini, R. Rosati, and D. Zane, Storage Characteristics of Cathodes for Li-ion Batteries. *Electrochim. Acta* **1997**, *41*, 2683-2689.
- (12) Y. Xia, Y. Zhou, and M. Yoshio, Capacity Fading on Cycling of 4 V Li/LiMn<sub>2</sub>O<sub>4</sub> Cells. *J. Electrochem. Soc.* **1997**, *177*, 2593-2600.
- (13) Choi, W.; Manthiram, A. Comparison of Metal Ion Dissolutions from Lithium Ion Battery Cathodes. *J. Electrochem. Soc.* **2006**, *153*, A1760-A1764.

- (14) Li, C.; Zhang, H. P.; Fu, L. J.; Liu, H.; Wu, Y. P.; Rahm, E.; Holze, R.; Wu, H. Q. Cathode Materials Modified by Surface Coating for Lithium Ion Batteries. *Electrochim. Acta* **2006**, *51*, 3872-3883.
- (15) Jung, Y. S.; Cavanagh, A. S.; Dillon, A. C.; Groner, M. D.; George, S. M.; Lee, S. - H. Enhanced Stability of LiCoO<sub>2</sub> Cathodes in Lithium-Ion Batteries Using Surface Modification by Atomic Layer Deposition. *J. Electrochem. Soc.* **2010**, *157*, A75-A81.
- (16) Meng, X.; Yang, X.-Q.; Sun, X. Emerging Applications of Atomic Layer Deposition for Lithium-Ion Battery Studies. *Advanced Materials* **2012**, *24*, 3589-3615.
- (17) Kumagai, N.; Komaba, S.; Kataoka, Y.; Koyanagi, M. Electrochemical Behavior of Graphite Electrode for Lithium Ion Batteries in Mn and Co Additive Electrolytes. *Chem. Lett.* **2000**, 1154-1155.
- (18) Komaba, S.; Kumagai, N., Kataoka, Y. Influence of Manganese(II), Cobalt(II), and Nickel(II) Additives in Electrolyte on Performance of Graphite Anode for Lithium-Ion Batteries *Electrochim. Acta* **2002**, *47*, 1229-1239.
- (19) Tsujikawa, T.; Yabuta, K.; Matsushita, T.; Arakawa, M.; Hayashi, K. A Study on the Cause of Deterioration in Float-Charged Lithium-Ion Batteries Using LiMn<sub>2</sub>O<sub>4</sub> as a Cathode Active Material. *J. Electrochem. Soc.* **2011**, *158*, A322-A325.

- (20) Chu, I.H.; Zhang, H.; Dearden, D.V. Macrocyclic Chemistry in the Gas Phase: Intrinsic Cation Affinities and Complexation Rates for Alkali Metal Cation Complexes of Crown Ethers and Glymes. *J. Am. Chem. Soc.* **1993**, *115*, 5736-5744.
- (21) Bradshaw, J.S.; Izatt, R.M. Crown ethers: The Search for Selective Ion Ligating Agents. *Acc. Chem. Res.* **1997**, *30*, 338-345.
- (22) Ziv, B.; Levy, N.; Borgel, V.; Li, Z.; Levi, M. D.; Aurbach, D.; Pauric, A. D.; Goward, G. R.; Fuller, T. J.; Balogh, M. P.; H. Manganese Sequestration and Li-Ion Batteries Durability Enhancement by Polymeric 18-crown-6 Ethers. *J. Electrochem. Soc.* **2014**, *161*, A1213–A1217.
- (23) Li, Z.; Pauric, A. D.; Goward, G. R.; Fuller, T. J.; Ziegelbauer, J. M.; Balogh, M. P.; Halalay, I. C. Manganese Sequestration and Improved High-Temperature Cycling of Li-Ion Batteries by Polymeric aza-15-crown-5. *J. Power Sources* **2014**, *272*, 1134-1141.
- (24) Høiland, H.; Ringseth, J. A.; Brun, T. S. Cation-Crown Ether Complex Formation in Water. II. Alkali and Alkaline Earth Cations and 12-crown-4, 15-crown-5, and 18-crown-6. *J. Solution Chem.* **1979**, *8*, 779–792.
- (25) More, M. B.; Ray, D.; Armentrout, P. B. Intrinsic Affinities of Alkali Cations for 15-Crown-5 and 18-Crown-6: Bond Dissociation Energies of Gas-Phase  $M^+$ -Crown Ether Complexes. *J. Am. Chem. Soc.* **1999**, *121*, 417–423.
- (26) Izatt, R.M.; Terry, R.E.; Nelson, D.P.; Chan, Y.; Eatough, D.J.; Bradshaw, J.S.; Hansen, L.D.; Christensen, J.J. Calorimetric Titration Study of the Interaction of

- Some Uni- and Bivalent Cations with Benzo-15-crown-5, 18-crown-6, dibenzo-24-crown-8, and dibenzo-27-crown-9 in Methanol-Water Solvents, at 25 °C and  $\mu = 0.1$ . *J. Am. Chem. Soc.* **1976**, *98*, 7626-7630.
- (27) Izatt, R.M.; Terry, R.E.; Hansen, L.D.; Avondet, A.G.; Bradshaw, J.S.; Dalley, N.K.; Jensen, T.E.; Christensen, J.J.; Haymore, B.L. A Calorimetric Titration Study of Uni- and Bivalent Metal Ion Interaction with Several Thia Derivatives of 9-crown-3, 12-crown-4, 15-crown-5, 18-crown-6, 24-crown-8, and with Several Oxathiapentadecanes in Water or Water-Methanol solvents at 25°C. *Inorganica Chim. Acta.* **1978**, *30*, 1-8.
- (28) Izatt, R.M.; Bradshaw J.S.; Nielsen, S.A.; Lamb, J.D.; Christensen, J.J.; Sen, D. Thermodynamic and Kinetic Data for Cation-Macrocycle Interaction. *Chem. Rev.* **1985**, *85*, 271-339.
- (29) Izatt, R.M.; Pawlak, K.; Bradshaw, J.S.; Bruening, R.L. Thermodynamic and Kinetic Data for Macrocycle Interactions with Cations and Anions. *Chem. Rev.* **1991**, *91*, 1721-2085.
- (30) Steed, J.W. First and Second-sphere Coordination Chemistry of Alkali Metal Crown Ether Complexes. *Coord. Chem. Rev.* **2001**, *215*, 171-221.
- (31) Glendening, E. D.; Feller, D.; Thompson, M. A. An Ab-Initio Investigation of the Structure and Alkali Metal Cation Selectivity of 18-crown-6. *J. Am. Chem. Soc.* **1994**, *116*, 10657–10669.

- (32) Gafni, A.; Cohen, Y. Complexes of Macrocycles with  $\Gamma$ -Cyclodextrin as Deduced from NMR Diffusion Measurements. *J. Org. Chem.* **1997**, *62*, 120–125.
- (33) Hirose, K. A Practical Guide for the Determination of Binding Constants. *J. Inclusion Phen.* **2001**, *39*, 193–209.
- (34) Rong, Q.; Español, M.; Mota de Freitas, D.; Geraldès, C. F. G. C. Lithium-7 NMR Relaxation Study of Lithium Binding in Human Erythrocytes. *Biochemistry* **1993**, *32*, 13490–13498.
- (35) Smetana, A. J.; Popov, A. I. Lithium-7 Nuclear Magnetic Resonance and Calorimetric study of Lithium Crown Complexes in Various Solvents. *J. Solution Chem.* **1980**, *9*, 183–196.
- (36) Soong, L. L.; Leroi, G. E.; Popov, A. I. Cesium-133 NMR Studies of Crown Ether-Cesium(1+) Complexes in High Dielectric Amide Solvents. *Inorg. Chem.* **1990**, *29*, 1366–1370.
- (37) Aoshima, T.; Okahara, K.; Kiyohara, C.; Shizuka, K. Mechanisms of Manganese Spinel Dissolution and Capacity Fade at High Temperature. *J. Power Sources* **2001**, *97*, 377–380.
- (38) Yang, L.; Takahashi, M.; Wang, B. A Study on Capacity Fading of Lithium-ion Battery with Manganese Spinel Positive Electrode During Cycling. *Electrochim. Acta* **2006**, *51*, 3228–3234.
- (39) Danil de Namor, A. F.; Llosa Tanco, M. A.; Solomon, M.; Ng, J. C. Y. Thermodynamic, Structural, and Conductance Studies of Lithium Coronand

- Electrolytes Relevant to Lithium Battery Technology, *J. Phys Chem.* **1994**, *98*, 11796 – 11802.
- (40) Nagasubramanian, G.; Di Stefano, S. 12-Crown-4 Ether-Assisted Enhancement of Ionic Conductivity, *J. Electrochem Soc.* **1990**, *137*, 3830-2835.
- (41) Wilkinson, D. P.; Dahn, J. R. Electrolyte Solution Sequestering Agents for Electrochemical Cells Having Carbonaceous Electrodes, *US Patent 5,130,211*, **1992**.
- (42) Foster, D.L.; Behl, W.K.; Wolfenstine, J. The effect of Various Electrolyte Additives on Reversible Li-graphite Intercalation. *J. Power Sources* **2009**, *85*, 299-301.
- (43) Fakhari, A. R.; Shamsipur, M. An NMR Study of the Stoichiometry and Stability of Lithium Ion Complexes with 12-crown-4, 15-crown-5 and 18-crown-6 in Binary Acetonitrile-Nitrobenzene Mixtures. *J. Incl. Phenom. Macrocycl. Chem.* **1996**, *26*, 243–251.
- (44) Shamsipur, M.; Irandoust, M. A proton NMR Study of the Stoichiometry and Stability of 18-Crown-6 Complexes with  $K^+$ ,  $Rb^+$  and  $Tl^+$  Ions in Binary Dimethyl Sulfoxide-Nitrobenzene mixtures. *J. Solution Chem.* **2008**, *37*, 657–664.
- (45) Kurland, R. J.; McGarvey, B. R. Isotropic NMR Shifts in Transition Metal Complexes: The Calculation of the Fermi Contact and Pseudocontact terms. *J. Magn. Reson.* **1970**, *2*, 286–301.
- (46) Gochin, M.; Roder, H. Protein Structure Refinement Based on Paramagnetic NMR shifts: Applications to Wild-type and Mutant Forms of Cytochrome C. *Protein Sci. Publ. Protein Soc.* **1995**, *4*, 296–305.



## **Chapter 5 - Cellulose Substrates and their Application to Solid State NMR of Lithium Ion Batteries: A Case Study in Silicon Monoxide Anodes**

The chapter described here was concerned with the use of cellulose substrates and how their properties assist in conducting NMR characterization of LIB materials. In particular, silicon monoxide was used as a case study to showcase both the reasonable performance and relative ease with which detailed  $^{29}\text{Si}$  NMR spectra could be obtained. Additionally, the lack of metallic active components enabled novel  $^7\text{Li}$  in-situ NMR designs which were applied to the study of silicon monoxide. These results were directly compared against the lithiation behaviour of metallic silicon. Cumulatively, the work provides new insights into the use of silicon monoxide as a LIB anode and more generally validates the use of cellulosic substrates in the NMR characterization of LIB materials towards both in-situ and ex-situ NMR characterizations.

This manuscript was prepared for submission to a peer-reviewed journal by the authors Allen D. Pauric, Gillian R. Goward, and Meng Jiang. Data collection, initial analyses, and initial draft manuscript preparation were conducted by Allen D. Pauric. Final analyses and manuscript edits included contributions from Gillian R. Goward and Meng Jiang.

## 5.1 - Introduction

Substantial research has accumulated with regard to silicon anode materials as a replacement to graphite.<sup>1</sup> The primary benefit of silicon based anode materials is the expanded gravimetric capacity, ranging as high as 4000 mAh/g.<sup>2</sup> When compared to graphite at 372 mAh/g the increase in energy density associated with silicon seems particularly promising. However, the primary drawback of silicon anode materials is tied to the dramatic volume expansion (ca. 300%) upon lithiation.<sup>3</sup> After multiple cycles the repeated volume expansion and contraction can pulverize the active material and result in separation of the silicon particles from the electrically conductive carbon matrix. Additionally, this physical instability disrupts the solid electrolyte interphase (SEI) which forms at the surface of the silicon particles. In doing so, continued breakdown of the electrolyte is promoted, thickening the SEI layer and resulting in an associated increase in electrical resistance along with depletion of the electrolyte components.<sup>4</sup>

The typical approach towards using silicon anodes is the mitigation and/or accommodation of the associated volume expansion.<sup>5</sup> Many highly cited articles on silicon metal explain such approaches in greater detail.<sup>6-8</sup> Simultaneously, there has been substantial research into a detailed understanding of the electrochemical lithiation of silicon. Towards this end, in-situ <sup>7</sup>Li NMR has proven a valuable tool. For instance a seminal publication by Grey et. al.<sup>9</sup> showed the formation of a metastable crystalline lithium silicide phase towards the end of lithiation which dissipates upon discharge. Such repeated transitions between amorphous and crystalline phases have been linked to excessive capacity fade.<sup>10,11</sup> Importantly, the spectral feature associated with crystalline

silicon was unobserved in ex-situ measurements, helping to underline the importance of in-situ NMR in the observation of metastable states.

A less commonly considered alternative is the use of silicon monoxide instead of pure silicon.<sup>12</sup> The primary advantage of SiO is the presence of irreversible lithiation species including  $\text{Li}_2\text{O}$  and  $\text{Li}_4\text{SiO}_4$  which serve as a buffer to the volume expansion.<sup>13</sup> Their presence reduces the volume expansion upon lithiation by 50% in comparison to silicon metal.<sup>12</sup> Unfortunately, the enhanced cyclability necessarily incorporates additional irreversible capacity upon lithiation of the buffer species. Additionally, practical anode capacities are typically on the order of 1000 mAh/g. Nevertheless, the potential for increased cycling stability coupled with a reversible capacity that is sufficient for state of the art transition metal cathodes makes them a promising anode candidate.

NMR studies of the material are sparse with only a handful having been reported.<sup>14,15</sup> While ex-situ  $^7\text{Li}$  NMR of cycled active material exists, no in-situ experiments have been conducted thus far. Furthermore,  $^{29}\text{Si}$  spectra of the charge/discharge process are also unavailable, made exceedingly difficult by long relaxation times coupled with the low natural abundance, low gyromagnetic ratio, and small sample volumes associated with ex-situ analysis of SiO anodes. The publication presented here addresses the shortcomings in current literature on SiO through the application of in-situ  $^7\text{Li}$  NMR and ex-situ  $^{29}\text{Si}$ . Use of in-situ methodologies is meant to complement existing research on pure silicon and in particular to search for a similar amorphous to crystalline transition. Detailed ex-situ  $^{29}\text{Si}$  NMR of cycled anodes can show specific features of this including the development of the  $\text{Li}_4\text{SiO}_4$  buffer phase, and provide insight on the nature of the

reversible lithium silicides.

To enable these experiments we propose an unorthodox yet effective strategy whereby the copper current collector is replaced with a cellulosic substrate. Cellulose based energy storage materials have been investigated previously, including their potential applications to lithium ion batteries.<sup>16</sup> The most prominent use is as a binder, including the extensively studied carboxymethylcellulose.<sup>17</sup> This strong binder material has demonstrated greater adhesive strength in comparison to the commonly used polyvinylidene fluoride, making it particularly useful in mitigating the effects of volume expansion.<sup>18</sup> Additionally, the high porosity and wettability of cellulosic materials has piqued interest for their use in composite battery separator materials.<sup>19</sup> Further exploratory studies have demonstrated the notable performance of complete cellulose solutions where all the battery components included the use of cellulose and its derivatives.<sup>20</sup> In addition to the performance arguments, there are the associated environmental benefits to utilizing biologically derived materials in this context.

To directly compete with established LIB technology, extensive testing of such a solution would be necessary. Since LIBs are required to operate over thousands of cycles during their usable lifetime, a cellulosic solution would have to meet a similar standard. This is of course neglecting issues with scale up and whether there would be a significant enough performance benefit to merit the transition. Nevertheless, they represent an intriguing avenue for improvement in both existing and emerging LIB technology.

Irrespective of the long term implications, cellulosic substrates incorporate notable advantages towards NMR spectral acquisition of electrode materials. For ex-situ

experiments it can significantly increase active material loading per unit area of electrode. Typical active material loadings are in the range of 3-4 mg/cm<sup>2</sup>, whereas the silicon monoxide anodes used in this study maintained active material loadings of 7-10 mg/cm<sup>2</sup>.<sup>21,22</sup> This was achieved through the improved adhesion of electrode slurries using water based binders onto the porous substrate. Similar loadings on traditional metallic substrates are more difficult to achieve without compromising structural integrity. The porosity also enables the stacking of multiple electrodes in a single coin cell. While this reduces the effective cycling rate attainable by increasing ionic resistance, it dramatically increases the amount of active material per coin cell. For low sensitivity nuclei including <sup>29</sup>Si the resultant signal boost can be particularly advantageous.

Increasing the sample size in this manner also has key benefits for the implementation of in-situ <sup>7</sup>Li NMR. Specifically, in-situ NMR studies suffer from sensitivity issues related to both the broad resonances and the RF interference associated with the metallic current collectors. To minimize RF permeability effects, a horizontal geometry is typically employed. These cells are encased in a plastic, sealable bag inside of which the battery components are assembled and isolated from the outside environment. Copper and aluminum mesh current collectors are employed to allow RF penetration. The entire assembly is then surrounded by a solenoid coil which possesses enhanced sensitivity in comparison to the saddle coil used in vertical geometries.<sup>23</sup>

Various in-situ studies conducted to date have utilized adaptations of the aforementioned design, from some of the very first studies of hard carbon anodes<sup>24</sup> to recent multinuclear studies on LiFePO<sub>4</sub> and NaFePO<sub>4</sub>.<sup>25</sup> Both these and other in-situ

experiments have been highly successful in characterizing lithium ion batteries during operation, though RF permeability and active material loading remain common concerns. To this end a cylindrical geometry as enabled by the use of a cellulosic substrate is thus considered. This configuration provides an improved filling factor for the active material and retains use of the more efficient solenoid coil geometry. As mentioned with the ex-situ experiments, the permeability of the cellulose electrodes allows multiple layers to be cycled simultaneously, albeit at the cost of a reduced cycling rate. Furthermore, the lack of a metallic current collector improves RF permeability.

The following results demonstrate that the use of cellulosic substrates as an anode material enables the acquisition of ex-situ  $^{29}\text{Si}$  and  $^7\text{Li}$  in-situ data while retaining significant cyclability at high active material loadings.

## 5.2 - Experimental

Silicon monoxide electrode slurries were prepared by first dissolving 125 mg of sodium alginate binder (Sigma Aldrich) into 10 ml of deionized water. The mixture was mechanically stirred until mostly dissolved and then sonicated for 60 minutes to ensure complete dissolution of the binder. Meanwhile a solid mixture of 1.4g SiO powder (>99%, 325 mesh, Sigma Aldrich) and 0.425g of Super-P C65 carbon black was coarsely mixed together. After sonication, the SiO/C powder mixture was added to the binder solution, mechanically stirred for 5-10 minutes, and the whole mixture sonicated for an additional 60 minutes. The prepared slurry was then cast onto both sides of a 10x10 cm section of KimWipe®. A five minute room temperature air drying step was included in-

between flips to prevent active material from sticking to the glass substrate upon which it was being cast. The prepared electrode was then dried in air at 80°C overnight and transferred into an argon filled glovebox. Silicon metal anodes were prepared in an identical fashion (99.999%, 325 mesh, Alfa Aesar).

Battery construction involved the use of a polypropylene separator coupled with 100  $\mu\text{L}$  of 1M  $\text{LiPF}_6$  in EC/DEC and a lithium metal counter electrode. Only a single punched SiO anode was used for the cycling stability studies, whereas two electrodes were used when preparing samples for ex-situ  $^{29}\text{Si}$  NMR. Cycling rates were C/10 and C/50 for cycling stability and ex-situ analysis respectively.

NMR measurements of the ex-situ cells were performed at several points in the charge/discharge process and involved  $^{29}\text{Si}$  MAS-NMR experiments at 23 kHz in a 3.2 mm rotor. A simple Hahn echo was used with a 6  $\mu\text{s}$  90° pulse and a recycle delay of 10 seconds for every sample besides the pristine material. Because of the long  $T_1$  times measured (in excess of 600s via inversion recovery) the associated recycle delay was increased to 120s. Each direct  $^{29}\text{Si}$  spectrum required approximately 1 day of acquisition on a fully filled rotor.

In-situ experiments utilized an identical anode preparation procedure. Cell construction involved commonly available materials. Specifically, a 3 ml syringe was obtained with the plunger and approximately 1 cm of syringe top removed. The bottom section of the syringe was melted using a soldering iron such that it formed a seal and the total length of the modified syringe was no greater than 6 cm.

Subsequent to this, a silicone septum with just over a 1 cm external diameter was cut

to 0.5 cm in length and pierced with two 16 cm lengths of copper wire, one of these being bare and the other being epoxy coated copper magnet wire. The epoxy coating of the magnet wire was removed both on the outside end and at a 6 cm section meant to go in the interior of the cell. The use of the coated wire is to prevent accidental short circuits as the assembly is placed in the modified syringe. Further to this, the plunger of a 1 ml syringe was extracted and cut to approximately 5 cm in length. The wide end was trimmed such that it fit inside the modified syringe thus centering the plastic core. The prepared magnet wire was then wrapped around the plastic core.

Further assembly involved work in the glovebox where a 5x1 cm section of lithium foil was cut in half and then flattened manually as thin as possible while maintaining structural integrity. The prepared lithium was subsequently rolled with a section of separator at slightly larger dimensions around the plastic core and wrapped around the magnet wire section. With the lithium and separator prepared a 4x2 cm section of anode was wrapped around the prepared core and held in place with the bare copper wire. In an attempt to promote better contact with the separator, some sections of the anode were further wrapped with Teflon tape. The entire assembly was placed loosely in the modified syringe, filled with 0.5 M LiFSI in EC/DEC, and sealed from the environment via the friction of the septum against the body of the syringe (Figures 7.3.3.1 and 7.3.3.1 in the appendix).

Acquisition of the in-situ NMR measurements necessitated additional considerations. The fully constructed cell was first attached to metal screws that were pre-drilled into the probe body. Their purpose was to relieve strain on the cell as the connections to the

outside of the probe were being made. These connections were linked to the outside via two thin strands of magnet wire that fit in-between the probe body and the metallic sheath surrounding it. The circuit was completed through two 50 kHz RF filters on each channel. Furthermore, residual electronic noise was substantially reduced by grounding the BNC cables to the body of the magnet. NMR parameters involved a 13 us 90° pulse on a 200 MHz magnet with a recycle delay of two seconds.

### **5.3 - Results and Discussion**

Before performing detailed NMR analysis of the SiO anodes it was important to perform cycling in a standard coin cell context. Adequate cyclability in this regime proves their validity in an in-situ setting, as well as hinting towards possible directions in mitigating capacity fade. Along this vein, Figure 5.1 depicts the capacity and coulombic efficiency performance of the prepared SiO anodes. The first charge/discharge cycle includes reversible capacity of about 1250 mAh/g and a coulombic efficiency of 50%. Since the SiO material used in this study is not designed for electrode application, it is expected that both the capacity and initial coulombic efficiency are relatively lower than battery grade materials, typically 1500mAh/g and 70% respectively.<sup>26</sup> The low first cycle efficiency is due to both initial SEI layer formation and the creation of irreversible lithium silicates and oxides.<sup>27</sup> However, the efficiency rapidly approaches 100% on subsequent cycles suggesting a stabilization of the irreversible reactions.

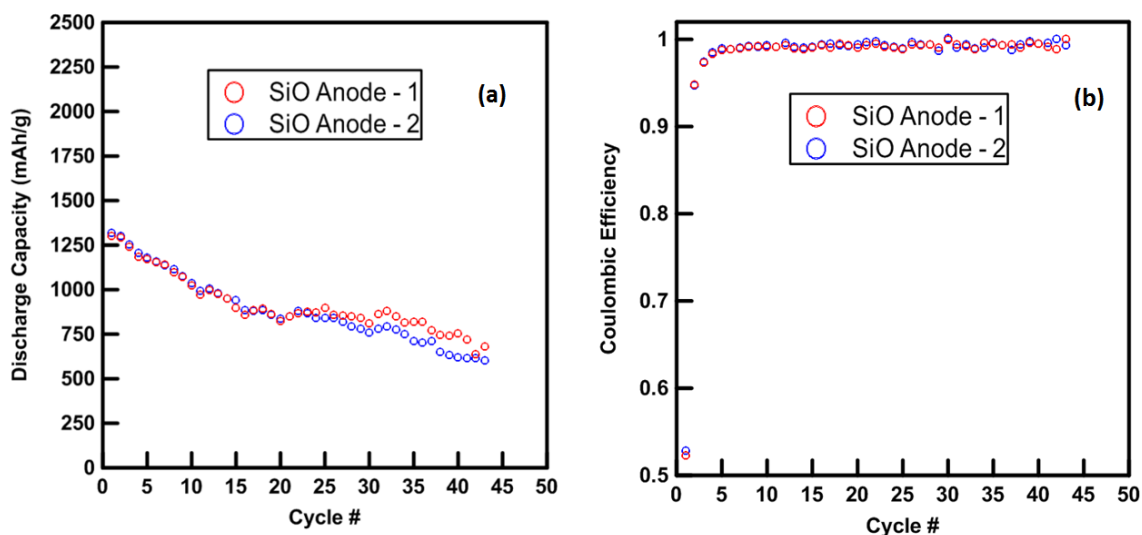


**Figure 5.1.** Silicon monoxide capacity (a) and coulombic efficiency (b) data over multiple cycles showing an associated variation in performance. An additional replicate was included to further verify the observed trend.

The cycle life data shows a continued decline in capacity over subsequent cycles on the order of 5-20 mAh/g per cycle retaining only 60% of its original capacity after 40 iterations. Although, given the high current density achieved, even this performance has merit. Ultimately, the electrochemical performance was sufficient to justify NMR analysis including both ex-situ and in-situ experiments. It should, however, be noted that these results were obtained with relatively minimal optimization and there remains significant room for further improvement.

Given the rate of capacity decay it is likely that the sodium alginate binder is sufficient to keep the active material particles in initial contact with the carbon matrix. If there were a failure at this point the capacity would collapse to a fraction of its initial value within

the first few cycles. It is probable that the observed capacity fade is a consequence of the continually thickening SEI layer often mentioned in literature where volume expansion has been tied to the generation of unexposed active material which further reacts with the electrolyte.<sup>28,29</sup> This process can serve to electrically isolate particles from the conductive carbon matrix. While the binder can provide adhesion to the conductive matrix, it cannot prevent the accumulation of SEI products over numerous cycles. Approaches to address this might include changes to the battery chemistry including electrolyte additives or active particle modification.

Figure 5.2 shows the initial <sup>29</sup>Si MAS-NMR spectra collected for the lithiation of silicon monoxide anodes. The bottom spectrum of Figure 5.2 is that of the pristine SiO starting material, whereas the top two spectra include cycling to 77 and 330 mAh/g. For the pristine material there exist two domains that are associated with SiO<sub>2</sub> at about -105 ppm and the metallic silicon corresponding to the peak at about -70 ppm.<sup>15</sup> The T<sub>1</sub> values of pristine material were long and necessitated the use of relaxation delays significantly in excess of that used in all remaining experiments. Also evident in the pristine spectrum is a degree of peak intensity between the two end states. This likely represents a proportion of silicon species which are intermediate between metallic silicon and SiO<sub>2</sub>, as might be anticipated for a nominal SiO stoichiometry.<sup>30</sup> Initial lithiation shows the beginning development of three distinct regions which are more thoroughly described in Figures 5.3 through 5.5. These show two narrow peaks centered at about -70 and -20 ppm, coupled with a large broad peak which grows in relative intensity as a function of lithiation from -70 ppm initial up to approximately -20 ppm by the end of lithiation.

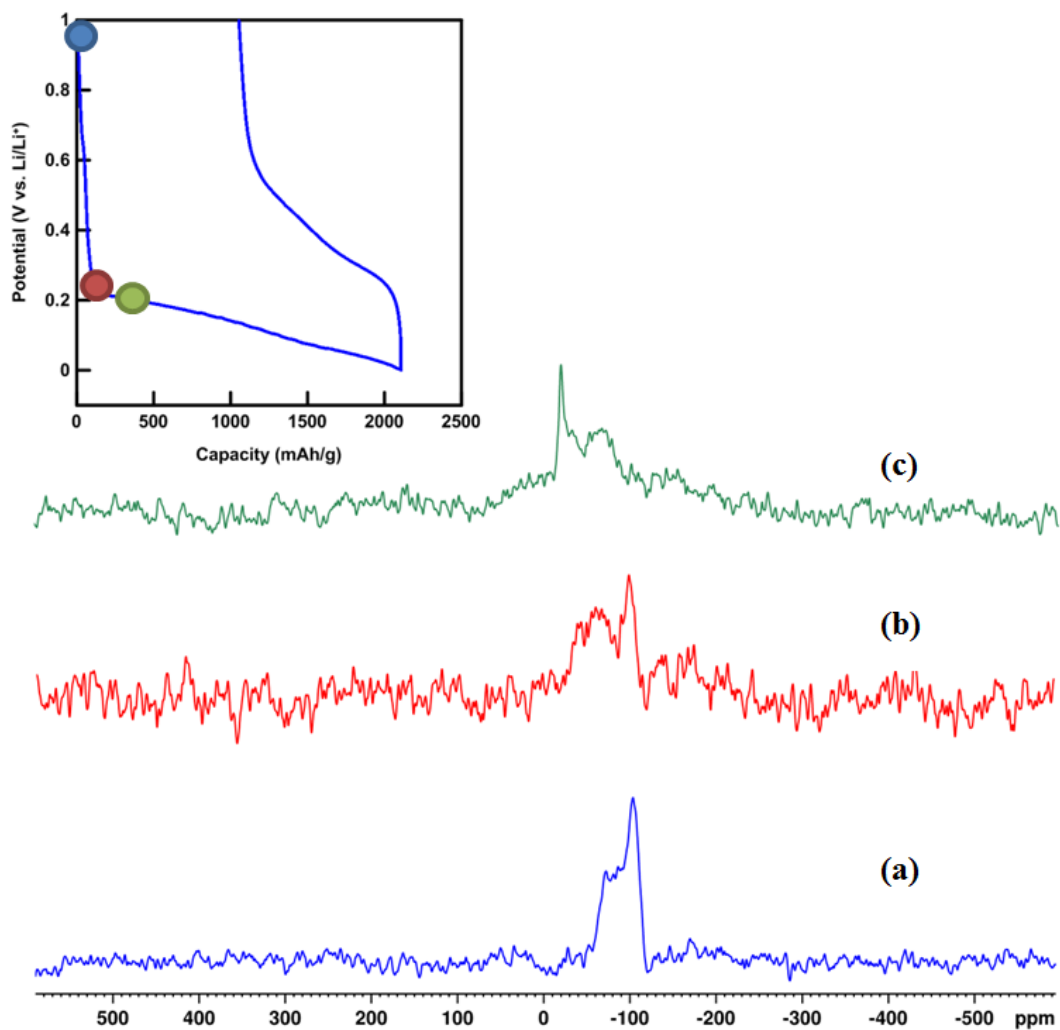


**Figure 5.2.** <sup>29</sup>Si MAS-NMR spectra of pristine silicon monoxide (a), silicon monoxide discharged to 77 mAh/g (b), and discharged to 330 mAh/g (c)

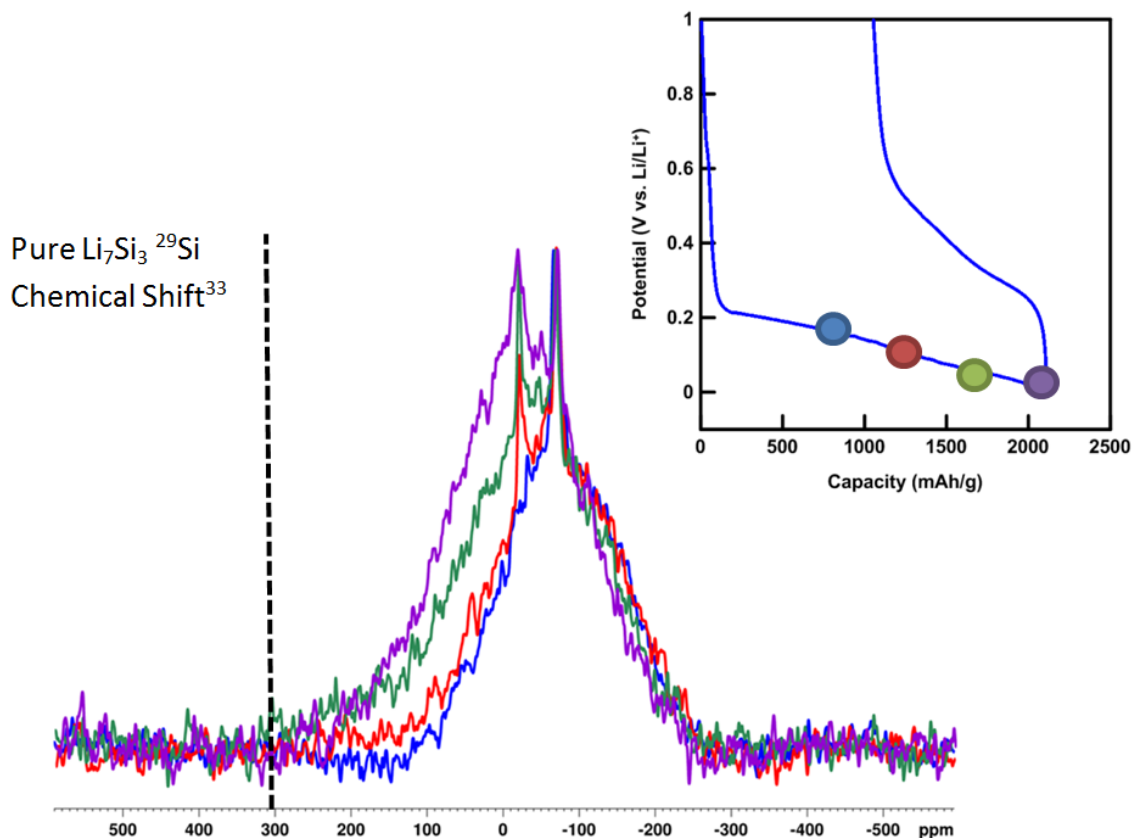


**Figure 5.3.**  $^{29}\text{Si}$  MAS-NMR spectra of further discharged silicon monoxide electrodes including 781 mAh/g (red), 1239 mAh/g (blue), 1755 mAh/g (green), and 2059 mAh/g (purple). The sample cycling curve serves as a legend to correlate the appropriate coloured spectra with their position on the cycling curve. The dashed line is presented in reference to work by Eckert et al.<sup>32</sup> where the isotropic  $^{29}\text{Si}$  chemical shift of a pure phase of  $\text{Li}_7\text{Si}_3$  is shown for reference

To put these chemical shift values in context it is instructive to consider the lithiation chemistry for both metallic silicon and silicon monoxide. In the former case lithiation proceeds through several stoichiometries beginning with  $\text{Li}_7\text{Si}_3$ , often ending with  $\text{Li}_{15}\text{Si}_4$  and includes several additional stoichiometries in-between.<sup>31,32</sup> Silicon monoxide

is suspected to lithiate similarly within its metallic silicon domains. However, a combination of  $\text{Li}_4\text{SiO}_4$  and  $\text{Li}_2\text{O}$  is expected within the silicon dioxide domains. Little precedent exists for  $^{29}\text{Si}$  chemical shift data for lithium silicides, however a publication by Eckert et. al.<sup>33</sup> is useful in this regard. They were successful in obtaining high quality  $^{29}\text{Si}$  MAS-NMR data of both  $\text{Li}_7\text{Si}_3$  and  $\text{Li}_{13}\text{Si}_4$  using a synthetic methodology as opposed to electrochemical lithiation. Chemical shift values of these stoichiometries were in excess of 300 ppm for both cases with linewidths of approximately 15 ppm.

The result obtained by Eckert et al. for metallic silicon contrasts significantly with those obtained for silicon monoxide. Some features can be readily explained such as the narrow resonance at -70 ppm which is consistent with a  $\text{Q}_0$  silicon bonding environment expected for the  $\text{Li}_4\text{SiO}_4$  irreversible lithiation product.<sup>15</sup> However, the two additional resonances at -20 and -70 ppm detailed in Figure 5.5 do not behave similarly to metallic silicon. It is clear from the intensity decrease relative to the  $\text{Li}_4\text{SiO}_4$  resonance during delithiation (Figure 5.4) that both are reversible lithium silicide species. However, there is clear lack of an extensive Knight shift where at no point throughout lithiation is this observed for either resonance, although a moderate positive chemical shift trend is observed for the broad resonance during this process. Furthermore, the majority of the silicon signal intensity is contained within the broad resonance with a linewidth in excess of 200 ppm. These results suggest that the lithiated metallic silicon domains within  $\text{SiO}$  have less metallic character than direct lithiation of pure silicon metal. This feature is a likely consequence of the silicon bonding environment described in figure 5.2 (a). In the pristine material, a nanoscale mixture of silicon species exists including the predominant

$Q_0$  and  $Q_4$  with intermediate  $Q_1$  through  $Q_3$  states.<sup>30</sup> Lithium silicides produced in this environment are finely interspersed and do not agglomerate into larger structures where a more significant Knight shift could arise. This structure might explain the ability of lithium silicate to constrain volume expansion in such small domains and yield the associated capacity retention.

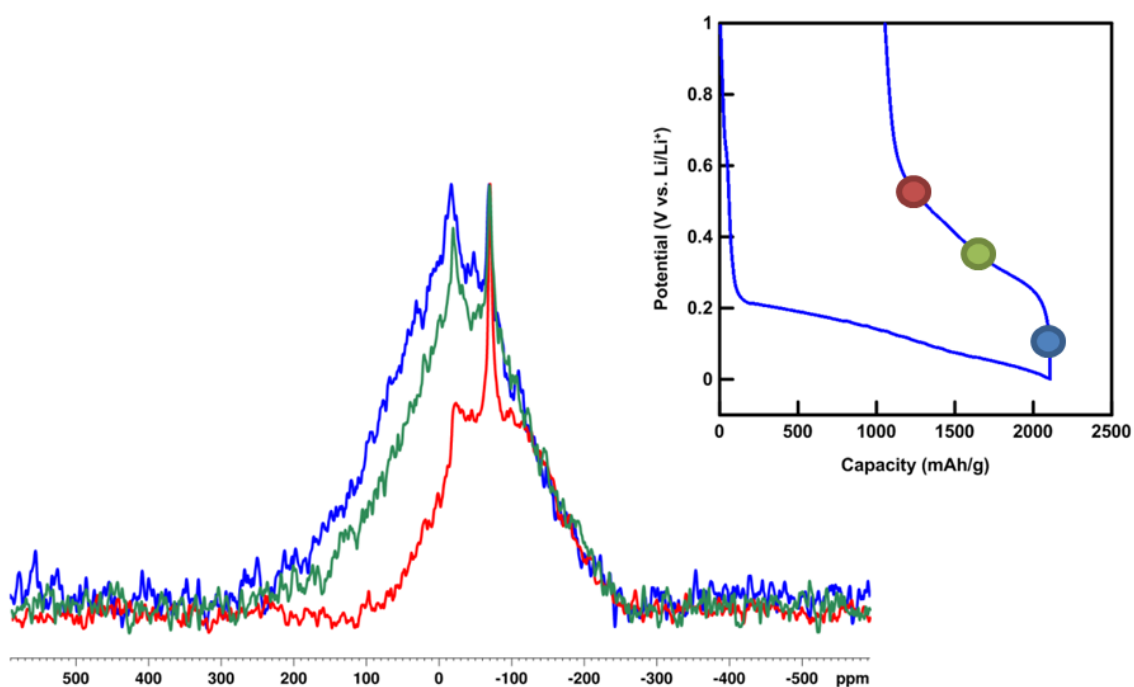


**Figure 5.4.**  $^{29}\text{Si}$  MAS-NMR spectra of charged silicon monoxide anodes from 2230 mAh/g to near the end of charge at approximately 1000 mAh/g showing the reversible capacity associated with the broad resonance and the peak at -20 ppm.

Width, chemical shift trend, and relative intensity increase as a function of lithiation (Figure 5.5) for the broad resonance are consistent with an interpretation as a collection of amorphous lithium silicides. The narrow peak at -20 ppm is, however, more difficult to unambiguously identify, though the width and reversibility suggests a small amount of a crystalline lithium silicide phase. Interestingly, it was first observed in Figure 5.2 (c) at 330 mAh/g of lithiation. Also, the chemical shift of the narrow resonance corresponds with that of the amorphous lithium silicide in its most lithiated state. Finally its relative peak area with respect to  $\text{Li}_4\text{SiO}_4$  remains constant after 1281 mAh/g of lithiation capacity and higher. This is in opposition to the continuously increasing trend for the amorphous lithium silicide resonance. These observations both support and detract from the phase being associated with crystalline  $\text{Li}_{15}\text{Si}_4$  with further experiments required to conclusively identify the resonance.

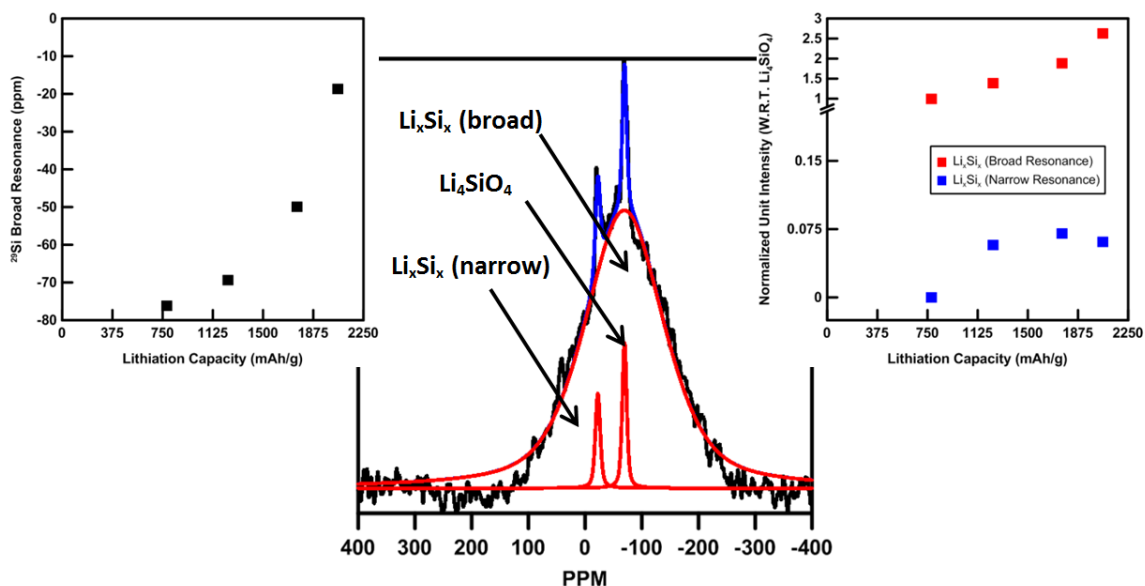


**Figure 5.5.** The central figure shows a deconvolution of  $^{29}\text{Si}$  MAS-NMR spectrum for the species lithiated to 1239 mAh/g capacity. The spectrum depicts a narrow  $\text{Li}_4\text{SiO}_4$  peak (-70 ppm) as well as lithium silicide products (narrow peak at -20 ppm, broad peak at -70 ppm) associated with the other two resonances. The left figure shows how the chemical shift of the broad lithium silicide resonance changes as a function of lithiation. On the right figure the integral area of the lithium silicide peaks is shown as a function of the lithiation capacity, normalized to the intensity of the  $\text{Li}_4\text{SiO}_4$  resonance.

The ex-situ  $^{29}\text{Si}$  MAS-NMR measurements were made practical through the use of a high field 850 MHz spectrometer coupled with the high active material loading of the cellulose based SiO anodes. To complement these measurements, in-situ  $^7\text{Li}$  measurements were conducted on the same system to further exemplify its utility. A schematic representation of the in-situ cell is depicted in Figure 5.6.

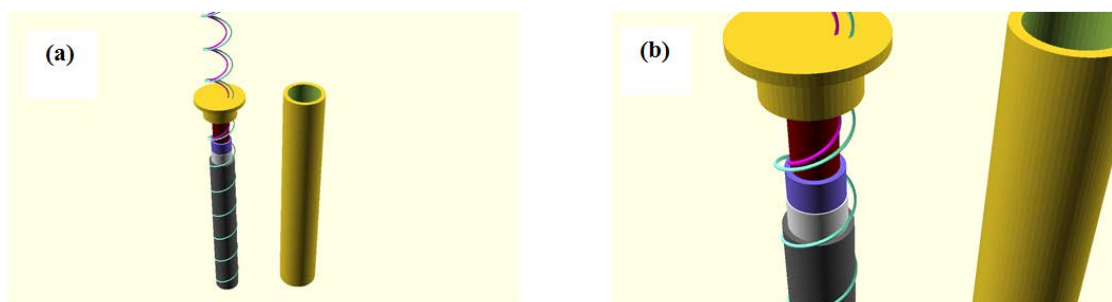


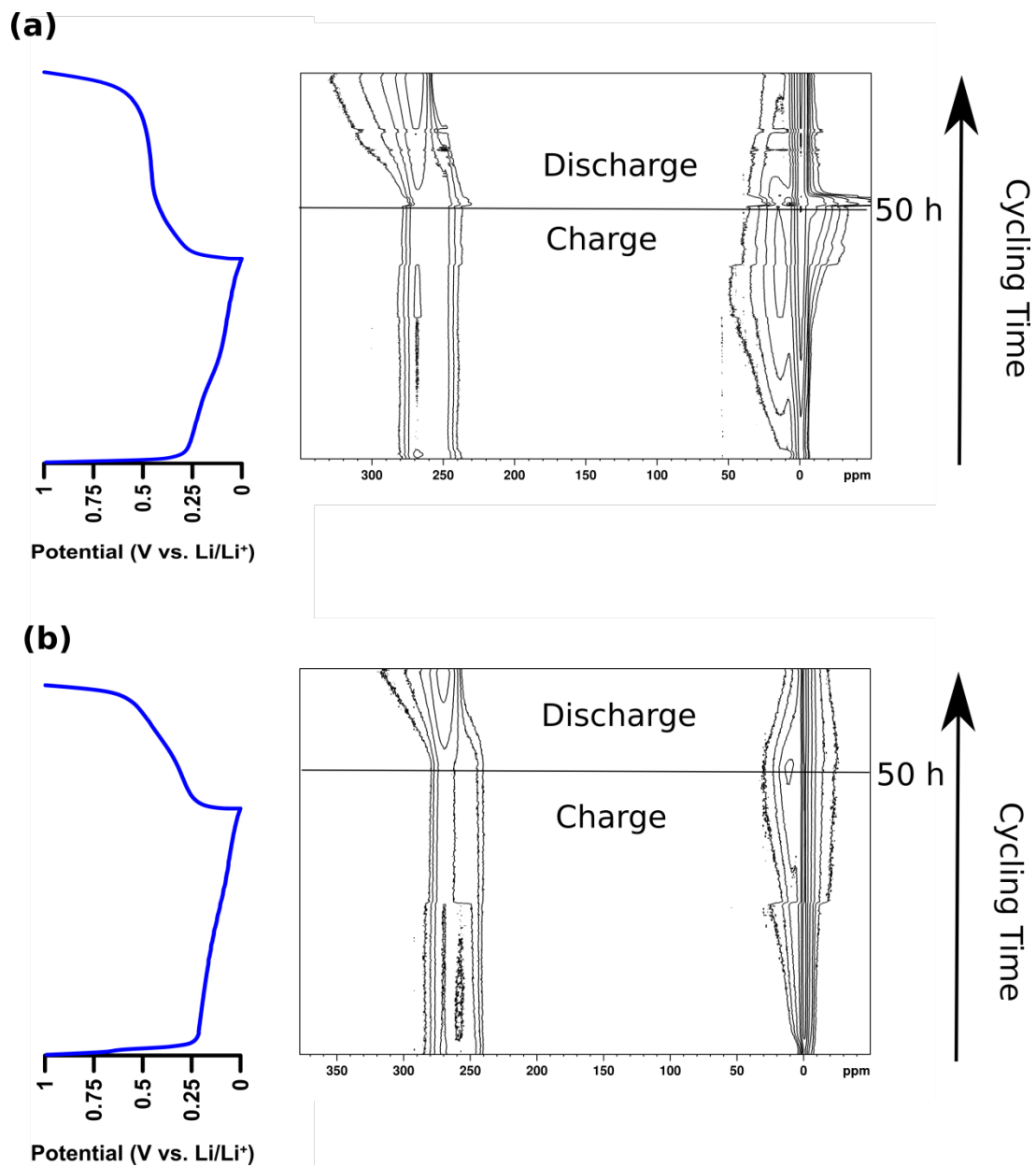
**Figure 5.6.** Schematic of in-situ cell configuration showing an overview (a) and a closeup (b) of the cell design. Elements include the anode and cathode wires (magenta and cyan spirals respectively), plastic core (red cylinder) and the lithium metal, separator, and cellulosic substrate anode (represented by the purple, white and gray cylinders respectively). These are all enclosed in a plastic tube with a silicon rubber septum serving to isolate the battery chemistry from the environment while allowing electrical connections.

The primary goal of the design is to maximize the quantity of active material being probed while simultaneously limiting RF shielding effects from the metallic components. The cylindrical design maximizes the amount of active material whereas a solenoid coil improves sensitivity performance. Use of a solid copper current collector would be unsuitable for the design as the RF skin depth penetration at a 77.7 MHz  $^7\text{Li}$  resonance spectrometer is approximately  $7.5 \mu\text{m}$ .<sup>34</sup> This would severely limit RF penetration to the active material and result in reduced signal intensity.

Use of a cellulosic substrate allows greater RF penetration and thus permits the use of the aforementioned cell geometry. Coupled with the increased sample loading inherent to how the electrodes were prepared, these features enabled relatively rapid data acquisition. It was possible to obtain respectable S/N ratios within 2 minutes of acquisition time and

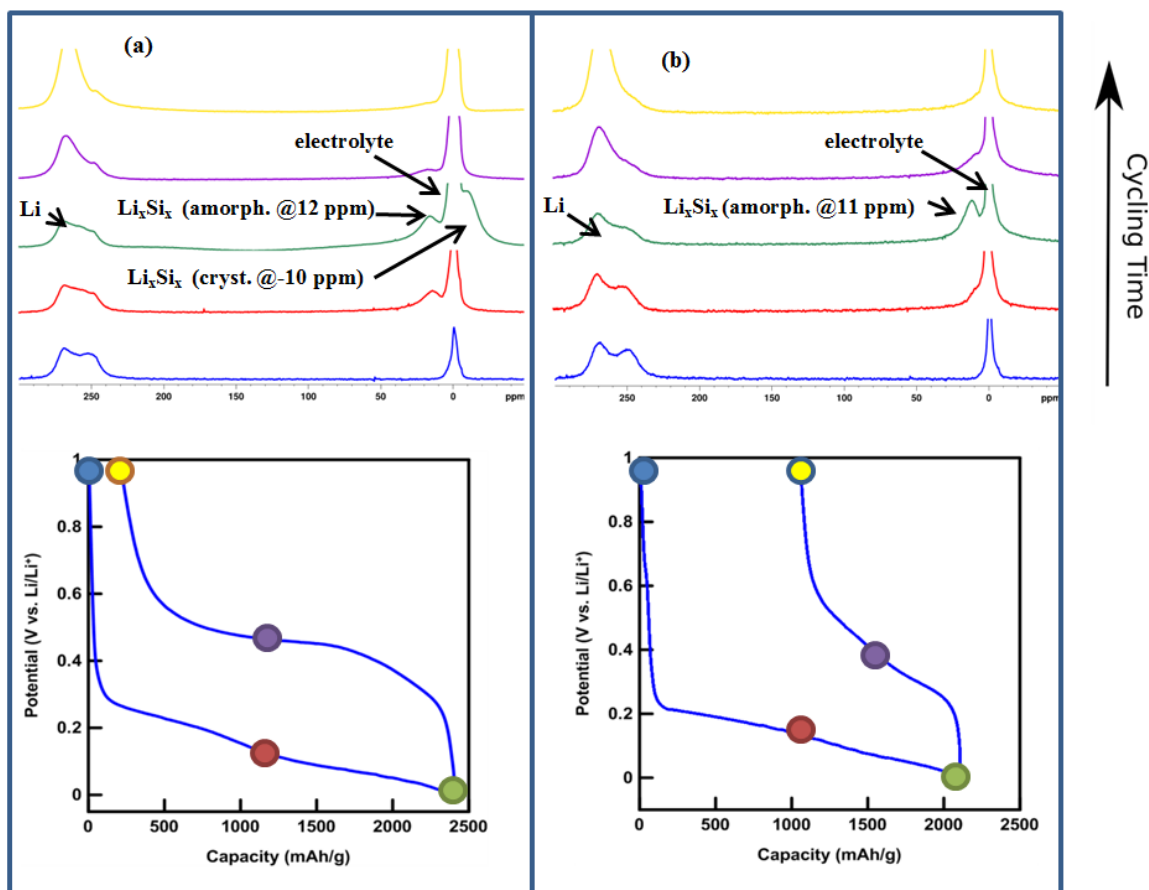
appropriately applied line broadening. Alternatively, as the cycling rate was the greater limiting factor, acquisition times on the order of 10-20 minutes were more typical but allowed for the application of limited line broadening.

Figure 5.7 depicts the overall change in chemical shift across one full cycle for both silicon metal and silicon monoxide anodes. This overall picture shows an apparent similarity in initial cycling behavior as the lithium chemical shift increases upon lithiation. However, upon nearing the end of lithiation their behaviour begins to deviate. The silicon metal spectrum shows the development of a second peak at negative chemical shift values which corresponds to previous in-situ studies suggesting the formation of a crystalline  $\text{Li}_{15}\text{Si}_4$  phase.<sup>35,36</sup> In contrast, the formation of this same peak is not observed for the SiO anode. The amorphous to crystalline transition towards the end of lithiation has been implicated exacerbating capacity fade.<sup>7</sup> Fortunately, the absence of this signal during the in-situ measurements suggests no such large scale transition and bodes well for the use of SiO as an anode material.



**Figure 5.7.** Comparison of  $^7\text{Li}$  in-situ spectra detailing change in lithium chemical shift across a full discharge/charge cycle for cellulose based silicon metal anodes (a) and silicon monoxide (b). In-situ spectra were acquired at an approximate cycling rate of C/50 and include coin-cell cycling curves on the left for reference.

Figure 5.8 provides a more detailed description of the lithiation in both systems by showing snapshots of the beginning, middle and end of discharge and charge respectively. Besides the absence of the resonance at -10 ppm the chemical shift behaviour of the initial lithiation peak differs. For silicon metal the average lithium silicide chemical shift appears at approximately 12 ppm and remains there until the appearance of the crystalline phase at -10 ppm. Silicon monoxide by contrast showed a chemical shift trend ranging from 4 to 11 ppm with increasing lithium content. Additionally, the appearance of a peak at -10 ppm was not observed. This behaviour is consistent with previously performed ex-situ  $^7\text{Li}$  NMR of these materials.<sup>14,15</sup> Immediately clear is that the electronic environments of lithium in the associated lithium silicide phases are not equivalent between the two anode materials. This might indicate that the expected metallic silicon domains are interspersed finely enough to result in a different lithium chemical shift trend. An intriguing additional feature of the in-situ spectra is the evolution of the lithium metal resonances centered at 250 and 270 ppm. These result from the orientation dependence of the lithium metal chemical shift with respect to the magnetic field. Lithium metal parallel with the field tends towards higher chemical shift and the opposite trend dominates in a perpendicular orientation.<sup>37</sup> Because of the cylindrical distribution of lithium metal around the plastic core there are equivalent distributions of lithium aligned parallel and perpendicular to the magnetic field axis. The end result is the approximately equal distribution of these resonances with a continuum or orientations in-between.



**Figure 5.8.** Comparison of  $^7\text{Li}$  in-situ snapshots detailing change in lithium chemical shift at the beginning (blue) middle (red) and end (green) of charge for cellulose based silicon metal anodes (a) and silicon monoxide (b)

Through the first discharge the intensity of the lithium metal resonance changes only marginally. This is a consequence of its low RF permeability restricting signals to the uppermost layer. Since the surface area is only decreasing slightly at this stage, large changes to the resonance are not expected. However, charging involves lithium re-deposition in a geometry less dense than the initial bulk metallic lithium. The formation

of lithium dendrites causes a drastic increase in the lithium metal signal intensity above the initial resonance intensity and is a direct result of the surface area increase.

#### **5.4 - Conclusion**

This work demonstrates the utility of using porous cellulosic substrates in the context of lithium ion battery characterization via NMR. Long term cycling data demonstrated the reasonable capacity retention for SiO anodes despite the high loadings employed. The large quantity of active material was important in enabling  $^{29}\text{Si}$  MAS-NMR of the cycled anode materials as a function of charge state. These spectra reaffirmed certain aspects of the silicon monoxide electrochemistry including the presence of a lithiated  $\text{Li}_4\text{SiO}_4$  irreversible phase in combination with a broad resonance corresponding to formation of lithium silicides. Importantly, there was also the appearance of a narrow resonance which we suggest may be the consequence of a crystalline lithium silicide phase. This resonance appeared even at the early stages of lithiation and never constituted a large component of the electrode. In contrast, the in-situ  $^7\text{Li}$  NMR spectra showed substantial amounts of crystalline lithium silicide during lithiation of metallic silicon. Confirmation of whether the narrow peak seen in the  $^{29}\text{Si}$  MAS-NMR data is the much discussed crystalline  $\text{Li}_{15}\text{Si}_4$  will be the subject of further research.

Additionally, the research presented here has proven the utility of a novel prototype design for the in-situ NMR characterization of lithium ion batteries. Having confirmed the suitability of cellulosic substrates in at least the anode context, the increased filling factor and RF permeability of the design lend themselves well to future experiments.

With further improvements it is possible to extend this methodology to other materials and potentially to other nuclei (e.g.  $^{29}\text{Si}$ ).

## 5.5 - References

- (1) Park, C.-M.; Kim, J.-H.; Kim, H.; Sohn, H.-J. Li-Alloy Based Anode Materials for Li Secondary Batteries. *Chem. Soc. Rev.* **2010**, *39* (8), 3115–3141.
- (2) Zhang, W.-J. A Review of the Electrochemical Performance of Alloy Anodes for Lithium-Ion Batteries. *J. Power Sources* **2011**, *196* (1), 13–24.
- (3) Beattie, S. D.; Larcher, D.; Morcrette, M.; Simon, B.; Tarascon, J.-M. Si Electrodes for Li-Ion Batteries—A New Way to Look at an Old Problem. *J. Electrochem. Soc.* **2008**, *155* (2), A158–A163.
- (4) Etacheri, V.; Haik, O.; Goffer, Y.; Roberts, G. A.; Stefan, I. C.; Fasching, R.; Aurbach, D. Effect of Fluoroethylene Carbonate (FEC) on the Performance and Surface Chemistry of Si-Nanowire Li-Ion Battery Anodes. *Langmuir* **2012**, *28* (1), 965–976.
- (5) Liu, N.; Wu, H.; McDowell, M. T.; Yao, Y.; Wang, C.; Cui, Y. A Yolk-Shell Design for Stabilized and Scalable Li-Ion Battery Alloy Anodes. *Nano Lett.* **2012**, *12* (6), 3315–3321.
- (6) Kasavajjula, U.; Wang, C.; Appleby, A. J. Nano- and Bulk-Silicon-Based Insertion Anodes for Lithium-Ion Secondary Cells. *J. Power Sources* **2007**, *163* (2), 1003–1039.

- (7) Szczech, J. R.; Jin, S. Nanostructured Silicon for High Capacity Lithium Battery Anodes. *Energy Environ. Sci.* **2010**, *4* (1), 56–72.
- (8) Wu, H.; Cui, Y. Designing Nanostructured Si Anodes for High Energy Lithium Ion Batteries. *Nano Today* **2012**, *7* (5), 414–429.
- (9) Key, B.; Bhattacharyya, R.; Morcrette, M.; Seznéc, V.; Tarascon, J.-M.; Grey, C. P. Real-Time NMR Investigations of Structural Changes in Silicon Electrodes for Lithium-Ion Batteries. *J. Am. Chem. Soc.* **2009**, *131* (26), 9239–9249.
- (10) Obrovac, M. N.; Christensen, L. Structural Changes in Silicon Anodes during Lithium Insertion/Extraction. *Electrochem. Solid-State Lett.* **2004**, *7* (5), A93–A96.
- (11) Hatchard, T. D.; Dahn, J. R. In Situ XRD and Electrochemical Study of the Reaction of Lithium with Amorphous Silicon. *J. Electrochem. Soc.* **2004**, *151* (6), A838–A842.
- (12) Miyachi, M.; Yamamoto, H.; Kawai, H.; Ohta, T.; Shirakata, M. Analysis of SiO Anodes for Lithium-Ion Batteries. *J. Electrochem. Soc.* **2005**, *152* (10), A2089–A2091.
- (13) Hwa, Y.; Park, C.-M.; Sohn, H.-J. Modified SiO as a High Performance Anode for Li-Ion Batteries. *J. Power Sources* **2013**, *222*, 129–134.
- (14) Kim, J.-H.; Park, C.-M.; Kim, H.; Kim, Y.-J.; Sohn, H.-J. Electrochemical Behavior of SiO Anode for Li Secondary Batteries. *J. Electroanal. Chem.* **2011**, *661* (1), 245–249.

- (15) Kim, T.; Park, S.; Oh, S. M. Solid-State NMR and Electrochemical Dilatometry Study on Li + Uptake/Extraction Mechanism in SiO Electrode. *J. Electrochem. Soc.* **2007**, *154* (12), A1112–A1117.
- (16) Nguyen, T. H.; Fraiwan, A.; Choi, S. Paper-Based Batteries: A Review. *Biosens. Bioelectron.* **2014**, *54*, 640–649.
- (17) Jabbour, L.; Bongiovanni, R.; Chaussy, D.; Gerbaldi, C.; Beneventi, D. Cellulose-Based Li-Ion Batteries: A Review. *Cellulose* **2013**, *20* (4), 1523–1545.
- (18) Li, J.; Lewis, R. B.; Dahn, J. R. Sodium Carboxymethyl Cellulose A Potential Binder for Si Negative Electrodes for Li-Ion Batteries. *Electrochem. Solid-State Lett.* **2007**, *10* (2), A17–A20.
- (19) Zhang, J.; Yue, L.; Kong, Q.; Liu, Z.; Zhou, X.; Zhang, C.; Xu, Q.; Zhang, B.; Ding, G.; Qin, B.; et al. Sustainable, Heat-Resistant and Flame-Retardant Cellulose-Based Composite Separator for High-Performance Lithium Ion Battery. *Sci. Rep.* **2014**, *4*.
- (20) Song, Z.; Ma, T.; Tang, R.; Cheng, Q.; Wang, X.; Krishnaraju, D.; Panat, R.; Chan, C. K.; Yu, H.; Jiang, H. Origami Lithium-Ion Batteries. *Nat. Commun.* **2014**, *5*, 3140.
- (21) Cui, L.-F.; Yang, Y.; Hsu, C.-M.; Cui, Y. Carbon–Silicon Core–Shell Nanowires as High Capacity Electrode for Lithium Ion Batteries. *Nano Lett.* **2009**, *9* (9), 3370–3374.

- (22) Zhao, H.; Fu, Y.; Ling, M.; Jia, Z.; Song, X.; Chen, Z.; Lu, J.; Amine, K.; Liu, G. Conductive Polymer Binder-Enabled SiO–SnxCoyCz Anode for High-Energy Lithium-Ion Batteries. *ACS Appl. Mater. Interfaces* **2016**, *8* (21), 13373–13377.
- (23) Hoult, D. I.; Richards, R. E. The Signal-to-Noise Ratio of the Nuclear Magnetic Resonance Experiment. *J. Magn. Reson.* 1969 **1976**, *24* (1), 71–85.
- (24) Letellier, M.; Chevallier, F.; Clinard, C.; Frackowiak, E.; Rouzaud, J.-N.; Béguin, F.; Morcrette, M.; Tarascon, J.-M. The First in Situ <sup>7</sup>Li Nuclear Magnetic Resonance Study of Lithium Insertion in Hard-Carbon Anode Materials for Li-Ion Batteries. *J. Chem. Phys.* **2003**, *118* (13), 6038–6045.
- (25) Pecher, O.; Bayley, P. M.; Liu, H.; Liu, Z.; Trease, N. M.; Grey, C. P. Automatic Tuning Matching Cyclers (ATMC) in Situ NMR Spectroscopy as a Novel Approach for Real-Time Investigations of Li- and Na-Ion Batteries. *J. Magn. Reson.* **2016**, *265*, 200–209.
- (26) Lu, Z.; Liu, N.; Lee, H.-W.; Zhao, J.; Li, W.; Li, Y.; Cui, Y. Nonfilling Carbon Coating of Porous Silicon Micrometer-Sized Particles for High-Performance Lithium Battery Anodes. *ACS Nano* **2015**, *9* (3), 2540–2547.
- (27) Jung, S. C.; Kim, H.-J.; Kim, J.-H.; Han, Y.-K. Atomic-Level Understanding toward a High-Capacity and High-Power Silicon Oxide (SiO) Material. *J. Phys. Chem. C* **2016**, *120* (2), 886–892.

- (28) Zhang, Q.; Xiao, X.; Zhou, W.; Cheng, Y.-T.; Verbrugge, M. W. Toward High Cycle Efficiency of Silicon-Based Negative Electrodes by Designing the Solid Electrolyte Interphase. *Adv. Energy Mater.* **2015**, *5* (5), n/a-n/a.
- (29) Li, J.; Dudney, N. J.; Nanda, J.; Liang, C. Artificial Solid Electrolyte Interphase To Address the Electrochemical Degradation of Silicon Electrodes. *ACS Appl. Mater. Interfaces* **2014**, *6* (13), 10083–10088.
- (30) Hirata, A.; Kohara, S.; Asada, T.; Arao, M.; Yogi, C.; Imai, H.; Tan, Y.; Fujita, T.; Chen, M. Atomic-Scale Disproportionation in Amorphous Silicon Monoxide. *Nat. Commun.* **2016**, *7*, 11591.
- (31) Okamoto, H. The Li-Si (Lithium-Silicon) System. *Bull. Alloy Phase Diagr.* **1990**, *11* (3), 306–312.
- (32) Key, B.; Morcrette, M.; Tarascon, J.-M.; Grey, C. P. Pair Distribution Function Analysis and Solid State NMR Studies of Silicon Electrodes for Lithium Ion Batteries: Understanding the (De)lithiation Mechanisms. *J. Am. Chem. Soc.* **2011**, *133* (3), 503–512.
- (33) Dupke, S.; Langer, T.; Pöttgen, R.; Winter, M.; Passerini, S.; Eckert, H. Structural Characterization of the Lithium Silicides Li<sub>15</sub>Si<sub>4</sub>, Li<sub>13</sub>Si<sub>4</sub>, and Li<sub>7</sub>Si<sub>3</sub> Using Solid State NMR. *Phys. Chem. Chem. Phys.* **2012**, *14* (18), 6496–6508.
- (34) Wheeler, H. A. Formulas for the Skin Effect. *Proc. IRE* **1942**, *30* (9), 412–424.

- (35) Key, B.; Bhattacharyya, R.; Morcrette, M.; Seznéc, V.; Tarascon, J.-M.; Grey, C. P. Real-Time NMR Investigations of Structural Changes in Silicon Electrodes for Lithium-Ion Batteries. *J. Am. Chem. Soc.* **2009**, *131* (26), 9239–9249.
- (36) Gu, M.; Wang, Z.; Connell, J. G.; Perea, D. E.; Lauhon, L. J.; Gao, F.; Wang, C. Electronic Origin for the Phase Transition from Amorphous  $\text{Li}_x\text{Si}$  to Crystalline  $\text{Li}_{15}\text{Si}_4$ . *ACS Nano* **2013**, *7* (7), 6303–6309.
- (37) Trease, N. M.; Zhou, L.; Chang, H. J.; Zhu, B. Y.; Grey, C. P. In Situ NMR of Lithium Ion Batteries: Bulk Susceptibility Effects and Practical Considerations. *Solid State Nucl. Magn. Reson.* **2012**, *42*, 62–70.



## **Chapter 6: Rotobattery**

Results outlined here detail current progress in developing an in-situ lithium ion battery capable of being characterized by MAS-NMR. Details included cell construction, initial spin testing and electrochemistry, MAS-NMR preliminary results, and discussion of wireless charge/discharge mechanisms. In particular, the MAS-NMR of a  $\text{LiCoO}_2$ /Graphite full cell configuration supported the feasibility of further rotobattery development.

This report was prepared by the authors Allen D. Pauric and Gillian R. Goward. Data collection, initial analyses, and initial draft preparation were conducted by Allen D. Pauric. Final analyses and manuscript edits included contributions from Gillian R. Goward. Submission to a peer-reviewed journal is anticipated upon completion of additional supporting experiments.

### **6.1 - Introduction**

As Chapter 5 has illustrated the application of static in-situ NMR to the characterization of LIB materials can lend valuable operational insight. However, a significant drawback of a static configuration is the inability to perform magic angle spinning. The rotation of an in-situ cell about the magic angle would enable substantial increases in spectral resolution and broaden the scope of the methodology. It would have application to all aspects of LIB characterization. To illustrate the potential utility it is instructive to consider the well characterized  $\text{LiCoO}_2$  cathode material.

From an NMR perspective this material exhibits exemplary behaviour as shown by Delmas et al.<sup>1</sup> In their publication they report the  $^7\text{Li}$  chemical shift of a fully discharged  $\text{LiCoO}_2$  cathode centered at about 0 ppm with a linewidth on the order of several ppm. As lithiation progresses a second resonance appears around 50 ppm characteristic to the  $\text{Li}_{0.75}\text{CoO}_2$  phase. In the fully discharged state the original 0 ppm resonance completely disappears and is fully replaced by the new signal which shifts to  $\approx 100$  ppm. Many commonly used LIB cathode materials are paramagnetic and result in linewidths of over 100 ppm as caused by  $^7\text{Li}$  nuclei interacting with the unpaired electron spin. The discharged form of  $\text{LiCoO}_2$ , however, includes  $\text{Co}^{3+}$  which is diamagnetic and thus allows for the narrow linewidths. Further to this, as  $\text{Co}^{3+}$  is oxidized to  $\text{Co}^{4+}$  the resulting phase possesses greater metallic character. Any lithium cations localized to  $\text{Co}^{4+}$  are broadened such that they become unobservable in a typical experiment. However, those that remained localized about  $\text{Co}^{3+}$  become Knight shifted. This shift arises from the additional effective magnetic field strength imposed by the conduction electrons, yielding the observed positive chemical shift change.

Such NMR studies of LIB electrodes are typically performed via the ex-situ processing of cycled coin cells. For well-behaved materials like  $\text{LiCoO}_2$  these measurements typically require under an hour of measurement time and often merely minutes. The limiting step is the assembly, disassembly, and rotor preparation prerequisite to the measurements. An in-situ experiment would allow for continuous monitoring, enabling a complete description of the chemical environment as a function of lithiation state, as opposed to the snapshots more typical of ex-situ experiments.

Furthermore, only a single in-situ experiment would need to be constructed, significantly reducing the experimental effort required to obtain the desired spectra.

Unfortunately, static in-situ experiments would not compensate for the line broadening behaviour of NMR interactions like CSA. This can often be significant enough so as to obscure site resolution for even a well-resolved material like  $\text{LiCoO}_2$ . Thus the ability to perform MAS-NMR on an in-situ LIB experiment would improve the spectral resolution while simultaneously retaining the practical implications of in-situ measurements. Another benefit includes the maintenance of the electrode in a pristine state while under applied potential, addressing both the contamination issues of ex-situ experiments and allowing the observation of any potential metastable states which might only exist during active lithiation/delithation.

Potential MAS-NMR in-situ experiments are not limited to cathodes or even to  $^7\text{Li}$ . Many other active nuclei including  $^{13}\text{C}$ ,  $^{19}\text{F}$ ,  $^{29}\text{Si}$ , and  $^{31}\text{P}$  have been utilized in ex-situ MAS-NMR studies of relevant materials previously.<sup>2-5</sup> An in-situ capability would incorporate all the advantages mentioned and apply them towards SEI layer characterization, anode analyses, binder degradation studies, and many other aspects of LIB operation.

While there is significant motivation for designing an in-situ MAS-NMR experiment, a practical implementation is particularly challenging due to a number of complicating factors. For instance, the inclusion of metallic components is more problematic than in the static in-situ geometry discussed in Chapter 5. Not only is RF penetration still a concern, but even small amounts of highly conductive metal can support eddy currents in

response to being rapidly rotated in the strong magnetic field.<sup>6</sup> The result is an auxiliary magnetic field which functions to oppose further rotation, often significantly hindering MAS experiments. Another challenge is the incorporation of a charging mechanism. Specifically the rapid rotation eliminates the possibility of a wired charging mechanism, thus necessitating the implementation of a wireless solution. Additional concerns include rotational stability, cycling performance, and ease of construction.

Described here is a discussion of the steps being taken to address these issues. It incorporates features of the static in-situ experiments, 3D printing, and other tools to construct what will subsequently be referred to as a “rotobattery.”

## **6.2 - Objectives**

The rotobattery project can be divided into several distinct sections. Firstly, the structural components and active materials of the rotobattery are to be successfully rotated in 4mm (3mm internal diameter) zirconia rotor at a target rotational speed of 10 kHz. Second, the assembly will be proven as electrochemical cyclable under static conditions. Third, a charged version of the assembly will be controllably discharged via an adequate choice of resistor while sustaining rotation at 10 kHz. And finally, a full assembled rotobattery is to be constructed including a photovoltaic element with static and dynamic testing. It is important to mention, however, that the steps thus described are to some extent interlinked and accommodations will have to be made earlier to address the requirements of later steps.

### 6.3 - Structural Considerations

A principal design premise for the rotobattery is minimization of highly conductive metallic components given the implications for eddy current reduction and improved RF penetration. The developments in cellulosic electrodes described in chapter 5 serve this purpose well and have been incorporated into the design. Unfortunately, this also restricts the use of metallic lithium. Nevertheless, use of air stabilized lithium particles<sup>7</sup> or exceptionally thin lithium foil may enable the issue to be circumvented. To eliminate this additional consideration, the present study utilizes lithium insertion type anodes including graphite and lithium titanium oxide (LTO).

While it is possible to eliminate metallic current collector sheets, an electrical connection from the cellulosic electrode to the electrical source is still required. Thin metallic wire would serve this purpose well, however rotation at 10 kHz of a 1 cm long, 0.250 mm diameter copper wire segment in a 4 mm rotor was sufficient to prevent rotation beyond 1 kHz. Fortunately, titanium wire can serve as an alternative. It is approximately 40 times less conductive than copper (Table 6.1) and identical testing of a 0.250 mm diameter titanium wire achieved spinning rates beyond 10 kHz. Despite the reduced conductivity inherent to titanium, a point-to-point resistance measurement showed that the majority of the resistance originated from the electrode material rather than the titanium itself. This implies that the electrical performance of the cell is not significantly hindered by the replacement of copper and aluminum with titanium.

Metals	Conductivity (S/cm)
Copper	$6.00 \times 10^5$
Aluminum	$3.77 \times 10^5$
Lithium	$1.17 \times 10^5$
Titanium	$0.18 \times 10^5$

**Table 6.1.** Conductivities of selected metals relevant to rotobattery construction (Conductivity values measured at the Canadian Institute for Non-Destructive Testing)

A cylindrical design has numerous benefits including an increase in the amount of active material. To illustrate some of the other benefits it is instructive to consider the role of the structural support as depicted in Figure 6.1.

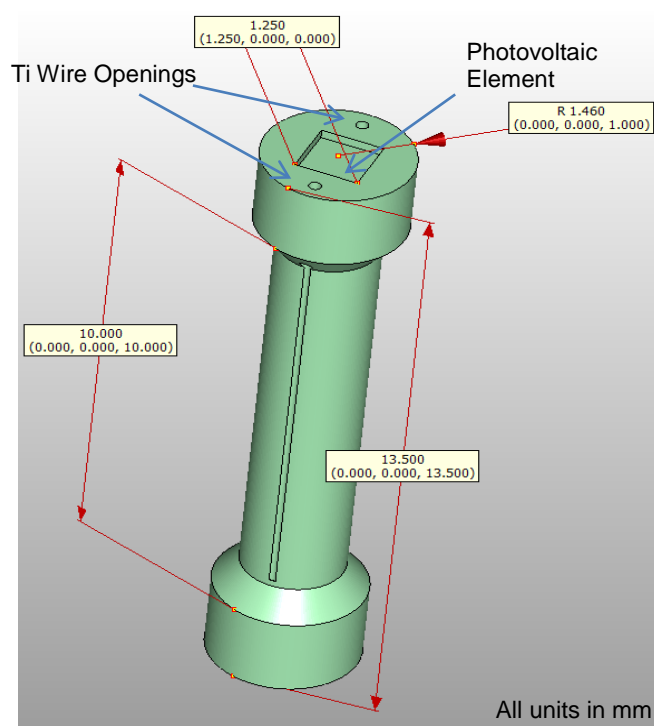


**Figure 6.1.** Schematic depiction of rotobattery support structure

A primary function of the support structure is to serve as a scaffold upon which all the constituent battery components can be wrapped. The typical order of assembly involves titanium wire, followed by inner electrode, separator, outer electrode, and titanium wire, not dissimilar from the “jelly-roll” design of many commercial batteries.<sup>8</sup> Making the outer electrode the material of interest is advantageous as the coil-electrode distance is minimized. The use of cellulose based electrodes and metallic wire facilitates RF penetration. Also, placing the active components towards the center maximizes RF field homogeneity and thus improves signal resolution.

Other features include a mechanism to mount and isolate the desired photovoltaic element or circuit from the battery chemistry. The support structure is utilized as a removable insert where the air compatible components can be assembled separately (e.g. outside the glovebox). Add to this the role in balancing the rotor during rotation and the importance of an appropriate support structure becomes clear.

3D printing has proven instrumental in iterating over support structure prototypes. The model shown above was constructed using the open source software OpenSCAD<sup>9</sup> (source code available in appendix) which facilitates parametric design to precise dimensions. It is however important to note the practical limitations in the physical resolution achievable. Fused deposition printing<sup>10</sup> is the most common type of 3D printing used for consumer grade devices. It operates through an additive process where an object is produced via melting and extrusion of thermoplastics in a layered fashion. While relatively inexpensive, this technology typically achieves up to 100 micron resolution and was found to be insufficient for the present purpose. This was however

rectified upon switching to the use of stereolithography (SLA). Instead of melting a thermoplastic, SLA involves lowering a build platform into a tank of UV curable resin. Each layer is produced via the precise application of UV light initiating photopolymerization of the resin. Upon subsequent platform lowering to build additional layers the result is an achievable build resolution of approximately 25 microns with high reproducibility. While the build quality thus obtained through SLA was sufficient, there was still the issue of chemical compatibility. The combination of both highly oxidative and reductive conditions and even simply solvent incompatibilities might render typical UV-curable resins unsuitable. Nevertheless, even if an incompatibility is confirmed, the information thus gained could be applied towards materials with proven chemical stability. In the LIB context, such materials include polytetrafluoroethylene (PTFE) or polyetheretherketone (PEEK). Once a design is finalized the finished structural support could be produced in these materials via either 3D printing or traditional subtractive manufacturing.

#### **6.4 - Cell Assembly**

The current assembly procedure for the battery components has been developed in an attempt to optimize both spin stability and electrochemical performance. It is important to note the preliminary nature of the procedure described where many of the details are subject to change. With this caveat under consideration, the current first step involves laying down the titanium wire which connects the anode to the external circuit. As current iterations of the structural support have not been tuned sufficiently for the printed

hole to be of the correct dimensions, what openings did exist was carefully excavated to yield slits (see Figure 1). To limit the amount of metal utilized, small diameter wire and a single linear strip of wire are desirable. Nevertheless, for ease of construction in the prototyping phase, the planned linear section of 0.125 mm titanium wire was replaced with a spiral of 0.250 mm titanium wire. This was easier to manipulate and relatively inexpensive allowing for more flexibility in the experimentation.

Upon coiling the titanium wire about the support, a section of graphite on a cellulosic substrate was wrapped about the anode wire section. This anode material was constructed in a similar fashion to the anodes described the previous chapter, including 92.5 wt% graphite and 7.5wt% sodium carboxymethylcellulose (CMC) binder deposited via aqueous slurry on a KimWipe® substrate. The graphite anode was wrapped to approximately 1.5 revolutions and held in place either through continued external pressure or alternatively using a sparing amount of water to adhere the anode to itself, thereby keeping it in place. For wetted electrodes, care was taken to ensure not too much active material is removed in the process.

Application of the separator is an important step and greatly influences the ultimate electrochemical performance. In this context, the use of a minimal separator thickness while maintaining close contact is ideal. However, ensuring no inter-electrode contact is imperative. Erring on the side of caution typically results in 1.5-2 revolutions of separator, though this is often hindered by the non-stick behaviour against the graphite anode. The contribution this makes to the internal resistance can be significant and methods to streamline and ensure a thin, tightly held separator layer would certainly be

useful.

The next layer consisted of the cathode material such as  $\text{LiCoO}_2$  constructed in similar fashion to the anode. Measured  $\text{LiCoO}_2$  loadings were  $9 \text{ mg/cm}^2$  with approximate dimensions being  $0.6 \times 0.6 \text{ cm}$  rectangles of active material yielding about  $3.5 \text{ mg}$  of active material per rotobattery. After the cathode layer followed an outer spiral of titanium wire and in some instances a final section of heat-shrinkable polyolefin tubing. A cross-sectional schematic of the final configuration is outlined below (Figure 6.2).

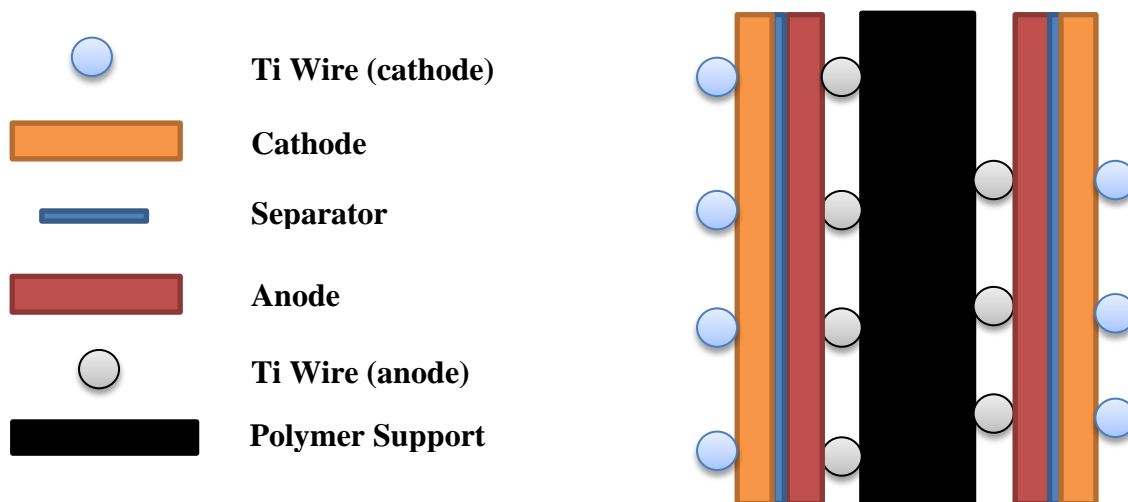


**Figure 6.2.** Longitudinal cross sectional schematic of rotobattery construction

Inclusion of the tubing applies additional external pressure to the active components, improving the cathode/separator/anode contact surface and thus the practical ionic conductivity. Temperatures applied were in excess of  $70^\circ\text{C}$  though ideally not much higher as pore closure and resulting ionic conductivity decreases would result.<sup>11</sup>

Alternatively, high temperature dimensionally stable separator materials could be utilized to mitigate the heat derived performance degradation.

Spin stability tests of this assembly minus the heat shrinkable tubing and any added electrolyte demonstrated the potential to reach 9 kHz. Given this proof of concept, attention was focused on demonstrating and improving electrochemical performance along with trial MAS-NMR experiments.

#### **6.4.1 - Initial Electrochemical Performance**

Cell testing of rotobattery prototypes has been performed under various iterations of the current design just described. Many of these attempts were too preliminary to merit mention, however the latest iteration of multi-cycle performance is depicted in Figure 6.3. The current rate corresponds to approximately  $C/70$  and the initial charge cycle appears to approach the predicted value. However, the first discharge cycle corresponds to approximately one third of the charge capacity. Subsequent charge cycles show increasingly high resistance as indicated by their higher voltage plateaus. Since these results were meant as preliminary experiments to prove cyclability in principle, liberties were taken towards cell preparation for the sake of expediency. For instance, the electrode masses were not properly balanced, allowing for excessive capacity depletion via SEI layer formation. Additionally, application of the heat gun is likely to have caused some pore closure of the separator. Future use of the methodology will involve controlled application of a specific temperature. Nevertheless, the results were encouraging enough to continue with initial NMR measurements of a charged cell.

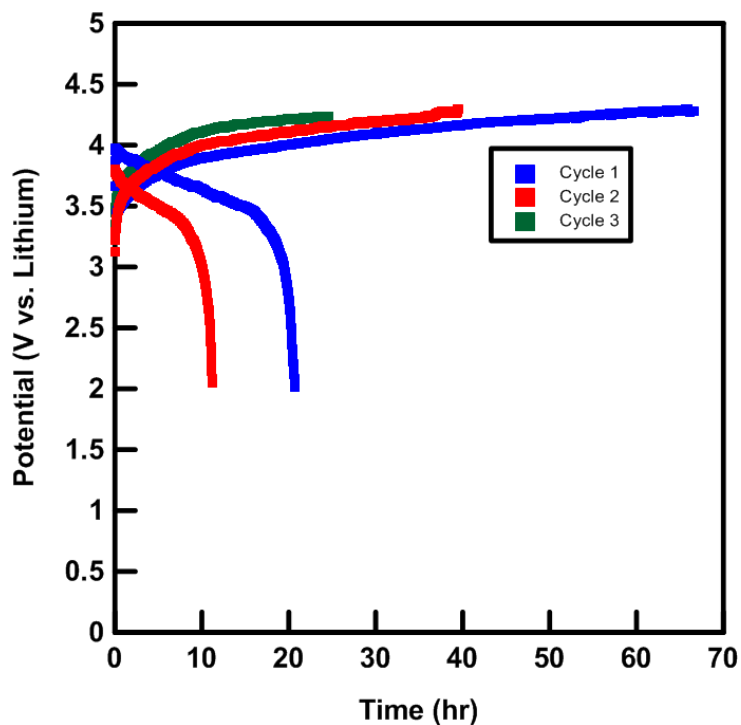


**Figure 6.3.** Initial cycling data for rotobattery prototype using an LCO cathode and graphite anode on cellulosic substrates with 1M LiPF<sub>6</sub> in EC/DMC electrolyte cycled at 7.5  $\mu$ A constant current between 2 and 4.3 V.

#### 6.4.2 - Initial NMR Performance

The primary aims for the initial NMR experiments were to demonstrate the capability to acquire <sup>7</sup>Li MAS-NMR of a fully charged LIB. In line with the previous cycling experiments, a single charge cycle to 4.6V was performed on LiCoO<sub>2</sub>/graphite full cell configuration (Figure 6.4). Importantly the entire assembly (titanium wires, anode, cathode, separator but without heat-shrink tubing) was constructed and placed inside a 4 mm rotor where it was subsequently filled with 1M LiPF<sub>6</sub> in EC/DMC. The assembly was then sealed from the glovebox environment in an Eppendorf tube and allowed to

cycle over the course of several days. Initially the remaining void space in the rotor was completely filled with electrolyte, although subsequent observation at the end of the charge cycle showed evidence of either evaporation or swelling of the plastic support with electrolyte. This may help explain the relatively poor rate performance although the assertion remains to be thoroughly tested.

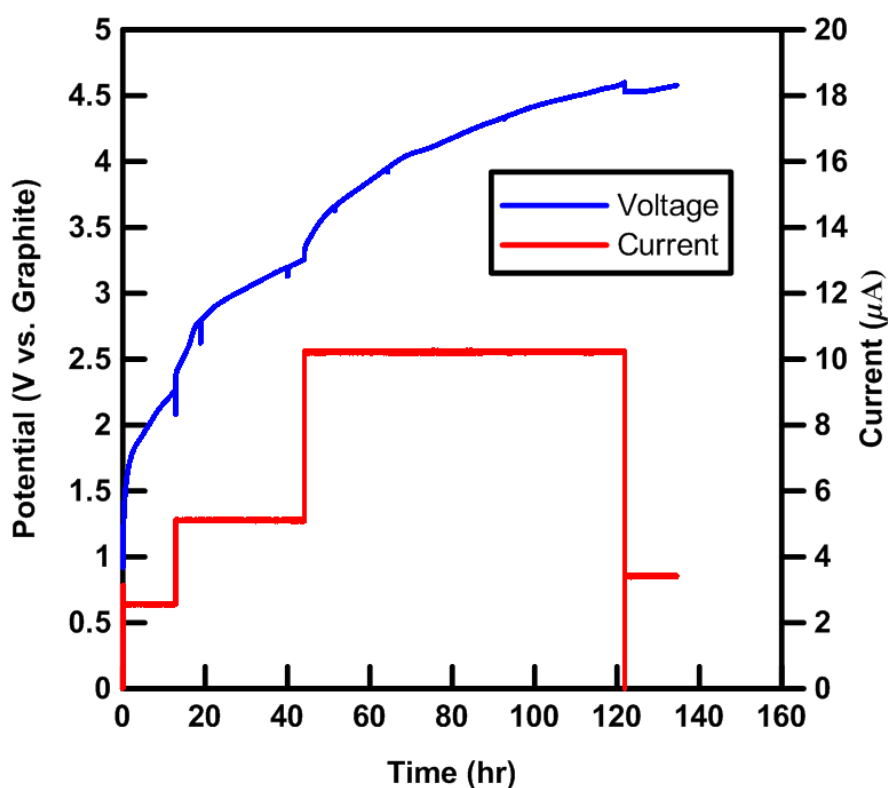


**Figure 6.4.** Single charge cycle for LCO/Graphite full cycled in 4 mm rotor with 1M  $\text{LiPF}_6$  in EC/DMC. Discontinuities constitute periodic stoppages and were often associated with an increase in current rate to expedite the experiment.

Given the importance of reaching a charged state the cycling rate was initially set to an approximate C/200, but was gradually increased up to C/50 as pauses in the experiment

demonstrated minimal voltage decline. Nevertheless the achieved capacity correlated roughly with the estimated mass of active material and successfully achieved a nominal voltage of 4.6V. At this point further charging was stopped and the rotor sealed for analysis on a 300 MHz Bruker NMR spectrometer. An initial static spectrum coupled with several MAS spectra of the charged rotobattery is depicted (Figure 6.5)

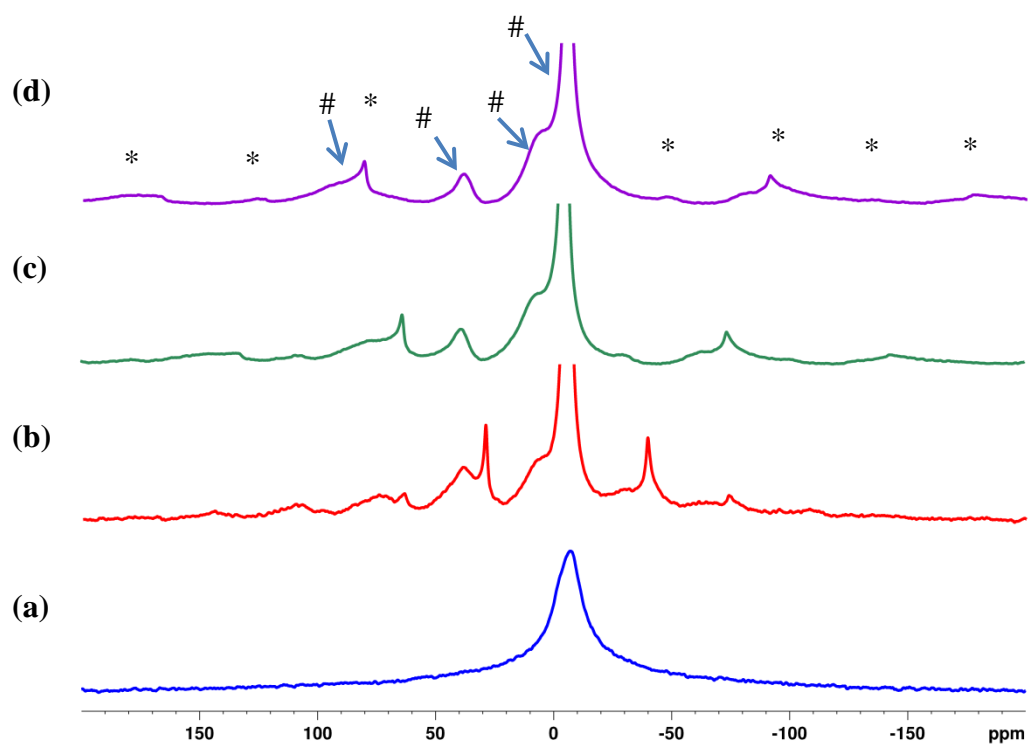


**Figure 6.5.** Stacked MAS-NMR under various conditions including static (a), 4 kHz (b), 8 kHz (c), and 10 kHz (d) of the fully charged rotobattery. The # symbols correspond to resonances while the \* symbols are their associated spinning sidebands.

The static spectrum exhibits negligible site resolution and is dominated purely by the electrolyte signal. Interestingly this resonance is relatively broad for the static spectrum of a lithium electrolyte solution. Some possible explanations include presence of solid  $\text{LiPF}_6$ , electrolyte solution trapped in the pores of cellulose, and inhomogeneity resulting from the cell components (e.g. titanium wire, plastic support). However, a dramatic improvement in spectral detail was obtained upon spinning to 4 kHz and then upwards to 10 kHz. Spectral features include resonances associated with the electrolyte ( $\approx 0$  ppm), lithiated graphite ( $\text{LiC}_{36}$ - $\text{LiC}_{18}$  @  $\approx 6.8$  ppm,  $\text{LiC}_{12}$ - $\text{LiC}_6$  @  $\approx 40$  ppm),<sup>13</sup> and their associated spinning sidebands. While this result satisfied the previously laid out objectives, the resonance associated with  $\text{LiCoO}_2$  was hard to discern in the expected 50-100 ppm range. As the spinning sidebands associated with the graphite and/or  $\text{LiPF}_6$  tended to obscure and overwhelm the region of interest, a pulse sequence to attenuate the spinning sideband intensity was utilized (Magic Angle Turning Phase Adjusted Sideband Separation or MATPASS).<sup>14</sup> A single dimensional projection of the 2D MATPASS spectra (inset) was obtained at 10 kHz spinning speed 24 hours apart (Figure 6.6). MATPASS was successful in attenuating a significant fraction of the sideband intensity but more importantly it demonstrates a change in the spectra taken 24 hours apart. Specifically they are indicative of a significant degree of self-discharge, depleting signal intensity at the graphite sites in favour of the  $\text{LiCoO}_2$  resonance ( $\approx 90$  ppm). Inadvertent observation of this self-discharge behaviour bodes well for spectral observation of future controlled discharge experiments. Although the source of the self-discharge will need to be identified as its presence is detrimental to cell performance.

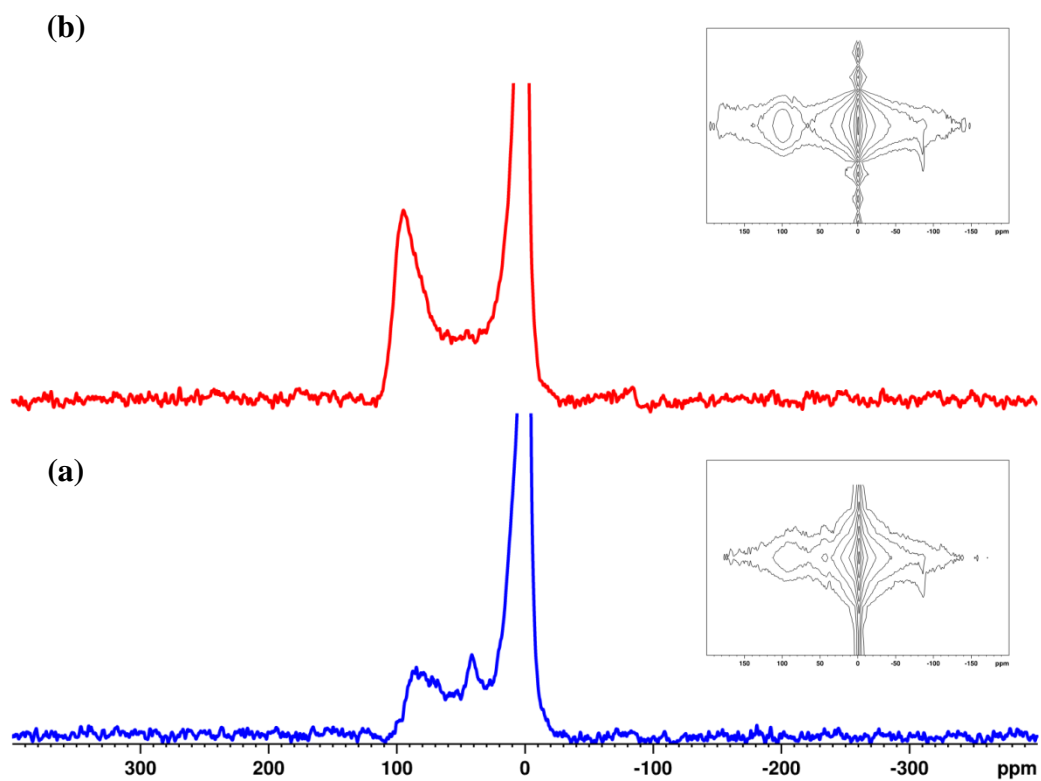


**Figure 6.6.**  $^7\text{Li}$  MATPASS spectra @ 10 kHz spinning speed for a LCO/Graphite charged rotobattery soon after ending charge (a), and 24 hours later (b).

One drawback of the MATPASS experiments includes the relatively long experiment times. The 1D projection shown in Figure 6.5 required approximately 2 hours to collect. However, a closer look at the single RF pulse spectra appears to show similar behaviour, albeit hidden somewhat by the overlapping spinning sidebands (Figure 6.7).

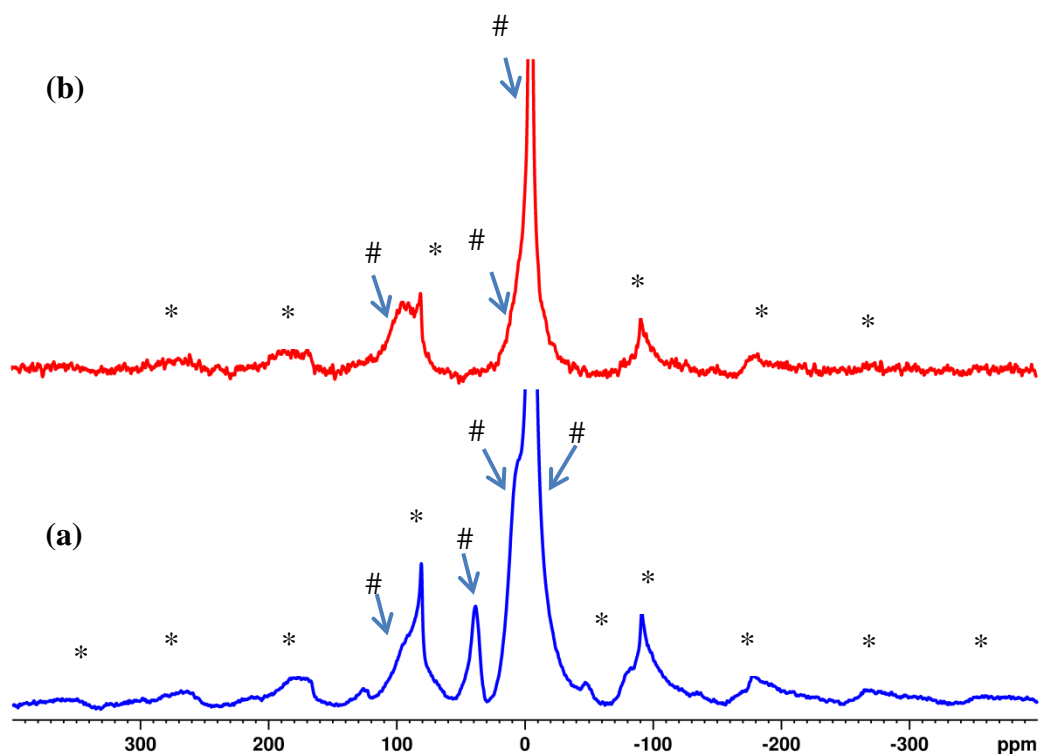


**Figure 6.7.**  $^7\text{Li}$  MAS-NMR single pulse experiments collected soon after charge (a), and after a further 24 hours (b). The # symbols correspond to resonances while the \* symbols are their associated spinning sidebands.

Focusing attention in the 0-100 ppm range seems to demonstrate clear evidence for the depletion of the lithiated graphite in favour of the  $\text{LiCoO}_2$  helping to confirm the observations in Figure 6.6. Also, spectrum 6.6 (b) was collected in a very short timeframe (<30 seconds) in comparison to the 10 minutes for 6.6(a). Despite this there is site resolution even with the short experimental time involved. Future experiments could reduce the influence of sideband overlap by using a less concentrated electrolyte and/or limiting the volume of electrolyte added to the active materials. This would further enable

rapid data acquisition and yield as close to real-time and resolved in-situ spectra as possible.

## 6.5 - Future Considerations

Progress on the rotobattery has not reached the point at which controlled discharge and subsequently photovoltaic charging are being applied. However, with the significant progress on electrochemical performance and spin stability it is foreseeable that continued work on the project would reach these stages shortly. Assuming a fully functional and spin stable experiment the wireless discharge can be facilitated through the appropriate choice of resistor.

Most commercial resistors would be incompatible due to the incorporation of metallic components. Although given that the current values required ( $\approx 3$  to  $30 \mu\text{A}$ ) a relatively large resistive component would be needed (e.g.  $1 \times 10^5$  to  $1 \times 10^6 \Omega$ ) to yield such discharge currents. One potential solution would be to use conductive or semi-conductive tape to complete the circuit. Alternatively, polymer doped with carbon black could provide the necessary electrical resistance. Either solution would have to be sufficiently resistive and capable of maintaining contact despite the rapid rotation.

Mechanisms for wireless charging present the greatest challenge to full in-situ operation. Successfully developing a method to charge the cell during in-situ MAS would enable NMR measurements during the first charge/discharge cycle and further cycles thereafter. One aspect of this to consider are the voltage requirements. In the best case scenario for a battery chemistry involving lithium titanium oxide (LTO) and lithium iron

phosphate (LFP) the corresponding voltage requirements are a minimum of 2V.

Light emitting diodes (LEDs) represent a relatively cheap and easily acquired photovoltaic element to enable wireless charging. Importantly, single LEDs are commonly manufactured to approximately  $1 \text{ mm}^2$  and could easily fit on the structural support, making them ideal for the present application. Use of a single LED would require a corresponding bandgap of at least 2 eV. A violet laser pointer outputs light at approximately 400 nm or 3.1 eV. Given minimal additional sources of resistance, an LED which emits 400 nm light would be sufficient. However, the forward voltage of a LED derives from a combination of the inherent bandgap and associated internal resistances. Thus it is likely more suitable to use a blue LED in combination with a violet laser pointer such that the forward voltage of the LED is no greater than 3.1 V. Assuming a 450 nm LED bandgap this would correspond to maximum voltage of 2.75V likely sufficient to charge a 2V LFP/LTO battery. Of course if multiple LEDs can be fashioned in series on the small space available, the voltage limitations are easily circumvented. A schematic of the cell and anticipated operation is presented in Figure 6.8. The simplest mechanism for discharge would be through the LED itself. While the resistance of an LED is high when the applied voltage does not approach the bandgap, it might be low enough to enable passage of sufficient current. An obvious drawback of this simple design is the uncontrolled discharge rate. Alternatively, a discrete resistor could be fashioned in parallel to the LED and allow controlled discharge as dictated by its electrical resistance. Practical considerations include appropriate mounting of the LED to the structural support, secure connection of the wires to the circuit, modification of the

top rotor cap to allow laser light illumination, adequate setup of the laser light source, and several more. While these design challenges are not insurmountable it would require significant troubleshooting.

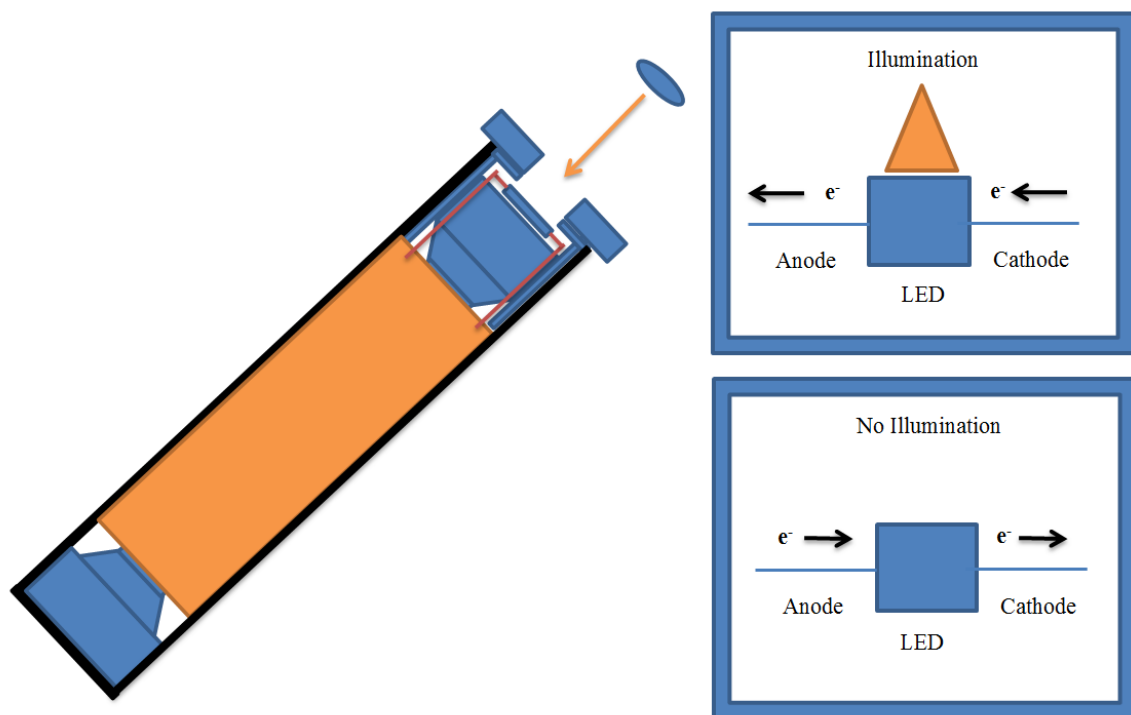


**Figure 6.8.** Schematic of rotobattery operation with left side showing support template with battery components connected to the top of the cell via a LED. The whole assembly is depicted assembled into a 4 mm rotor with the inclusion of a central hole cut in the rotor cap to allow laser light illumination. Shown right are the expected operational modes for the LED both with and without illumination.

## 6.6 – Summary

Proof of concept for certain aspects of the in-situ MAS of a functional lithium ion battery has been achieved. This includes the design and printing of a structural support along with establishing the cyclability and chemical compatibility of the battery components. An immediate next step includes in-situ controlled discharge from a charged state and associated NMR measurements. Following this, design of an appropriate charging mechanism would be the final component in rotobattery development.

## 6.7 - References

- (1) Ménétrier, M.; Saadoune, I.; Levasseur, S.; Delmas, C. The Insulator-Metal Transition upon Lithium Deintercalation from LiCoO<sub>2</sub>: Electronic Properties and <sup>7</sup>Li NMR Study. *J. Mater. Chem.* **1999**, *9* (5), 1135–1140.
- (2) Fukui, H.; Ohsuka, H.; Hino, T.; Kanamura, K. Influence of Polystyrene/Phenyl Substituents in Precursors on Microstructures of Si–O–C Composite Anodes for Lithium-Ion Batteries. *J. Power Sources* **2011**, *196* (1), 371–378.
- (3) Leifer, N.; Smart, M. C.; Prakash, G. K. S.; Gonzalez, L.; Sanchez, L.; Smith, K. A.; Bhalla, P.; Grey, C. P.; Greenbaum, S. G. <sup>13</sup>C Solid State NMR Suggests Unusual Breakdown Products in SEI Formation on Lithium Ion Electrodes. *J. Electrochem. Soc.* **2011**, *158* (5), A471–A480.

- (4) Chen, S.; Zhong, G.; Cao, X.; Gao, Y.; Jin, Y.; Wu, A.; Gong, Z.; Fu, R.; Zhao, Y.; Yang, Y. An Approach to Probe Solid Electrolyte Interface on Si Anode by <sup>31</sup>P MAS NMR. *ECS Electrochem. Lett.* **2013**, 2 (12), A115–A117.
- (5) Castaing, R.; Moreau, P.; Reynier, Y.; Schleich, D.; Jouanneau Si Larbi, S.; Guyomard, D.; Dupré, N. NMR Quantitative Analysis of Solid Electrolyte Interphase on Aged Li-Ion Battery Electrodes. *Electrochimica Acta* **2015**, 155, 391–395.
- (6) Aguiar, P. M.; Jacquinet, J.-F.; Sakellariou, D. Experimental and Numerical Examination of Eddy (Foucault) Currents in Rotating Micro-Coils: Generation of Heat and Its Impact on Sample Temperature. *J. Magn. Reson.* **2009**, 200 (1), 6–14.
- (7) Fitch, B. B.; Yakovleva, M.; Li, Y.; Plitz, I.; Skrzypczak, A.; Badway, F.; Amatucci, G. G.; Gao, Y. An Overview on Stabilized Lithium Metal Powder (SLMP), an Enabling Material for a New Generation of Li-Ion Batteries. *ECS Trans.* **2007**, 3 (27), 15–22.
- (8) Wierzbicki, T.; Sahraei, E. Homogenized Mechanical Properties for the Jellyroll of Cylindrical Lithium-Ion Cells. *J. Power Sources* **2013**, 241, 467–476.
- (9) OpenSCAD [Computer software]. (2016). Retrieved from <http://www.openscad.org/>
- (10) Mohamed, O. A.; Masood, S. H.; Bhowmik, J. L. Optimization of Fused Deposition Modeling Process Parameters: A Review of Current Research and Future Prospects. *Adv. Manuf.* **2015**, 3 (1), 42–53.

- (11) Chen, J.; Yan, Y.; Sun, T.; Qi, Y.; Li, X. Probing the Roles of Polymeric Separators in Lithium-Ion Battery Capacity Fade at Elevated Temperatures. *J. Electrochem. Soc.* **2014**, *161* (9), A1241–A1246.
- (12) Shi, C.; Dai, J.; Shen, X.; Peng, L.; Li, C.; Wang, X.; Zhang, P.; Zhao, J. A High-Temperature Stable Ceramic-Coated Separator Prepared with Polyimide Binder/Al<sub>2</sub>O<sub>3</sub> Particles for Lithium-Ion Batteries. *J. Membr. Sci.* **2016**, *517*, 91–99.
- (13) Letellier, M.; Chevallier, F.; Béguin, F. In Situ <sup>7</sup>Li NMR during Lithium Electrochemical Insertion into Graphite and a Carbon/Carbon Composite. *J. Phys. Chem. Solids* **2006**, *67* (5–6), 1228–1232.
- (14) Hung, I.; Edwards, T.; Sen, S.; Gan, Z. MATPASS/CPMG: A Sensitivity Enhanced Magic-Angle Spinning Sideband Separation Experiment for Disordered Solids. *J. Magn. Reson.* **2012**, *221*, 103–109.



## Chapter 7 – Summary, Conclusion, and Appendices

### 7.1 - Summary

Lithium ion batteries are a major component of the contemporary energy storage landscape. Current trends suggest a continued increase in their utilization, especially as fossil fuels are phased out. Further improvements to the technology can be derived from a detailed understanding of their operation and failure mechanisms. In this regard, NMR is presented as a versatile characterization tool capable of making significant contributions to the LIB field. The individual chapters which comprise this thesis have illustrated several examples of this utility.

Chapter 3 demonstrated the use of NMR in the analysis of deep eutectic electrolytes. Specifically, the MSA/DMMSA organic components were investigated in combination with the weakly coordinating LiTFSI salt. Diffusional analysis of anion, cation and organic component was accomplished using  $^{19}\text{F}$ ,  $^7\text{Li}$  and  $^1\text{H}$  measurements respectively. Diffusion coefficients thus obtained were used to parameterize molecular dynamics simulations to yield solution state structure and associated dynamics. For instance, it was found that lithium transport numbers were often significantly higher than a standard organic carbonate based electrolyte and partially compensated for the relatively lower diffusion coefficients. Additionally, hydrogen bonding was found to play a substantial role in MSA based compositions showing a relative increase in lithium transport number and associated diffusivity decrease even at identical organic:lithium salt ratios. MD simulations described this as result of increased MSA-TFSI interactions which slowed

TFSI more relative to  $\text{Li}^+$ . The work presented here was the first systematic NMR+MD analysis of its kind for the deep eutectics studied.

Chapter 4 was concerned with the use of NMR to evaluate the suitability of 15-crown-5 and 1-aza-15-crown-5 in sequestering manganese cations to mitigate capacity fade. For NMR active nuclei the relative binding affinity can be assessed through chemical shift evaluation in the free and bound states. As the paramagnetism of the  $\text{Mn}^{2+}$  and  $\text{Mn}^{3+}$  precluded this direct evaluation, observation of  $^7\text{Li}$  was instead utilized. Lithium cations were competitively inhibited from interacting with free crown ethers by the presence of manganese. This was observed in the lithium binding curves and allowed for the determination of relative binding affinity. Ultimately this supported a preference of  $\text{Mn}^{2+}$  over lithium for the crown ethers studied, but also suggested that only 1-aza-15-crown-5 was suitable for  $\text{Mn}^{3+}$  trapping. The data thus collected represents a novel demonstration of NMR based binding constant evaluation in a lithium ion battery context.

Chapter 5 described the characterization of cycled silicon monoxide anode materials through  $^{29}\text{Si}$  MAS-NMR and in-situ  $^7\text{Li}$  NMR. The key feature of these experiments was the use of cellulosic substrates in substitution of the traditionally used copper. Long term cycling of these anodes demonstrated notable performance at relatively large current densities. Additionally, the increased active material loading enabled the  $^{29}\text{Si}$  measurements performed. Another positive feature of these anodes was the enhanced RF penetration depth which made the material more suitable for in-situ NMR. This enabled key insights including in-situ  $^7\text{Li}$  NMR showing a lack of crystalline lithium silicide towards the end of lithiation. To contrast,  $^7\text{Li}$  in-situ measurements of silicon metal

anodes showed a clearly evident amorphous-crystalline transition. This feature might contribute to its enhanced native cyclability of SiO versus silicon metal. Novel contributions of this work include the first detailed  $^{29}\text{Si}$  MAS-NMR studies for silicon monoxide on a cellulosic substrate along with the construction and operation of a hitherto unexplored in-situ NMR cell design.

Chapter 6 detailed the development effort surrounding in-situ MAS-NMR. Enabling this type of experiment would substantially expand the range of in-situ NMR experiments possible, making previously unresolved resonances clearly discernable. Unfortunately there are list of complications which conspire to make its implementation a complicated endeavour. These range from spin stability and eddy current effects to electrochemical cyclability and structural considerations. While there remain substantial operational issues in the rotobattery project, there are clear signs of progress.

Firstly a range of components including cellulosic substrates and titanium wire have been successfully tested as alternatives copper as aluminum. Their relatively lower electrical conductivity mitigates eddy currents, thus enabling MAS. Additionally, rotobattery designs incorporating their use have allowed for stable spinning of a 4 mm rotor at up to 10 kHz. Electrochemical testing of these materials for cyclability has been met with moderate success. There is clear evidence for reversible capacity in full cells comprised of lithium cobalt oxide and graphite. And while resistance losses remain a concern, experiments in heat-shrinkable polyolefin tubing are being tested to decrease resistance by improving electrode-separator contact. Ultimately a prototype LCO/Graphite configuration was successfully charged and characterized via  $^7\text{Li}$  NMR.

While the photovoltaic element or a controlled discharge mechanism were not incorporated, the results were sufficient to prove the general feasibility of the design. Further development has the potential to enable full charge/discharge cycles during in-situ MAS-NMR characterization of LIBs and other relevant electrochemical devices.

## 7.2 - Future Directions

In considering further avenues for research it is instructive to consider deep eutectic electrolytes, crown ether trapping mechanisms, and in-situ NMR methodologies separately. For the DEEs, a significant drawback of the sulfonamide based formulations was the relatively low overall diffusivity in comparison to traditional organic carbonate electrolytes. One factor contributing to this feature is the bulkiness of the  $\text{CF}_3$  groups inherent to LiTFSI. An alternative can be found in the closely related lithium bis(fluorosulfonyl)imide salt which replaces the  $\text{CF}_3$  with a single fluorine. Preliminary experiments with LiFSI were performed with a dimethylsulfone organic component showing significant conductivity increases above that seen in the sulfonamides. The addition of ethyl-methyl sulfone to the LiFSI-dimethylsulfone eutectic was seen to further improve conductivity. Another area related to the investigation of deep eutectics includes the use of super-concentrated electrolyte solutions. For instance, highly concentrated LiTFSI in acetonitrile has been shown to substantially increase the reductive stability window of acetonitrile while retaining significant ionic conductivity.<sup>1</sup>

Research efforts beyond what has been described in this thesis have hinted towards interesting features of the lithium/manganese trapping mechanic in crown ethers. Where

the thesis describes an equilibrium residing predominantly in the fast exchange regime, use of electrolytes more typical of lithium ion batteries such as EC/DMC/EMC ternary electrolytes have exhibited decidedly different behaviour. Specifically, lithium trapping transitions to a slow exchange regime in these ternary electrolytes at low temperatures. This feature was not observed with propylene carbonate and suggested the possibility for both single and double crown coordination. It highlights the substantial effect of solvent composition on binding modes, even within the carbonate class of electrolytes. Continued investigation of this phenomenon would lend itself towards a self-contained investigation of lithium-crown ether binding motifs as they pertain to LIB electrolytes.

The primary drawback of the static and MAS based in-situ NMR characterization were the cycling performance features. Specifically, these proof of concept experiment were only capable of demonstrate low rate cycling with significant irreversible capacity issues. To achieve the ultimate goal of making such experiments more readily usable, improvements in cyclability are desirable.

Both static and dynamic in-situ experiments are hampered by an inability to reproduce conditions experienced in a cylindrical coin cell. Namely the degree of electrode-separator contact is relatively poor in such hand-made configurations. An iteration of the commonly used “roll-to-roll” processing scheme may be useful in addressing such issues. Specifically, a manufacturing method by which the entire battery is rolled at once under tension maintains good electrode-separator contact and improves reproducibility. Additionally, the design would maximize active material volume, further improving S/N. The main problem is that of scale, especially for rotobattery applications. A mechanism

to perform such manufacture would have to itself be developed to fit this specific application.

Besides construction, usability can be extended if a lithium rich anode can be used. While this is not an issue for the static configuration, a non-metallic lithium rich anode is essential for the rotobattery such that spinning capabilities are maintained. Ideas surrounding this include stabilized lithium metal particles, pre-lithiated silicon anodes, or electroplated lithium metal.

### **7.3 - Conclusion**

The results discussed here represent a small sampling of the NMR methodologies applicable to studying LIBs. There are a significant number of highly informative publications which detail the many other ways where NMR can be used in this context. Nevertheless, the completed research has made novel contributions to several aspects of LIB development including alternative electrolytes, manganese chelating agents, and silicon based anode materials. Additionally, progress being made in the realm of in-situ MAS-NMR has the potential to provide a novel new tool in the LIB characterization arsenal.

Taken in its entirety, this research represents one contribution among many in the expanding sphere of human knowledge. Our collective progress in this endeavour will greatly influence our lives into the 21<sup>st</sup> century and beyond.

## 7.4 - Appendices

### 7.4.1 - Chapter 3

Figures 7.3.1.1 through 7.3.1.4 display the volume integrals  $G(r)$ , for the lithium nitrogen (Figs. S-1 and S-2) and lithium-oxygen interactions. They help to further detail the discussion of the coordination environments surrounding the lithium cations. From Figs. 7.3.1.1a and 7.3.1.2a one can draw a contrast between the monodentate and bidentate coordination on one hand, and direct nitrogen coordination on the other. A comparison is made for the coordination number from the second plateau (monodentate/bidentate) versus the first (direct nitrogen coordination). This proportion is roughly 10:1 for nitrogen atoms being in an indirect versus a direct bonding environment. Furthermore, it appears that direct nitrogen coordination via MSA is found for one in every 10-20 lithium cations. This confirms that oxygen coordination is the predominant mode of interaction. The volume integrals for the lithium-oxygen coordination are shown in Figures 7.3.1.3 and 7.3.1.4 and have a number of similarities. However, a key difference is in the coordination number of lithium with respect to DMMSA versus MSA. At a 1:1 solvent:salt ratio there exists coordination of approximately 1.5 oxygen atoms from the organic components in both cases. However, at 6:1 solvent:salt ratio the oxygen coordination number for DMMSA is  $\sim 4.1$ , whereas for MSA it approaches 5 oxygen atoms. This can be explained by the smaller size of MSA and the increased mixture density when compared to the DMMSA based mixtures. Figure 7.3.1.5 uses previously reported conductivity measurements<sup>28</sup> in combination with the diffusion coefficients by

NMR, to address the issue of ionicity. The ratio between the conductivity measured by impedance spectroscopy versus that measured via NMR using the Nernst-Einstein relation is in line with the expectations outlined in the paper. Specifically, while significant ion pairing can be observed, its magnitude mirrors the trends observed in transport number. The 3:1 MSA:LiTFSI composition has the greatest degree of ionicity with a lithium transport number ranging from 0.625 to 0.6 over the temperature range of the measurements. This is in contrast to DMMSA:LiTFSI mixture, where the ionicity is lowest and the transport number ranges from 0.40 to 0.35 over the investigated temperature range. These results provide further confirmation that the introduction a hydrogen bonding component can mitigate ion pairing, albeit at the expense of overall conductivity.

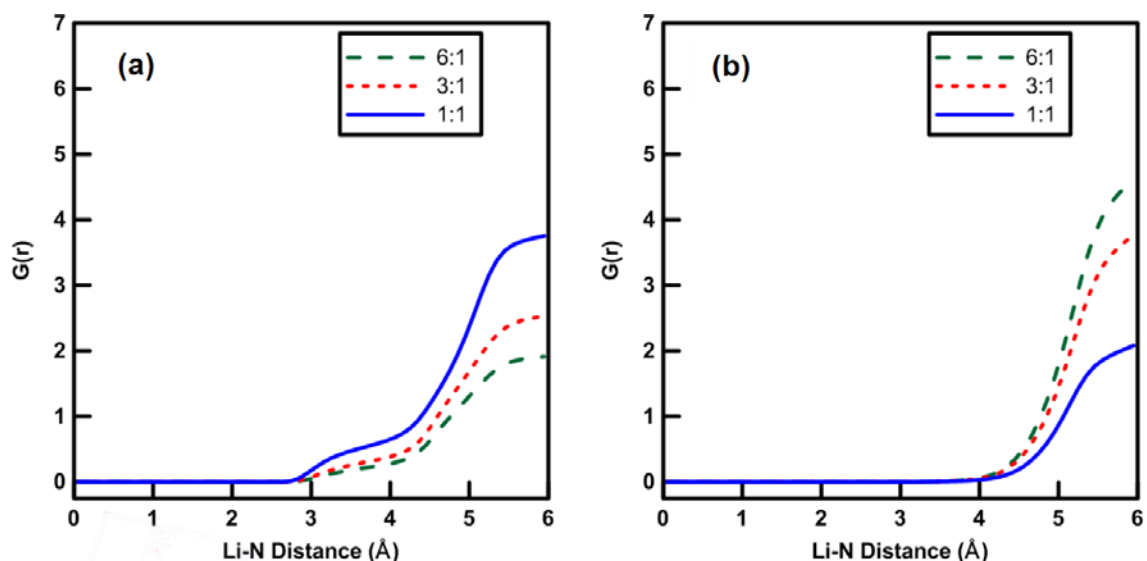


**Figure 7.3.1.1.** Lithium-nitrogen volume integrals for  $\text{Li}^+$  contact with TFSI (a) and DMMSA (b) in DMMSA:LiTFSI mixtures at 298K.

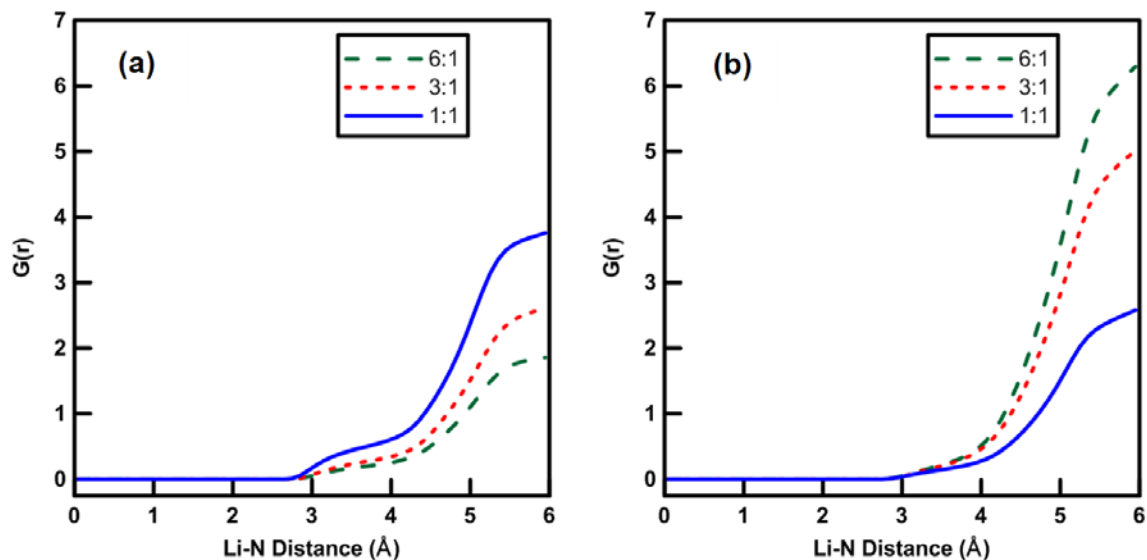


**Figure 7.3.1.2.** Lithium-nitrogen volume integrals for  $\text{Li}^+$  contact with TFSI (a) and MSA (b) in MSA:LiTFSI mixtures at 298K.

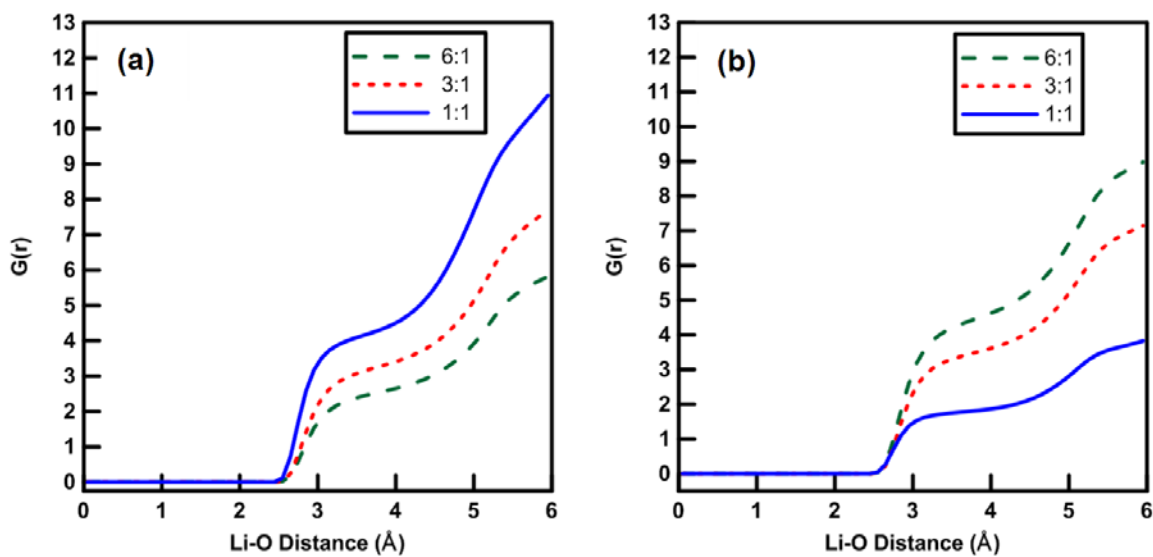


**Figure 7.3.1.3.** Lithium-oxygen volume integrals for intermolecular contact between  $\text{Li}^+$  and TFSI (a) and DMMSA (b) in DMMSA:LiTFSI mixtures at 298K.

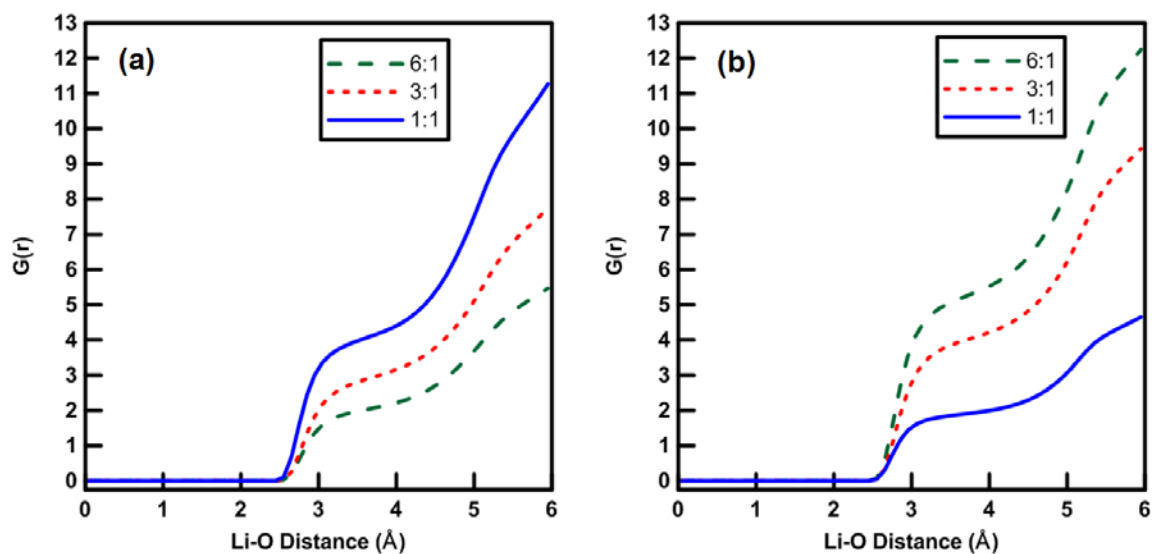


**Figure 7.3.1.4.** Lithium-oxygen volume integrals for intermolecular contact between  $\text{Li}^+$  and TFSI (a) and MSA (b) in MSA:LiTFSI mixtures at 298K.

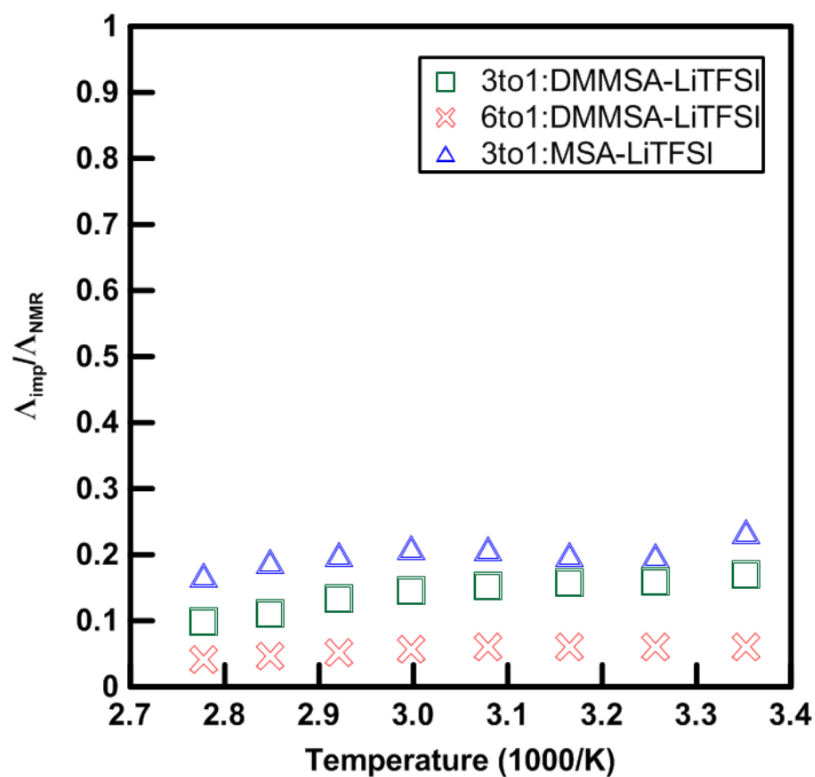


**Figure 7.3.1.5.** Ionicity derived through the ratio of molar conductivities, as determined

by impedance spectroscopy and NMR.

### 7.3.2 - Chapter 4

To be effective in a LIB, manganese trapping must operate in an environment with excess lithium. This can be modeled with equilibrium constants which take two processes into account, as shown in Eq. (1):

$$(1). \quad K_{Li} = \frac{[Li \cup \otimes]}{[Li][\otimes]} \quad K_{Mn} = \frac{[Mn \cup \otimes]}{[Mn][\otimes]}$$

The terms  $[Li \cup \otimes]$  and  $[Mn \cup \otimes]$  represent the molar concentrations of the lithium and manganese cation complexes with the crown ether, respectively. Similarly,  $[Li]$ ,  $[Mn]$ , and  $[\otimes]$  are the molar concentrations of free  $Li^+$ ,  $Mn^{x+}$ , and crown ether, respectively.

The two equilibria for lithium and manganese cation binding are related, since both consume the same source of crown ether, giving:

$$(2). \quad K_{Li} = \frac{[Li \cup \otimes]}{([Li_0] - [Li \cup \otimes])([\otimes_0] - [Li \cup \otimes] - [Mn \cup \otimes])}$$

$$K_{Mn} = \frac{[Mn \cup \otimes]}{([Mn_0] - [Mn \cup \otimes])([\otimes_0] - [Mn \cup \otimes] - [Li \cup \otimes])}$$

where the subscripted terms correspond to the initial concentrations of the respective species. From the  $K_{Mn}$  equation,  $[Mn \cup \otimes]$  can be isolated and subsequently substituted into the expression for  $K_{Li}$ . (Note that for the sake of brevity the Maple 16 command used to isolate for the variable of interest is included as opposed to the result of the operation wherever necessary.)

$$(3). \quad [Mn \cup \otimes] = isolate \left( K_{Mn} = \frac{[Mn \cup \otimes]}{([Mn_0] - [Mn \cup \otimes])([\otimes_0] - [Li \cup \otimes] - [Mn \cup \otimes])}, [Mn \cup \otimes] \right) \\ = q$$

This results in an expression where the only quantity not immediately known is  $[Li \cup \otimes]$

$$(4). \quad K_{Li} = \frac{[Li \cup \otimes]}{([Li_0] - [Li \cup \otimes])([\otimes_0] - [Li \cup \otimes] - q)}$$

NMR measurements of the average chemical shift of the lithium peak can be used to determine  $[Li \cup \otimes]$  via the associated change in chemical shift (Eq. 5):

$$(5). \quad \delta_{obs} = \delta_{Li} x_{Li} + \delta_{Li \cup \otimes} x_{Li \cup \otimes}$$

Since it is  $[Li \cup \otimes]$  that is of interest, the equation can be written such that  $[Li \cup \otimes]$  is defined in terms of the initial lithium concentration, the observed chemical shift, and the chemical shifts of the completely free and bound lithium.

$$(6). \quad [Li \cup \otimes] = -\frac{(\delta_{obs} - \delta_{Li}) \cdot [Li_0]}{(\delta_{Li} - \delta_{Li \cup \otimes})}$$

Substituting this expression into equation (4) yields the following expression:

$$(7). \quad K_{Li} = \frac{\left( -\frac{(\delta_{obs} - \delta_{Li}) \cdot [Li_0]}{(\delta_{Li} - \delta_{Li \cup \otimes})} \right)}{\left( [Li_0] - \left( -\frac{(\delta_{obs} - \delta_{Li}) \cdot [Li_0]}{(\delta_{Li} - \delta_{Li \cup \otimes})} \right) \right) \left( [\otimes_0] - \left( -\frac{(\delta_{obs} - \delta_{Li}) \cdot [Li_0]}{(\delta_{Li} - \delta_{Li \cup \otimes})} \right) - q \right)}$$

Rearranging equation (7) to solve for the  $\delta_{obs}$  would be typical although the expression this requires is significantly longer than that obtained through rearrangement for  $[\otimes_0]$ . Therefore the following operation was used to obtain an equation of the form used in the data fitting described in this manuscript

$$(8). \quad [\otimes_0] = isolate \left( K_{Li} = \frac{\left( -\frac{(\delta_{obs} - \delta_{Li}) \cdot [Li_0]}{(\delta_{Li} - \delta_{Li \cup \otimes})} \right)}{\left( [Li_0] - \left( -\frac{(\delta_{obs} - \delta_{Li}) \cdot [Li_0]}{(\delta_{Li} - \delta_{Li \cup \otimes})} \right) \right) \left( [\otimes_0] - \left( -\frac{(\delta_{obs} - \delta_{Li}) \cdot [Li_0]}{(\delta_{Li} - \delta_{Li \cup \otimes})} \right) - q \right)}, [\otimes_0] \right)$$

The type of plot this produces is with the initial crown ether concentration plotted as the dependent variable and the observed chemical shift as the independent variable (Figure 7.3.2.1) This is contrary to how the experiment is actually performed where successive increments of crown ether are added to a solution with constant metal ion concentration and the resultant chemical shift change is measured. While this does not influence the validity of the results, it represents the data in a way contrary to how it is typically shown. To achieve more logical consistency the initial plots were reoriented to reflect the mechanics of the experimental procedure as opposed to how the expression was derived.

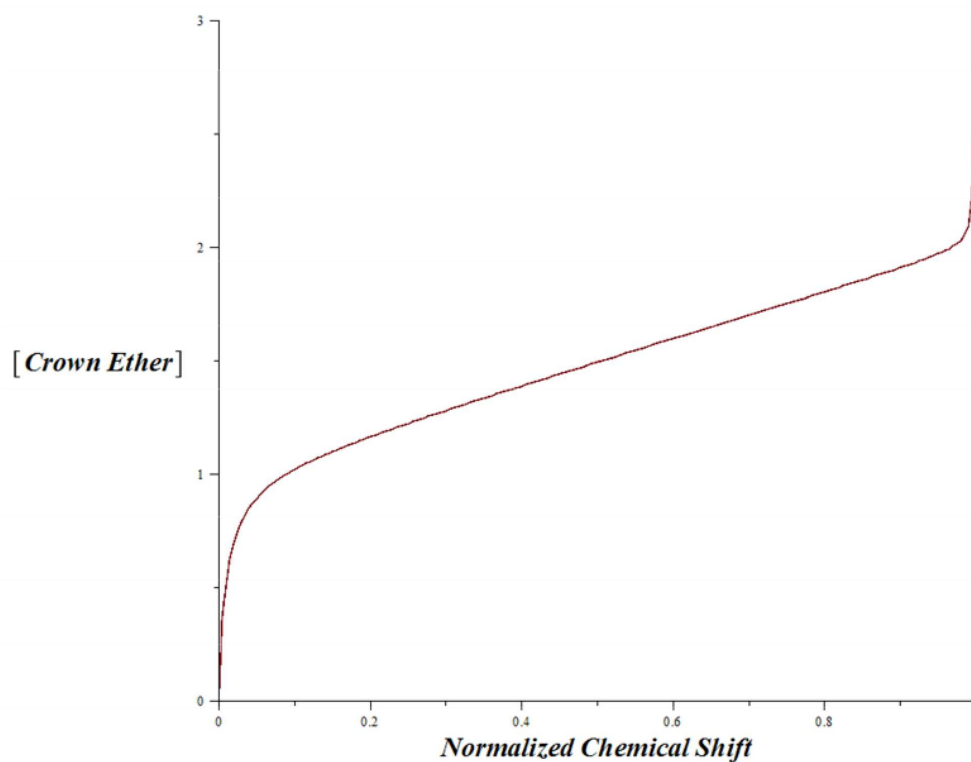


**Figure 7.3.2.1.** Example theoretical lithium binding curve generated in Maple 16 from equation (8) with [crown ether] in mM being plotted as the dependent variable and normalized chemical shift as the independent variable.

7.3.3 - Chapter 5

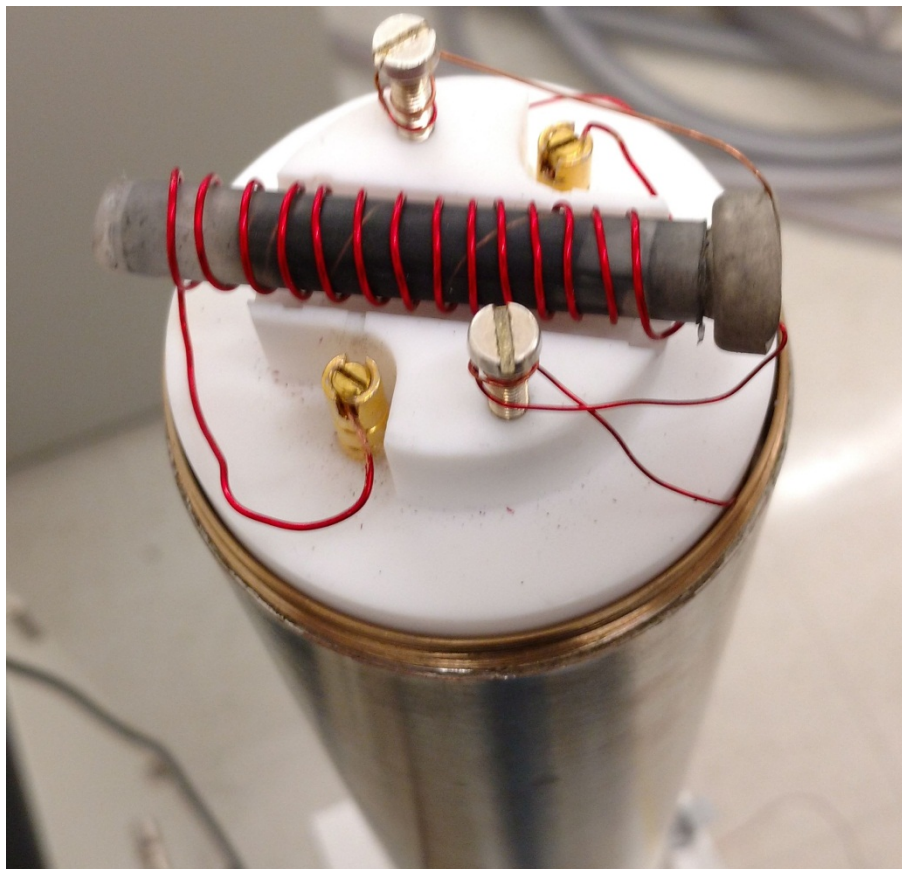


**Figure 7.3.3.1.** Top view of in-situ sample mounting configuration on probe head including anode and cathode electrical connections, strain relieving metallic posts, and connections to probe base.

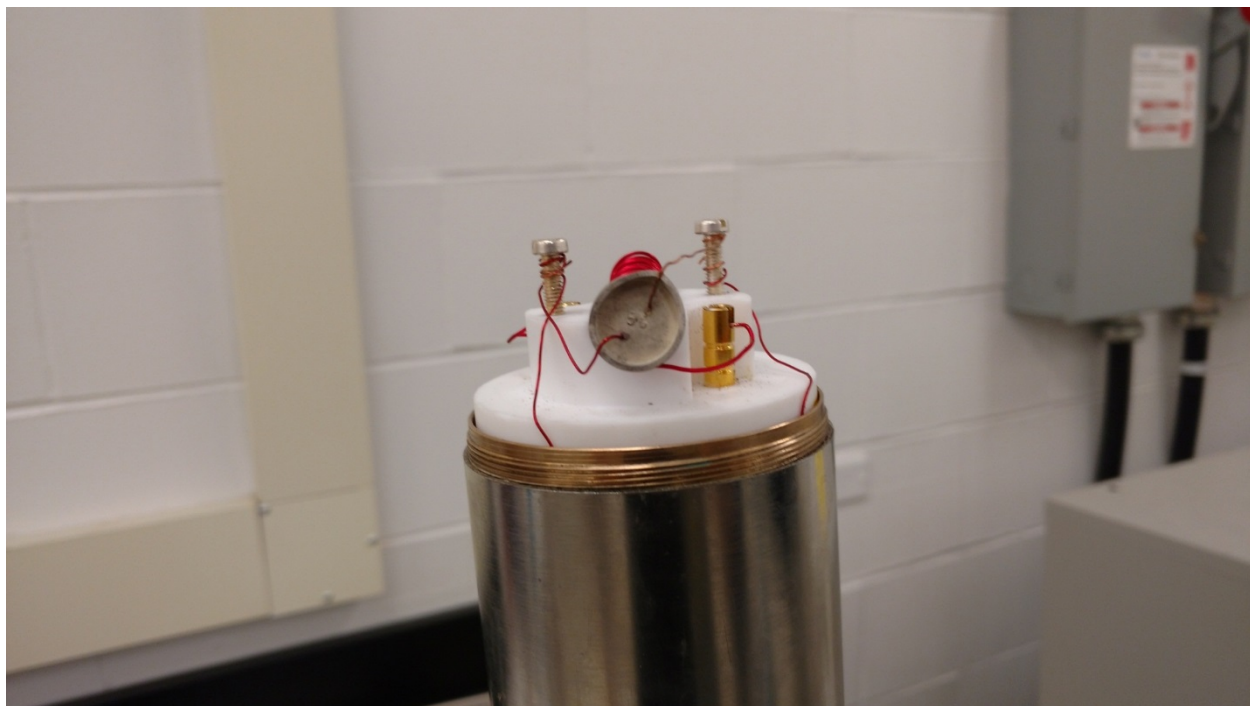
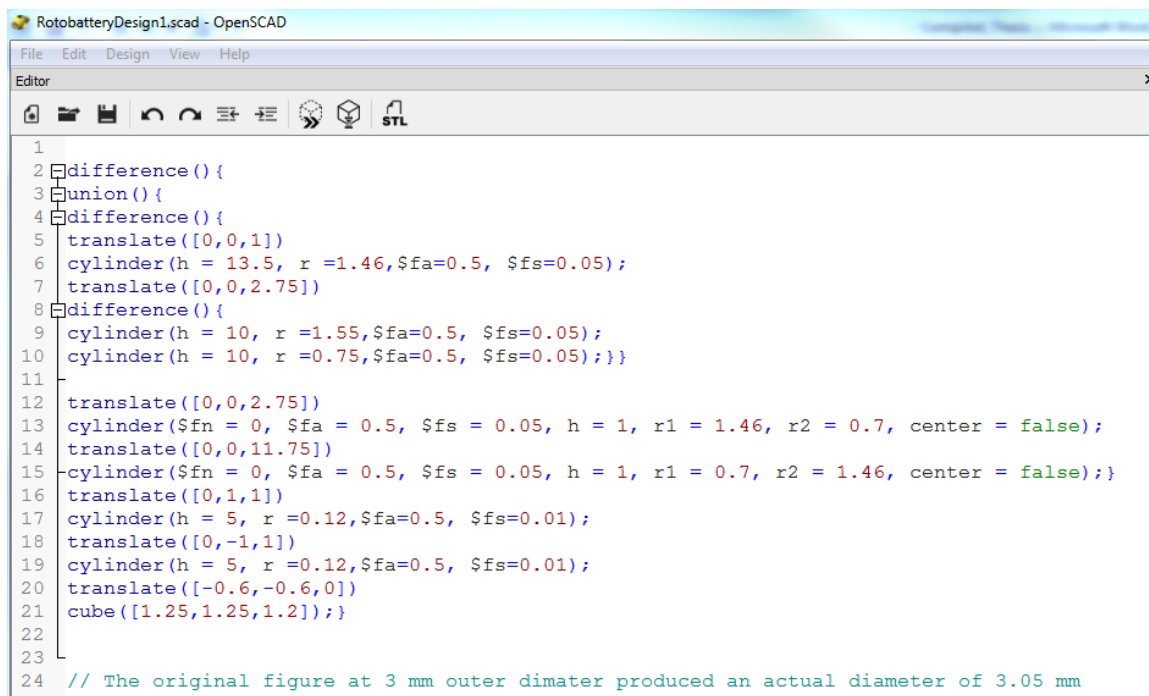


**Figure 7.3.3.2.** Side view of in-situ sample mounting configuration on probe head including anode and cathode electrical connections, strain relieving metallic posts, and connections to probe base.

### 7.3.4 - Chapter 6



```

1
2 difference(){
3 union(){
4 difference(){
5 translate([0,0,1])
6 cylinder(h = 13.5, r =1.46,$fa=0.5, $fs=0.05);
7 translate([0,0,2.75])
8 difference(){
9 cylinder(h = 10, r =1.55,$fa=0.5, $fs=0.05);
10 cylinder(h = 10, r =0.75,$fa=0.5, $fs=0.05);}}
11
12 translate([0,0,2.75])
13 cylinder($fn = 0, $fa = 0.5, $fs = 0.05, h = 1, r1 = 1.46, r2 = 0.7, center = false);
14 translate([0,0,11.75])
15 cylinder($fn = 0, $fa = 0.5, $fs = 0.05, h = 1, r1 = 0.7, r2 = 1.46, center = false);}
16 translate([0,1,1])
17 cylinder(h = 5, r =0.12,$fa=0.5, $fs=0.01);
18 translate([0,-1,1])
19 cylinder(h = 5, r =0.12,$fa=0.5, $fs=0.01);
20 translate([-0.6,-0.6,0])
21 cube([1.25,1.25,1.2]);}
22
23
24 // The original figure at 3 mm outer diameter produced an actual diameter of 3.05 mm

```

**Figure 7.3.4.1** – OpenSCAD code used to construct rotobattery support

## 7.5 - References

- (1) Yamada, Y.; Furukawa, K.; Sodeyama, K.; Kikuchi, K.; Yaegashi, M.; Tateyama, Y.; Yamada, A. Unusual Stability of Acetonitrile-Based Superconcentrated Electrolytes for Fast-Charging Lithium-Ion Batteries. *J. Am. Chem. Soc.* **2014**, *136* (13), 5039–5046.